Study on Noise Characteristics and Erosion Induced by Sodium Cavitation

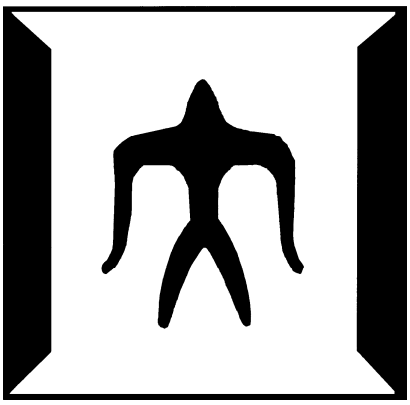

Department of Nuclear Engineering
Graduate School of Science and Engineering
Tokyo Institute of Technology

Teddy Ardiansyah

Study on Noise Characteristics and Erosion Induced by Sodium Cavitation

Dissertation submitted to
Tokyo Institute of Technology
for the degree of
Doctor of Engineering

by
Teddy Ardiansyah
09D19100

Supervised by
Associate Professor Minoru Takahashi

Department of Nuclear Engineering
Graduate School of Science and Engineering
Tokyo Institute of Technology

March 2012

Acknowledgment

Praise to Allah the most gracious and most merciful. After 4.5 years in Japan, I finally finished my doctoral study. I wish to express my gratitude to my academic advisor Prof. Minoru Takahashi who gave me opportunity to study in his lab. Special thanks are addressed to all of my reviewers Prof. Hisashi Ninokata, Prof. Masanori Aritomi, Prof. Hiroshige Kikura and Prof. Yukitaka Kato for their advice and useful comments for my dissertation.

I would like to express my highest respect and gratitude to my family in Surabaya and Lampung, my parents in Surabaya and parents in law in Lampung, my brothers and sisters for their sincere pray every day for my success in study and life. To my lovely wife Nidya Kartikasari and my soon to be born son Alif, I love you both so much and thank you very much for your support, pray, encouragement and kindness during the hard days of writing dissertation. Without your love and pray I would not stand the harsh comments from the reviewers. Last but not least, thank you to all my friends in Japan, PPI Tokodai, PPI Kanto and PPI Jepang. Thank you to Nuclear Boys in Japan during the triple disasters of March 11, 2011, Mas Kunta for his inspirational stories, Asril, Dwi, Syeilendra, Topan, Deby, Arnoldus, Mas Aziz, Mas Sidik and Pak Liem. I hope we can contribute to the development of nuclear energy in Indonesia. Thank you to my lab-mates Mas Abu, Irisawa-san, Nagasawa-san and Hino-san during the study.

This dissertation is dedicated to all the researchers in the field of thermal-hydraulics, especially those that deal with cavitation. I hope this dissertation would be useful for the advancement of science and technology in the field of nuclear engineering.

Abstract

The prevention of cavitation is one of the important problems in developing SFR (Sodium-cooled Fast Reactor) in the future. However most of the cavitation researches in the past were conducted using water to simulate sodium. This results in very limited data for sodium cavitation that could become an obstacle for the development of SFR in the future. In order to understand the characteristics of sodium cavitation for the prevention of cavitation in the future, study on the noise characteristics and erosion induced by sodium cavitation was conducted. The experiment to understand the characteristics of sodium cavitation, i.e. onset condition and noise spectrum, were conducted at flowing sodium with temperature of 200°-400°C and stagnant pressure range from 0.061-0.181 MPa-a using venturi channel. The results showed that the onset cavitation coefficient K for the judgment of cavitation occurrence in sodium had the value of around unity due to vaporous cavitation. The noise spectrum of sodium cavitation showed an increase at high frequency region from 2 kHz up to 20 kHz due to rapid collapse of cavitation bubbles (vaporous cavitation). For studying the erosion induced by sodium cavitation, the experiment was conducted in flowing sodium at 200°C for 600 hours in venturi channel. The erosion result induced by sodium cavitation showed that micro pits and micro cracks were formed on the surface of venturi channel made of stainless steel 316 even for 600 hours. These were caused by the micro jets that hit the wall of the venturi channel due to very rapid collapse of cavitation bubbles close to the wall.

Keywords: Sodium, Water, Cavitation, Onset, Noise, Erosion.

Contents

Nomenclature

Roman Letters

c	Sound speed
c_c	Empirical constant for condensation rate
c_e	Empirical constant for evaporation rate
D	Center-to-center distance
f_v	Vapor mass fraction
f_g	Gas mass fraction
h	Hard-core radius
k	Turbulent kinetic energy
K	Cavitation coefficient
p	Pressure wave emitted from pulsating sphere
ppm	Part per million
p_{sat}	Saturated pressure
p_{turb}	Turbulence pressure
P	Local static pressure
P_0	Static pressure at downstream of venturi
P_1	Static pressure at venturi
P_{stag}	Stagnant pressure
P_v	Saturated vapor pressure
P_∞	Far-field pressure in the liquid
R	Radius of the bubble

R_c Condensation rate

R_e Evaporation rate

t Time

T Liquid sodium temperature

v_v Velocity vector of the vapor phase

V_0 Liquid sodium superficial velocity in downstream of venturi

V_1 Liquid sodium superficial velocity in venturi

V_{ch} Characteristic velocity

Greek symbols

α Volume fraction of gas

β Gas fraction

γ Effective exchange coefficient; specific heat ratio

ε Turbulent dissipation rate

κ Polytrophic exponent of the gas

μ Dynamic viscosity

ρ Liquid sodium density at given temperature

ρ_m Mixture density

ρ_l Liquid density

ρ_v Vapor density

σ Surface tension

Tables

Figures

CHAPTER 1

INTRODUCTION

1.1 Background

According to the International Energy Outlook 2011 report **[1-1]**, the projection of the energy consumption grows by 53 percent from 2008 to 2035. The total world energy use rises from 505 quadrillion Btu in 2008 to 619 quadrillion Btu in 2020 and 770 quadrillion Btu in 2035. Much of the growth in energy consumption occurs in non-OECD nations due to economic growth such as in China, India, Brazil and others Asian countries. In connection with the increasing of energy demand, nuclear energy has played an important role to fulfill the energy demand and to reduce the amount of carbon dioxide produced from the burning of fossil fuels. However, one the issues in providing energy for the sustainability of the development in the world from nuclear energy is the limited amount of uranium resource that could hinder energy security. To address this problem, Generation IV nuclear energy systems forum was established to improve nuclear reactors performance in sustainability, economics and proliferation resistance **[1-2]**. One of the Generation IV nuclear reactors being researched and developed in the world widely is the Sodium-cooled Fast Reactor (SFR). SFR is a fast neutron spectrum reactor with liquid sodium coolant. The goal of this reactor is to increase the uranium usage by breeding plutonium by means of fast neutron spectrum in the core and reducing the amount of transuranic isotopes of the spent fuels leaving reactor. Other advantage of SFR is the use of liquid sodium as coolant, therefore eliminate the need to use high-pressure coolant since sodium boils at around 883°C and reduce the risk of leakage. However, in order to increase its competitiveness by reducing the cost to build it, the design of the future SFR is made compact. The compact design of SFR creates some problems from the point of fluid dynamic design. One of the problems encounter in the compact design of SFR is the

occurrence of cavitation and its erosion effect on the material. Also with the design of more compact reactor vessel and components of the future SFR, cavitation can easily occur because of higher coolant velocity in coolant flow circuits such as in the fuel assembly entrance nozzle in connecting tube, gap between support plate and fuel assembly, upper and lower neutron shields and orifices between high pressure plenum and low pressure plenum as shown in **Fig. 1.1**. Therefore, the study of cavitation and its erosion effect for SFR is very important for the safety of the future SFR. Besides erosion, cavitation can also cause material fatigue due to vibration, neutronics and hydrodynamics problems.

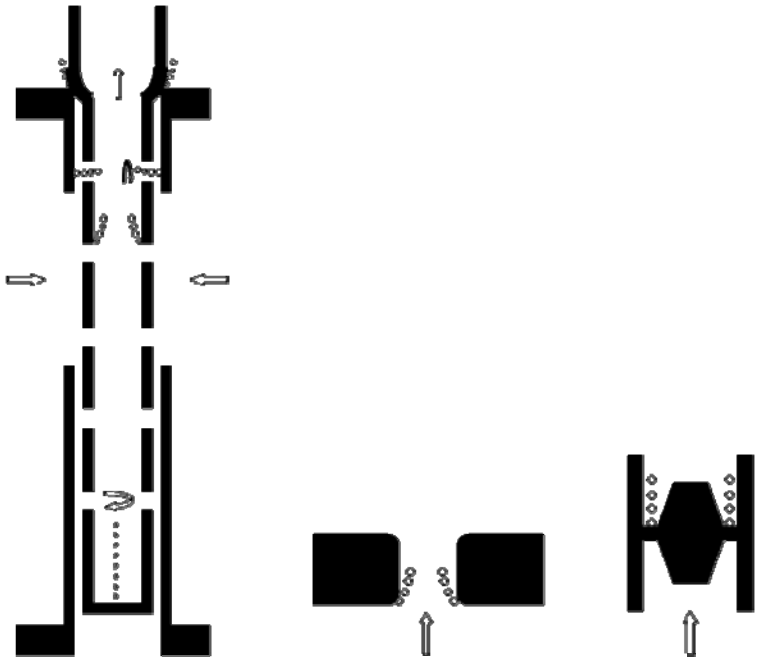

(a) (b) (c)

Fig. 1.1 Some possibilities of cavitation that can occur in **(a)** fuel assembly entrance nozzle in connecting tube and gap between support plate; **(b)** orifices between high and low pressure plenums; and **(c)** neutron shields.

1.2 Review of Previous Studies

Some researchers in the past have extensively studied cavitation, especially in uncompressible fluid such as water. Cavitation itself can be regarded as an ebullition process that takes place if the bubble grows as liquid rapidly changes into vapor and occurs when the pressure level goes below the vapor pressure of the liquid. Erosion caused by cavitation in liquid sodium is one of the critical problems for the development of future Sodium-Cooled Fast Reactor (SFR) **[1-3]**. Damage of structural material caused by the collapse of cavitation bubbles in SFR may be expected in cases where the design requires a more compact reactor vessel and components, leading to higher sodium flow velocity. The cavitation might occur in local condition where the local pressure falls below the vapor pressure of the fluid due to high flow velocity. The damage of the structural material such as cracks or severe erosion leads to the failure of the reactor component. If the damage occurs in primary coolant pipes, the leak of reactor coolant from primary circuits could take place.

Cavitation starts when the small bubbles grow into larger ones and collapse. The formation of small cavitation bubbles in flow components is an important phenomenon in cavitation stages before the bubbles can grow into violent ones and damage or erode the surface. This first stage in cavitation phenomena is known as the onset or inception of cavitation. The onset cavitation condition can be judged from the change of the audible sound noise. As the sound noise changes during the onset condition, the flow and fluid properties (static pressure, vapor pressure, density and velocity) can be grouped into one non-dimensional parameter known as cavitation coefficient or number K similar to that used in water cavitation. This cavitation coefficient or number can be used to predict the

occurrence of cavitation in the flow. Since theoretically when cavitation starts to occur (onset condition) the value of cavitation coefficient is 1 (unity). Therefore any values lower than 1 indicates the existence of cavitation in the flow. Meanwhile, many researchers have conducted the study of the cavitation by acoustic noise measurement. For instance, Sato in 1987 **[1-4]** studied the cavitation process by means of acoustic pulse measurement by using long orifice in water. He stated that cavitation process could be divided into some stages according to the measured acoustic pulse count rate with some critical points that are closely related with the flow characteristics from incipient to developed stages (change of cavitation coefficient). Sato and Kakutani **[1-5]** in his work found a relation between cavitation inception and cavitation coefficient, and the cavitation coefficient number is influenced by the air content in water. Coubiere **[1-6]** carried out a work to determine the onset cavitation condition using orifice in sodium at 250°-545°C and water at 19-62°C and found that the onset cavitation coefficient in case of orifice test section is around 2-3 and will change with the change of downstream pressure and free argon gas content. He also found that the ratio of the noise intensity increases rapidly in case of cavitation. Lin and Katz **[1-7]** in their experiment in water jet cavitation stated that the inception of cavitation are affected by the jet velocity, dissolved air content, nozzle geometry and size, boundary layer tripping and external excitation. Hammitt **[1-8** and **1-9]**, Hammitt, *et al* **[1-10** to **1-12]** and Ericson **[1-13]** conducted extensive researches on the effect of air/gas content on cavitation inception number in water and mercury. Hammitt, *et al* **[1-10]** stated that the effect of gas content (entrainment) upon cavitation initiation number for liquid metal (mercury) in a ½ inch venturi appears to be relatively small between the minimum attainable gas (around 0.2

ppm) and around 2 ppm for argon, but becomes a factor of around 2 or more for gas contents in the 3-4 ppm range. This has been demonstrated by the data to be the case for mercury temperatures ranging from room temperature to about 400°F (around 204.44°C), at a single velocity and in the steel venturi. Hammitt **[1-8** and **1-9]** and Hammitt, *et al* **[1-11** and **1-12]** also reviewed the effect of air content on the cavitation coefficient number for initiation of cavitation in water. In general, an increase in air content causes an increase in inception cavitation coefficient. Also the importance of air content upon inception cavitation coefficient depends upon the type of cavitation, i.e. bubble, laminar (steady cavity), vortex cavitation, etc., where the bubble cavitation being the most sensitive. The type of cavitation found depends on geometry and other flow parameters. Ericson **[1-13]** also found the same result with Hammitt **[1-10]** in case of mercury with injected argon gas in stainless steel venturi where the trend of increasing cavitation number can be seen if the argon gas content rises above 2%. Some works related to water cavitation in venturi and orifice as reviewed by Hammitt **[1-14]** show that the onset or inception cavitation number tends to increase with the increase of air or dissolved gas content ranging from around 0.025 to 1.2 **[1-15** to **1-19].** Duport **[1-20]** in his experiment in water show that the onset cavitation numbers did not show large differences between different orifice shapes. Hammitt and Erickson **[1-21]** also show that for venturi results with different orifice throats from 1/8 to 3/4 inch in water the air content largely influenced the onset cavitation number. Kamiyama and Yamasaki **[1-22]** show that their analytical prediction of cavitation occurrence based on analogy with the choked flow has good agreement with experimental results in organic liquids and Freon-12. They also found that the occurrence of cavitation in sodium and water has similar tendency and can

be predicted qualitatively based on critical flow analogy **[1-23]**. They tried to predict cavitation in liquid hydrogen, oxygen, nitrogen, water and Freon-113 considering the effect of vaporization, gas solubility, surface tension and electrical tension. They found that in case of water the gas solubility has significant influence to increase the incipient cavitation number **[1-24]**. Reviewed from the previous investigations of cavitation onset conditions, most of the studies were conducted using water and mercury, and very little data on sodium that has different properties with water and mercury. Also most of the studies in sodium were analytical work rather than experimental. Therefore, understanding the onset cavitation condition experimentally in sodium is very important as a threshold for the prediction of cavitation occurrence in the flow.

Previous studies in the past have shown that cavitation can produce damages. Therefore the early detection of cavitation in SFR is very important part in order to ensure the safety of the flow components. This could prevent further damages caused by cavitation such as erosion on the material surface. In regard with the occurrence of cavitation in the fluid system besides its potential to create erosion, it is generally accepted especially in the water system case that the onset of cavitation is associated with the change of its acoustic noise as one of the characteristics of cavitation since the noise is produced by the formation and collapse of cavitation bubbles. Therefore, the noise emitted from cavitation bubbles can be used as a tool to detect the occurrence of cavitation in the sodium similar to that used in water. The differentiation of cavitation noise spectrum from the background noise can be used to judge whether cavitation already occurred or not in the flow system. Bistafa in 1986 **[1-25]** measured the noise generated by cavitation in orifice plates immersed in water and found an increase of

about 20 dB between the background and cavitation noises. Frizell, *et al* in 1987 **[1-26]** found that noise frequency from a bubble generated by a nozzle in water is associated with the volume pulsation of the bubble. The sound produced is in the form of a damped sinusoidal oscillation. Research on the noise produced by bubbles splitting in a turbulent free shear flow in water showed that splitting can be a substantial noise producer with sound level above single phase jet noise **[1-27]**. The study of the cavitation noise and its correlation with the cavitation coefficient has been conducted by Zhuang, *et al* in 1988 **[1-28]** on three different headforms in water. They found that for higher cavitation coefficient the sound spectra were dominated by the background noise over low frequency. In cavitation inception, the noise levels do not increase very much in the low frequency range but increase drastically in the high frequency range. Sanjay, *et al* **[1-29]** found that the multiple peaks of noise spectrum observed in single bubbles cavitation around two axisymmetric headforms in water were resulted from several shock waves emitted during the collapse process. Arakeri, *et al* **[1-30]** in their experiment in water using axisymmetric body and seeding artificial nuclei in boundary layer stated that cavitation noise is a complex process that is not only affected by the degree of cavitation but also by the influence of the nuclei number density present in the fluid. Testud, *et al* in 2007 **[1-31]**, investigated the effect of geometry on the cavitation noise. In their experiment they stated that the acoustic noise in high degree of cavitation condition shows no differences between single-hole and multi-hole orifices. From the previous results in relation with cavitation noise reviewed above, most of the researches in cavitation noise did not explain in detail the spectrum of the noise especially in the case of sodium cavitation noise. Since in the complex flow systems, the different noise

spectrums might have the same noise intensity or magnitude. Also, most of the results were obtained in water as a model fluid that has different properties with sodium. Therefore it is important to differentiate the noise spectrum between cavitation and no cavitation conditions in sodium.

In case of cavitation damage, previous researchers have studied the damage of liquid metal cavitation by using liquid sodium and tap water in vibratory apparatus at temperatures range of 400°-1500°F (204.44°-815.56°C) in sodium and using various materials **[1-32** to **1-40]**. As results, it has been known that cavitation causes damages on the surface of the materials in the forms of coarse surfaces, pits and cracks and influenced by the magnitude of bubble collapse, amplitude of the vibration, system pressure, fluid and material properties. For the study of liquid metal erosion itself especially in liquid sodium, cavitation tests were conducted mostly by using vibratory apparatus at non flowing condition in sodium since it can be done at relatively low cost, the liquid metals inventory can be easily operated and handled, and a large number of data can be obtained for various combinations of liquid metals and test materials for relatively short duration of time. However, cavitation tests using the vibratory apparatus lack the information of the actual damage process in practical flowing condition, since most of the components that suffer from cavitation are operated in the flowing systems. The formation and collapse sites of cavitation bubbles in flowing systems are different from each other compared to vibratory apparatus where the formation and collapse sites are approximately the same. Also the growth and collapse process of the bubbles in flowing condition might be difference since the shapes of the bubbles at flowing conditions are influenced by the flow, hence influence the damage on the surface of material. Smith,

DeVan and Grindell **[1-41]** conducted the cavitation damage study to centrifugal pump impellers made from Inconel using sodium at temperatures of 1050°-1250°F (565.56°-676.67°C) for 2575 hours of sodium pump operation. They found that the damages were located mostly on the trailing side of the main vanes and approximately equidistant between the main and the splitting vanes, indicating flow influence. Robinson and Hammitt **[1-42** and **1-43]** found that pitting damages formed by cavitation in case of water system are influenced by the flow of the water and the pits have either approximately symmetrical or irregular shapes following the flow. Meanwhile, most of the materials used for the flow components of SFR are stainless steel. The cladding tube of the fuel is also made from stainless steel, i.e. 316 SS (316 Stainless Steel). However, review from the previous publications found that most of the data for cavitation damage of 316 SS in liquid sodium are obtained for short period of time and by using vibratory apparatus at non flowing condition, while for longer time at flowing condition in sodium pump using Inconel. Therefore it is necessary to know in more detail the damage on the surface of the test section caused by cavitation in flowing liquid sodium that can match closely with the real cavitation condition, i.e. in flowing condition. For that reason, cavitation erosion experiment in sodium using venturi made from 316 SS was conducted, because 316 SS is used in the fuel cladding of SFR where the possibility of cavitation could occur and erode the surface due to high velocity.

1.3 Purpose of Study

The purpose of the study presented in this dissertation is:

1) To investigate the detail of the onset or inception condition in sodium as a threshold for the prediction of cavitation occurrence in the flowing system and prevention of cavitation damages. The results are compared with the onset condition in water cavitation case. The formation of small cavitation bubbles in flow components is an important phenomenon in cavitation stages before the bubbles can grow into violent ones and damage or erode the surface. This important first stage in cavitation phenomena is known as the onset or inception of cavitation. Therefore, knowing the onset condition is very important in order to prevent cavitation to grow even further. Previous researches on sodium and water cavitation are not enough since there are no direct comparisons between sodium and water cavitation using the same test section geometry and fluid parameters (kinematic viscosity). Therefore, comparing between the two results are difficult to be done using data from previous studies.
2) To investigate the detail of the cavitation noise spectrum in sodium as a method to detect the occurrence of cavitation in the flowing system for the prevention of cavitation damages. The results are compared with the cavitation noise spectrum in water cavitation case. The differentiation of cavitation noise from the background noise is very important because it can be used to judge whether cavitation already occurred or not in the flow system. The early detection of cavitation from the noise could prevent cavitation bubbles growing into developed cavitation condition that could severely damage the material and creates undesirable problems. There are no data from the previous researches that give details of the sodium cavitation noise spectrum in flowing system. Therefore, it is very important to conduct cavitation noise experiment.

3) To investigate the detail of the erosion on the surface of the test section material made from 316 SS caused by cavitation bubbles collapse in sodium flow for long time period (600 hours). 316 SS is chosen because this material is used as cladding material in SFR. The experiment was conducted to understand the erosion due to cavitation in practical sodium flow system since there is very limited data concerning sodium cavitation damage in flowing condition.

1.4 Outline of Dissertation

The outline of this dissertation consists of:

Chapter 1 Introduction

This chapter describes the background of the study, review of the previous research and the purpose of the study. First the development of SFR and the issue related to cavitation is explained briefly. Next, previous research related to cavitation is presented in detail. Finally the purpose of the study is explained.

Chapter 2 Experimental Apparatus and Procedure for Sodium and Water Cavitation

This chapter describes the experimental apparatuses and procedure for the study in sodium and water cavitation. The detail of the apparatus, test sections and the sensors used for the measurements are explained in detail as well as the experimental procedure.

Chapter 3 Characteristics of Onset Condition in Sodium and Water Cavitation

This chapter explains the characteristics of the onset condition for sodium and water cavitation conducted with the same venturi channel geometry for comparison. These experiments were conducted to understand the onset or the beginning condition of the cavitation occurrence in sodium and water that is very important for the prediction of cavitation. Since cavitation can be prevented earlier if the onset condition can be predicted in the flow. The experiments were conducted in sodium at 200-400°C and in water at 56-90°C because of the same kinematic viscosity between sodium and water at these temperatures. The results were presented in the form of noise intensity change and the change of the non-dimensional parameter known as cavitation coefficient K that relates the change of the static pressure with the change of the dynamic pressure derived from Bernoulli's equation.

Chapter 4 Characteristics of Noise Spectrum in Sodium and Water Cavitation

This chapter describes the results of the experiments to understand the characteristics of the noise spectrum in sodium cavitation that is very important for the early detection of cavitation. The results are compared with water cavitation case conducted for the same test section geometry using venturi channel. The experiments were conducted in sodium at 200-400°C and in water at 56-90°C because of the same kinematic viscosity between sodium and water at these temperatures. The spectrum results were measured and analyzed in detail for each cavitation condition in both sodium and water, i.e. no cavitation, intermittent cavitation and developed cavitation.

Chapter 5 Erosion in Sodium Cavitation

This chapter explains the result of erosion on the surface of stainless steel 316 in flowing sodium cavitation using venturi for 600 hours at 200°C in developed cavitation condition with cavitation coefficient *K*: 0.59-0.51. The erosion results in the form of micro pits and micro cracks were observed in detail by using optical microscope and SEM on the surface of the 316 SS. The pits distribution and diameter on the surface of the 316 SS were counted and discussed in detail.

Chapter 6 Conclusions

This chapter summarizes all the conclusions from each chapter in the study.

1.5 References

1-1 International Energy Outlook 2011, (2011), DOE/EIA-0484.

1-2 Generation IV Nuclear Energy Systems, (2009), The U.S. Department of Energy's Office of Nuclear Energy.

1-3 Konomura, M. and Ichimaya, M., (2009), Design Challenges for Sodium Cooled Fast Reactors, Journal of Nuclear Materials, Vol. 371, pp. 250-569.

1-4 Sato, K., (1987), A Study of Cavitation Process by Means of Acoustic Pulse Measurement, International Symposium on Cavitation Research Facilities and Techniques, FED-Vol. 57, December, 13-18, pp. 115-121.

1-5 Sato, K. and Kakutani, K., (1994), Measurement of Cavitation Inception, JSME International Journal Series B, Vol. 37, No. 2, pp. 306-312.

1-6 Courbiere, P., (1984), An acoustic Method for Characterizing The Onset of Cavitation in Nozzles and Pumps, International Symposium on Cavitation Inception, pp. 137-143.

1-7 Lin, H. J. and Katz, J., (1987), The Effect of Background Noise on Cavitation Phenomena in Water Jets, Cavitation and Multiphase Flow Forum, FED-Vol. 50, June 14-17, pp. 41-44.

1-8 Hammitt, F. G., (1971), Effects of Gas Content Upon Cavitation Inception, Performance, and Damage, UMICH 01357-19-T.

1-9 Hammitt, F. G., (1971), Effects of Gas Content Upon Cavitation Inception, Performance, and Damage (Summary Report for Working Group No. 1 of Section for Hydraulic Machinery, Equipment and Cavitation of IAHR), UMICH 01357-21-T.

1-10 Hammitt, F. G., Robinson, M. J., Kersppainen, D. J. and Robinson, R. A., (1965), Gas Entrainment Effects on Cavitation Number in Mercury in ½ inch Venturi to 400°F, Internal report 06110-7-I.

1-11 Hammitt, F. G., Robinson, M. J., Koopman, R. P. and Ericson, D. M., (1966), Gas Content Effects on Cavitation Number in Water in A Cavitating Venturi, TR-19.

1-12 Hammitt and Ericson, D. M., (1969), Scale Effects Including Gas Content Upon Cavitation in A Flowing System, TR-01357-11-T.

1-13 Ericson, D. M., (1969), Observations and Analyses of Cavitating Flow in Venturi Systems, Ph.D dissertation, University of Michigan.

1-14 Hammitt, F. G., (1971), Effects of Gas Content Upon Cavitation Inception, Performance, and Damage, UMICH 01357-19-T.

1-15 Numachi, F. and Kurokawa, T., (1938), Ueber die Kavitationsentstehung mit besonderem Bezug auf den Luftgehalt des Wassers, Tech. Rep. of Tohoku Imperial Univ., Vol. XII, No. 4.

1-16 Numachi, F. and Kurokawa, T., (1938), Ueber den Ein fluss des Luftgehalts auf die Kavitationsentstehung im Salzwasser, Tech. Rep. of Tohoku Imperial Univ., Vol. XII, No. 4.

1-17 Numachi, F. and Kurokawa, T., (1938), Ueber den Ein fluss des Luftgehalts auf die Kavitationsentstehung im Meerwasser, Tech. Rep. of Tohoku Imperial Univ., Vol. XII, No. 4.

1-18 Numachi, F. and Kurokawa, T., (1939), Ueber den Ein fluss des Luftgehalts auf die Kavitationsentstehung, Werft Reederei Hafen, Vol. XX.

1-19 Williams, E. E. and Mc Nulty, P., (1956), Some Factors Affecting the Inception of Cavitation, Proceeding of 1955 NPL Symposium in Hydrodynamics, Paper 2, H. M. Stationary Office, London.

1-20 Duport, J. P., (1967), La Cavitation de Melange, Revue Francaise de Mecanique, No. 24, pp. 79-87 also available as SOGREAH Rept. NT. 1370, January (1968).

1-21 Hammitt, F. G. and Ericson Jr., (1970), D. M., Scale Effects Including Gas Content Upon Cavitation in a Flowing System, Proc. Symposium on Pumps and Compressors, Leipzig, DFR, also available as Univ. Mich. ORA Rept., 01357-11-T, AOYO, Ann Arbor Michigan.

1-22 Kamiyama, S. and Yamasaki, T., (1986), Critical Condition of Cavitation Occurrence in Various Liquids, Journal of Fluids Engineering, Vol. 108, pp. 428-432.

1-23 Kamiyama, S. and Yamasaki, T., (1980), One Predicting Method of Gaseous Cavitation Occurrence in Water and Sodium, Bulletin of the JSME, Vol. 23, No. 183, pp. 1428-1434.

1-24 Kamiyama, S. and Yamasaki, T., (1982), One Prediction Method of Cavitation Occurrence in Special Liquids (in Japanese), Bulletin of the JSME, Vol. 48, No. 125, pp. 43-49.

1-25 Bistafa, S. R., (1986), Noise Generated by Cavitation in Orifice-Plates with Some Gaseous Effects, International Symposium on Cavitation and Multiphase Flow Noise, pp. 41-52.

1-26 Frizell, K. W. and Cheng, J., (1987), Air Bubble Creation Noise, Cavitation and Multiphase Flow Forum, FED-Vol. 50, June 14-17, pp. 5-7.

1-27 Frizell, K. W., Cheng, J. and Arndt, R. E. A., (1987), Characteristics of Bubble Splitting Noise, Cavitation and Multiphase Flow Forum, FED-Vol. 50, June 14-17, pp. 38-40.

1-28 Zhuang, H. and Liu, K., (1988), An Experimental Study on Cavitation Noise on Headforms, Cavitation and Multiphase Flow Forum, FED-Vol. 64, July 24-28, pp. 68-70.

1-29 Kumar, S. and Brennen, C. E., (1991), Statistics of Noise Generated by Travelling Bubble Cavitation, Cavitation and Multiphase Flow Forum, FED-Vol. 109, June 23-27, pp. 55-61.

1-30 Arakeri, V. H. and Shanmuganathan, V., (1985), On the Evidence for the Effect of Bubble Interference on Cavitation Noise, Journal of Fluid Mechanics, Vol. 159, pp. 131-150.

1-31 Testud, P., Mussou, P., Hirschberg, A. and Auregan, Y., (2007), Noise Generated by Single-Hole and Multi-Hole Orifices in A Water Pipe, Journal of Fluid and Structures, Vol. 23, pp. 163-189.

1-32 Young, S. G. and Johnston, J. R., Effect of Temperature and Pressure on Cavitation Damage in Sodium, (1970), Characterization and Determination of Erosion Resistance, ASTM STP 474, American Society of Testing and Materials, pp. 67-108.

1-33 Preiser, H. S., Thiruvengadam, A. and Couchman III, C. E., (1964), Cavitation Damage in Liquid Sodium, NASA CR-54071.

1-34 Thiruvengadam, A., Preiser, H. S. and Rudy, S. L., (1965), Cavitation Damage in Liquid Metals, NASA CR-54391.

1-35 Thiruvengadam, A. and Preiser, H. S., (1965), Cavitation Damage in Liquid Metals, NASA CR-72035.

1-36 Young, S. G. and Johnston, J. R., (1967), Effect of Cover Gas Pressures Up To 4 Atmospheres on Accelerated Cavitation Damage in Sodium, NASA TMX-61065.

1-37 Young, S. G. and Johnston, J. R., (1968), Effect of Cover Gas Pressures on Accelerated Cavitation Damage, NASA TMX-52414.

1-38 Young, S. G. and Johnston, J. R., (1967), Accelerated Cavitation Damage of Steels and Superalloys in Sodium and Mercury, Erosion by Cavitation or Impingements, ASTM STP 408, American Society of Testing and Materials, pp. 186-219.

1-39 Kamiyama, S., Koike, K. and Kawaguchi, H., (1982), Effects of a Magnetic Field on Cavitation Damage (Experiments in Tap Water), Bulletin of the JSME, Vo. 25, No. 209, pp. 1690-1695.

1-40 Okada, T. and Iwai, Y., (1990), Cavitation Erosion, JSME International Journal, Series 1, Vol. 33, No. 2, pp. 128-135.

1-41 Smith, P. G., De Van, J. H. and Grindell, A. G., (1963), Cavitation Damage to Centrifugal Pump Impellers during Operation with Liquid Metals and Molten Salt at 1050-1400 F. Transaction of the ASME Series D, Journal of Basic Engineering, Vol. 85, pp. 329-337.

1-42 Robinson, M. J. and Hammitt, F. G., (1967), Detailed Damage Characteristics in a Cavitating Venturi, Transaction of the ASME Series D, Journal of Basic Engineering, Vol. 89, pp. 161-173.

1-43 Hammitt, F. G., (1963), Observations of Cavitation Damage in a Flowing System, Transaction of the ASME Series D, Journal of Basic Engineering, Vol. 85, pp. 347-359.

CHAPTER 2

EXPERIMENTAL APPARATUS AND PROCEDURE FOR SODIUM AND WATER CAVITATION

2.1 Introduction

Sodium cavitation is one of the important problems for the development of SFR in the future. However most of the studies were conducted in water instead of sodium. Therefore experimental study in sodium and water are necessary in order to understand the clear differences between sodium and water cavitation. In this study, two kind of different experiments were conducted. One in sodium and the other one in water. In sodium, two experiments were conducted separately to observe the characteristics of sodium cavitation (onset, acoustic noise and erosion). The sodium cavitation experiment to observe the onset condition and acoustic noise were conducted at 200°, 300° and 400°C with stagnant pressure range of 0.061-0.181 MPa-a. Cavitation erosion experiment in sodium were conducted at 200°C for 600 hours at developed cavitation condition (K: 0.59-0.51). While in water, water cavitation experiments were also conducted at two different experiments. One experiment of water cavitation were conducted at 56°, 74° and 90°C at atmospheric pressure to observe the onset and acoustic noise spectrum of water cavitation. The other experiment to observe the dynamics of water cavitation were conducted at room temperature with the stagnant pressure of 0.062 MPa-a. The detail description of experimental apparatus, test section, accuracy and experimental procedure are explained below.

2.2 Sodium Loop Apparatus

The sodium cavitation experiment was conducted by using the sodium loop apparatus. The schematic of the sodium loop facility at Sukegawa Electric Co., Ltd. is shown in **Fig. 2.1**. This sodium loop can be operated up to 500°C at 0.2 Mpa-a and 40

L/min. The sodium inventory of the loop is about 90 kg. The loop consists of the test section with venturi part, electromagnetic pump (EMP), electromagnetic flow meter (EMF), heater, cooler, cold trap and expansion tank. The test section is located about 3.6 m above the ground so that the static pressure could be lower in order to realize cavitation. The heater controls sodium temperature in the loop during experiment. Argon gas is used as a cover gas by injecting it inside the expansion tank. EMP is used to circulate liquid sodium inside the loop. Liquid sodium flow rate is measured by using EMF and the cold trap is used to purify liquid sodium from impurity. Liquid sodium is charged to the loop facility at 120°C before experiment. The impurity is estimated to be 1 ppm (part per million) at this condition and most of the impurities are oxides. The physical and thermodynamic properties of sodium used for the experiments are listed in **Table 2.1**.

Fig. 2.1 Picture of sodium loop apparatus at Sukegawa Electric, Co., Ltd.

Table 2.1 Physical and thermodynamic properties of sodium **[2-1]**.

Melting point [°C]	98.0
Boiling point [°C]	883.0
Vapor pressure at 200°-400°C [kPa]	2.2×10^{-5} - 5.2×10^{-2}
Liquid density at 200°-400°C [$kg.m^{-3}$]	903.0 - 857.7
Surface tension at 200°-400°C [$N.m^{-1}$]	1.90×10^{-1} – 1.69×10^{-1}
Viscosity at 200°-400°C [Pa.s]	4.52×10^{-4} – 2.77×10^{-4}
Calculated argon gas solubility at equilibrium from 200°-400°C [ppm]	4.46×10^{-3} – 2.83
Kinematic viscosity at 200°-400°C [$m^2.s^{-1}$]	5.01×10^{-7} – 3.23×10^{-7}
Sound velocity 200°-400°C [$m.s^{-1}$]	2462.2 – 2366.2

2.2.1 Description of the Venturi Channel

Figure 2.2 shows a schematic of the test section for the present liquid sodium cavitation experiment. The piping of the test section including the venturi is made from 316 SS (316 stainless steel) since this material is used as fuel cladding of SFR due to its good compatibility with sodium. The test section consists of the venturi channel, the wave-guide rod and the static pressure tap. Cavitation is realized in the venturi by increasing liquid sodium flow velocity gradually using a voltage slider until cavitation noise is heard. The inner diameter (ID), the outer diameter (OD) and the length of the venturi are 6.5 mm, 21 mm and 20 mm, respectively as shown in **Fig. 2.3**. Occurrence of cavitation is judged by an indirect method **[2-2]** using an accelerometer (Ono Sokki NP-

2710) mounted at the end of the wave-guide rod. The wave-guide rod is used to direct the acoustic noise signal to the accelerometer and acting as a heat resistance since the temperature of the accelerometer must be maintained not to exceed the accelerometer operating temperature range. The static pressure of the liquid sodium downstream of the test section is measured by the diaphragm connected at the pressure tap and transmitted along the silicon oil tube to the pressure transducer (Ashcroft GC-51, **Fig. 2.4**). This silicon oil tube also acts as a heat resistance to keep the maximum allowable temperature of the pressure gauge below 200°C. At the top of the test section, a gas injector made of porous tungsten plug with porosity of 30% is mounted. The temperature is measured by using thermocouple.

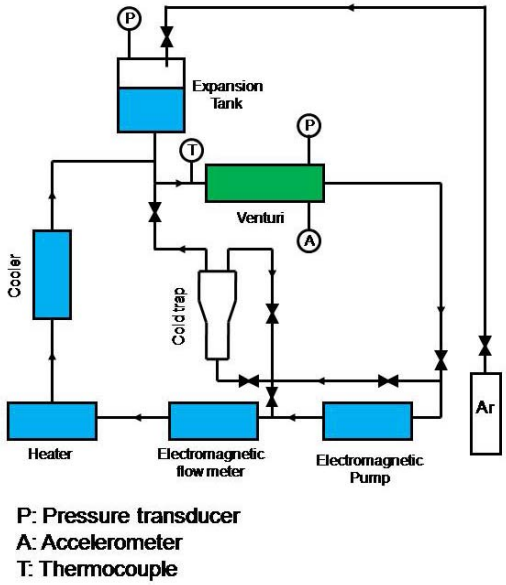

Fig. 2.2 Schematic of sodium loop apparatus at Sukegawa Electric Co. Ltd.

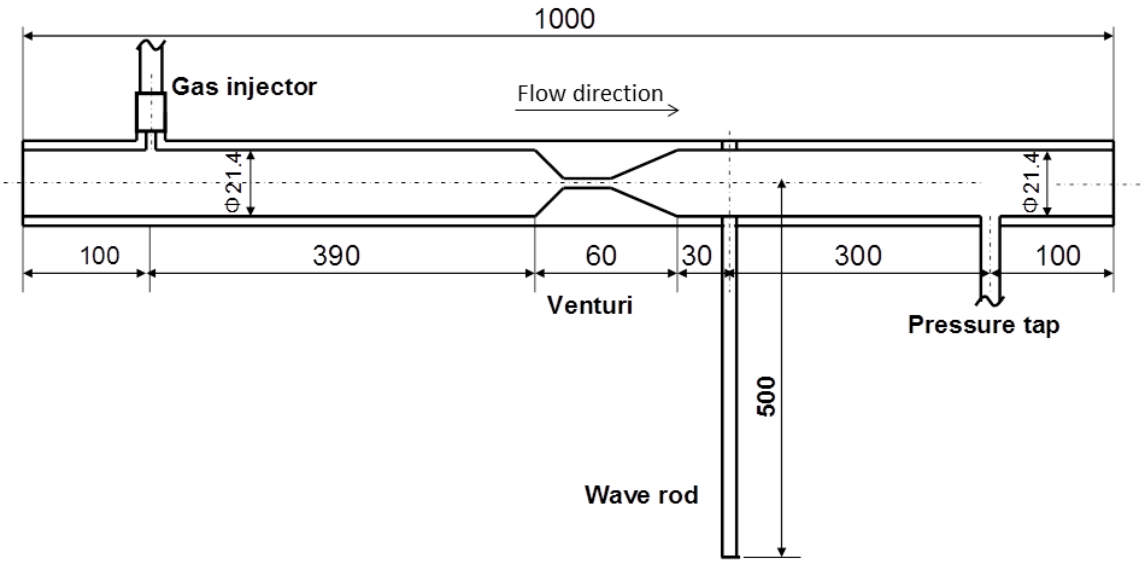

(a) Whole of test section

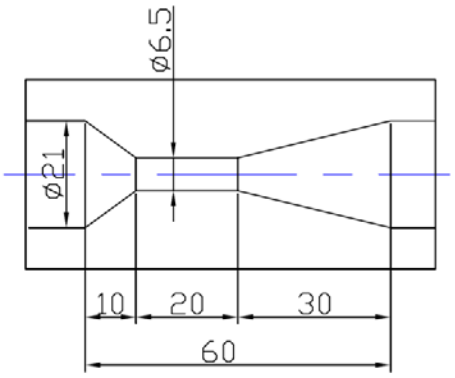

(b) Venturi

Fig. 2.3 Schematics of liquid sodium test section (length is in mm).

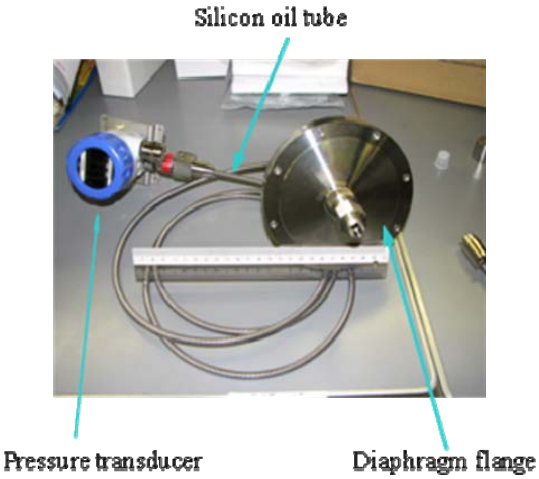

Fig. 2.4 Picture of pressure transducer connected to diaphragm flange.

Fig. 2.5 Picture of accelerometer (Ono Sokki NP-2710).

Fig. 2.6 Picture of charge amplifier (TEAC SA-630).

Fig. 2.7 Picture of data acquisition device (Roga Instruments Plug.n.DAQ).

2.3 Water Loop Apparatus

2.3.1 High Pressure Water Loop Apparatus

Two experimental apparatuses were used for cavitation experiments using water, i.e. high-pressure water loop and low-pressure water loop apparatuses. Both of the loops are located at Research Laboratory for Nuclear Reactors (RLNR) of Tokyo Institute of Technology as shown in **Figs. 2.8** and **2.9**. The high-pressure water loop apparatus can be operated at high temperature since it is made from stainless steel. The loop consists of water main pump, orifice flow meter, pre-heater, venturi channel, condenser, buffer tank and cooler. In this experiment, tap water is supplied to the loop from the water supply tank after being filtered. The circulation flow rate is controlled by the rotation speed of the main pump, and the flow rate is measured by using the orifice flow meter. Pre-heater is used to control the water temperature inside the loop.

The venturi channel has the inner diameter (ID) of 6.5 mm and the outer diameter (OD) of 21 mm. The dimensions of the venturi channel for the high-pressure water loop apparatus are the same as that used for liquid sodium cavitation experiment described above. The cavitation noise signal is measured by using accelerometer (TEAC 601) mounted at the edge of the wave-guide rod connected to the venturi channel. A pressure transducer (Toyoda Koki PMS-5; operating measurement is from 0 MPa up to 1 MPa) is connected at the downstream of the venturi channel to measure the static pressure at downstream. **Figure 2.10** shows the calibration curve of the pressure transducer Toyoda Koki. **Table 2.2** shows the physical and thermodynamics properties of water used for the experiments. The venturi channel for water cavitation experiment using high-pressure water loop was made from stainless steel, and the schematic of the test section is shown in **Fig. 2.12**.

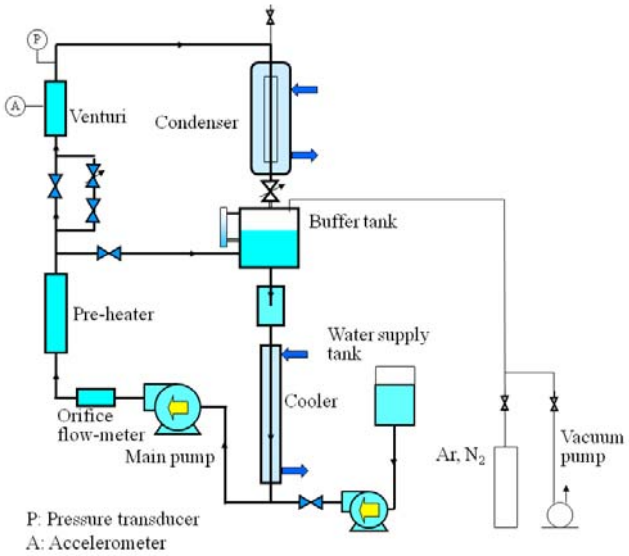

Fig. 2.8 Schematic of the high-pressure water loop apparatus.

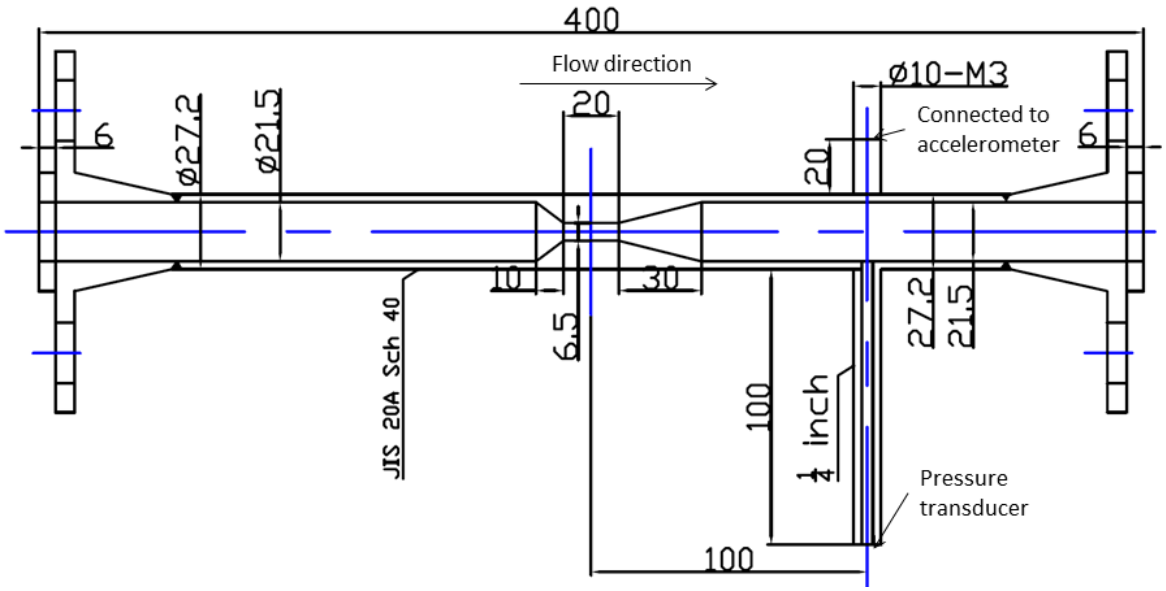

Fig. 2.9 Schematic of the high-pressure water loop venturi test section (length is in mm).

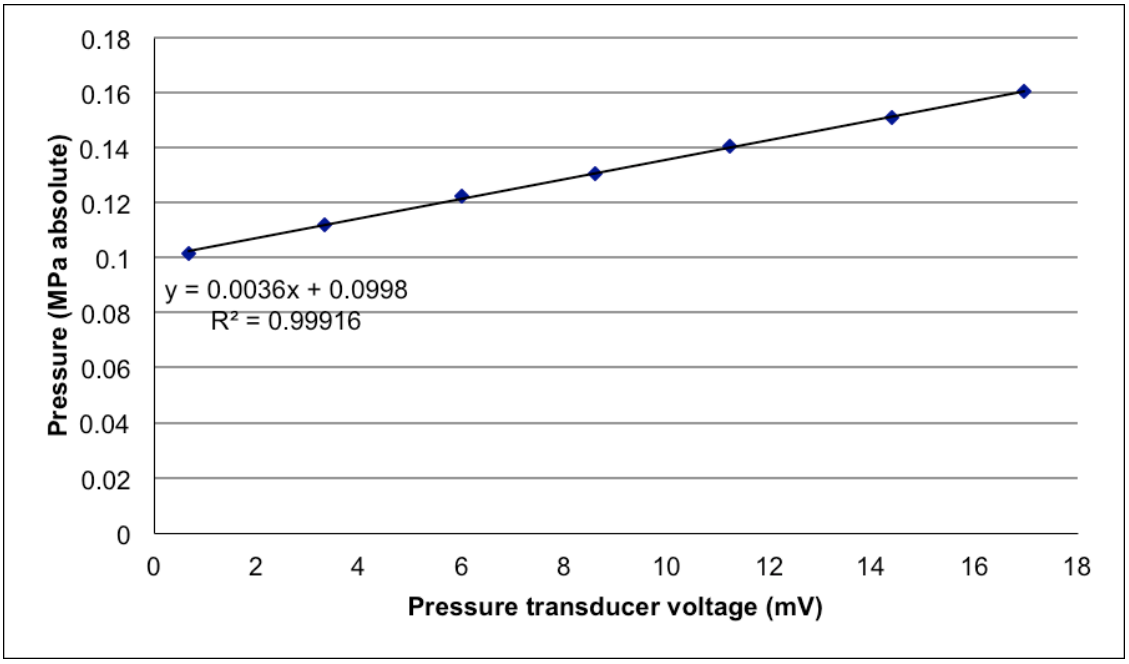

Fig. 2.10 Calibration curve of the pressure transducer.

Fig. 2.11 Picture of accelerometer (TEAC-601).

Table 2.2 Physical and thermodynamics properties of water.

Melting point [°C]	0
Boiling point [°C]	100
Vapor pressure at 56°-90°C [kPa]	16.53 – 70.18
Liquid density at 56°-90°C [kg/m^3]	985.2 – 965.3
Surface tension at 56°-90°C [$N.m^{-1}$]	6.7×10^{-2} – 6.1×10^{-2}
Viscosity at 56°-90°C [Pa.s]	4.96×10^{-4} – 3.14×10^{-4}
Calculated air (21% O_2+79% N_2) solubility at equilibrium from 56°-90°C [ppm]	14.26 - 9.64
Kinematic viscosity at 56°-90°C [$m^2.s^{-1}$]	5.00×10^{-7} – 3.23×10^{-7}
Sound velocity 56°-90°C [$m.s^{-1}$]	1494.3 – 1509.8

2.3.2 Low Pressure Water Loop Apparatus

The low-pressure water loop apparatus operates at room temperature since it is made from acrylic resin. The loop itself consists of four main parts, i.e. water pump, flow meter, water tank and test section as shown in **Fig. 2.12**. The pump to circulate tap water is a canned motor pump supplied by Teikoku Electric MFG. Co., Ltd. This pump is

connected to an inverter to control the rotation speed of the pump. The flow meter is an orifice type and used to measure the flow rate of water based on pressure difference between the upstream and downstream of the flow. This flow meter is connected with a differential pressure transducer whose output signal is proportional to the pressure difference. At the top of the loop, there is water tank to contain water and circulate it during experiment. The venturi channel is mounted below the tank. The venturi test section has the same dimension as that used in sodium cavitation and high-pressure water loop apparatus (OD: 21 mm, ID: 6.5 mm), except that it is made from acrylic. Cavitation experiment in water loop uses tap water that is already filtered. The acoustic noise signal from cavitation and downstream static pressure of the venturi are measured by using accelerometer (TEAC 601) and pressure transducer (Toyoda Koki PMS-5; operating measurement is from 0 MPa up to 1 MPa), respectively. The schematic figure of venturi test section is shown in **Fig. 2.13** below. To observe the dynamics of cavitation bubbles in the venturi channel, a high-speed camera (Photron Fastcam-Net 1000) and stroboscope light (Sugawara Lab. MS-300) are used. The characteristics of the high-speed camera and stroboscope are explained in detail in the appendix.

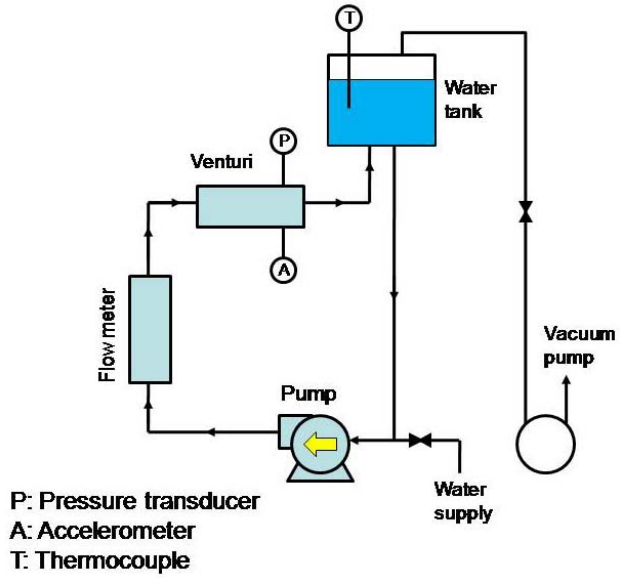

Fig. 2.12 Schematic of the low-pressure water loop apparatus.

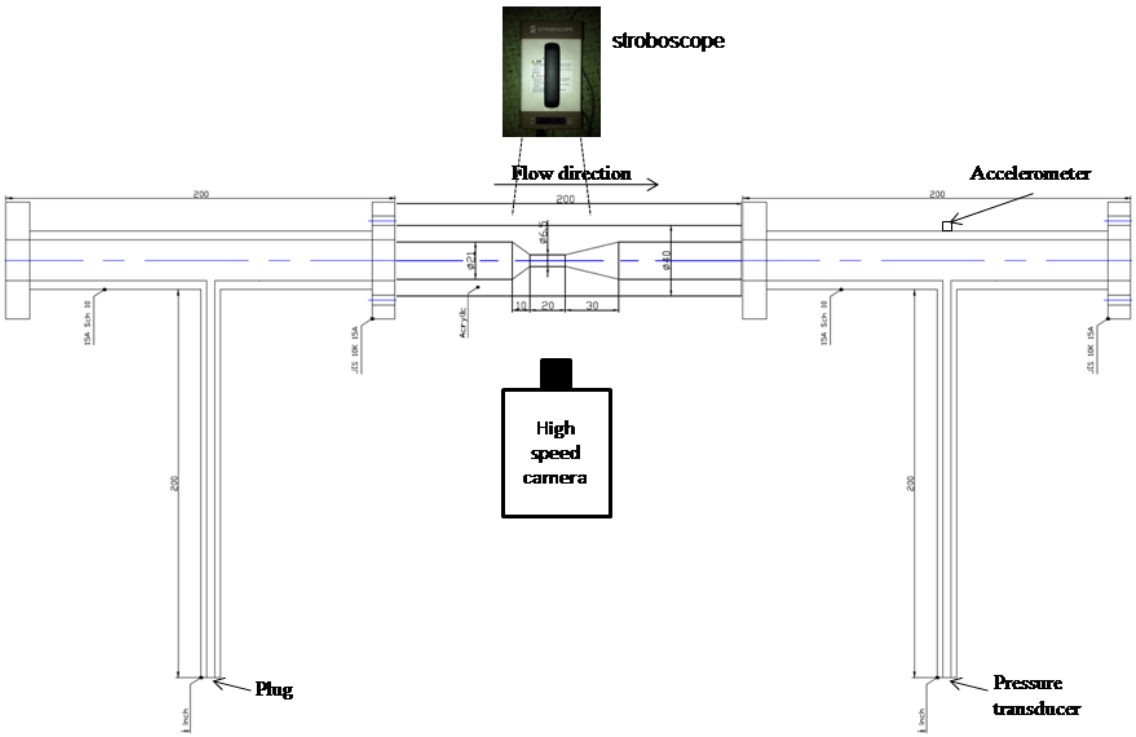

Fig. 2.13 Schematic of the low-pressure water loop venturi test section (length is in mm).

Fig. 2.14 Picture of high-speed camera (TEAC-601).

Fig. 2.15 Picture of stroboscope (Sugawara MS-300).

2.3.3 Dissolved Oxygen Meter

Dissolved gas is any gas that is dissolved in the liquid. The measurement of the dissolved oxygen (DO) in water was conducted by using a dissolved oxygen meter (Horiba OM-51). The specification of the meter is presented in the appendix. The criteria for judging the stability of the DO measurement is within ±3 digit variance after 10 seconds, while for temperature is within ±2°C variance after 10 seconds.

Fig. 2.16 Picture of dissolved oxygen meter (Horiba OM-51).

2.4 Noise Measurement Method

The acoustic noise from the collapse of cavitation bubbles that hit the surface of the test section will be transmitted to the accelerometer. The accelerometer is a shear type accelerometer, which means that the accelerometer will generate charge when there is a force applied in the shear directions. During cavitation, the formation and collapse of cavitation bubbles will produce acoustic noise signals that hit the wall and create vibrations. These vibrations on the wall are measured by the accelerometer creating charge signals. These charge signals will be amplified by the charge amplifier (TEAC SA-630). The output voltage of the charge amplifier will enter the data acquisition device (Roga Instruments, Plug.n.DAQ) before being recorded by using PC (Visual Analyzer, Silanumsoft.org) to analyze the acoustic noise intensity and spectrum. The schematic of the noise measurement is shown in **Fig. 2.17**. The wave-guide rod is placed 30 mm from the venturi channel exit because it is expected at around this part the cavitation bubbles will be collapsed and produce acoustic sound noise that can be recorded. The changes of the acoustic noise intensity and acoustic sound intensity level with the change of the

distance are presented in **Figs. 2.18** and **2.19**. The value of the sound intensity increases inversely squared with increasing distance from the sound source as stated by

$$I_2 = I_1 \cdot \left(\frac{r_1}{r_2} \right)^2$$

where I is the sound intensity [W/m^2] and r [m] is distance from the sound source. The sound intensity level (dB) is calculated by

$$SIL = 10 \log_{10} \cdot \left(\frac{I}{I_0} \right)$$

where $I_0 = 10^{-12}$ W/m^2 ≡ 0 dB is the standard reference sound intensity. **Figure 2.19** shows that increasing the distance twice will reduce the sound intensity level of about 6 dB that is still in the range of the measurement equipment. The difference becomes smaller and can be neglected if the sound travels in solid for instance in steel with the sound speed of about 6100 m/s, because sound travels better in solid than in air that has the value of about 343 m/s at 20°C and 1 atm. From the accuracy of each equipment used, (accelerometer, charge amplifier, data acquisition, pressure transducer), the total accuracy of this experiment is estimated to be around ± 13.25%.

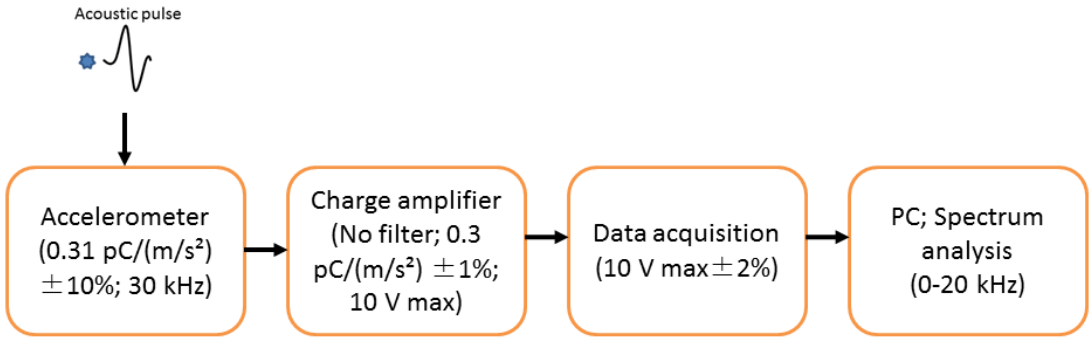

Fig. 2.17 Schematic of the noise measurement.

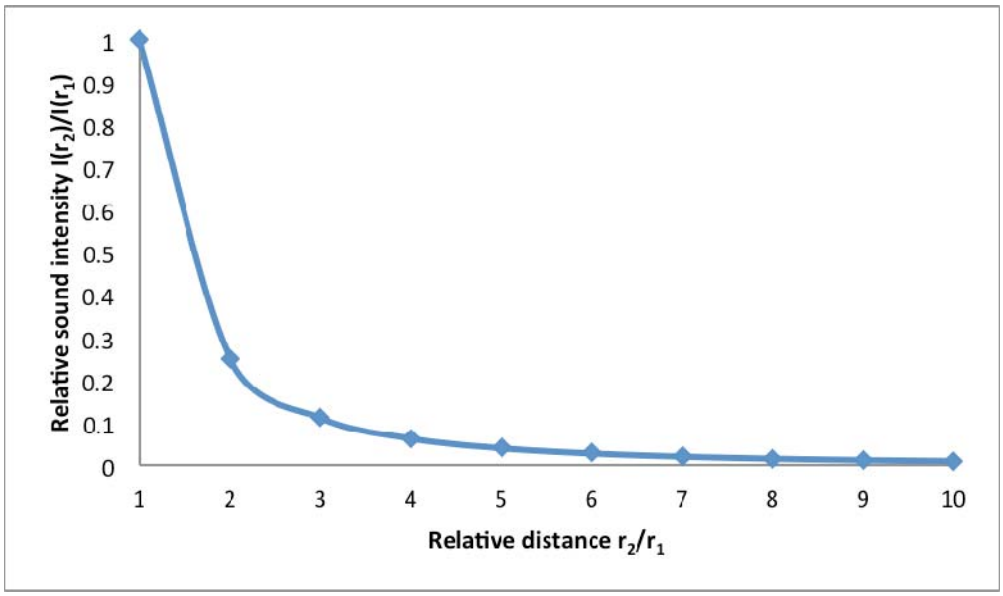

Fig. 2.18 Relative change of the sound intensity with distance.

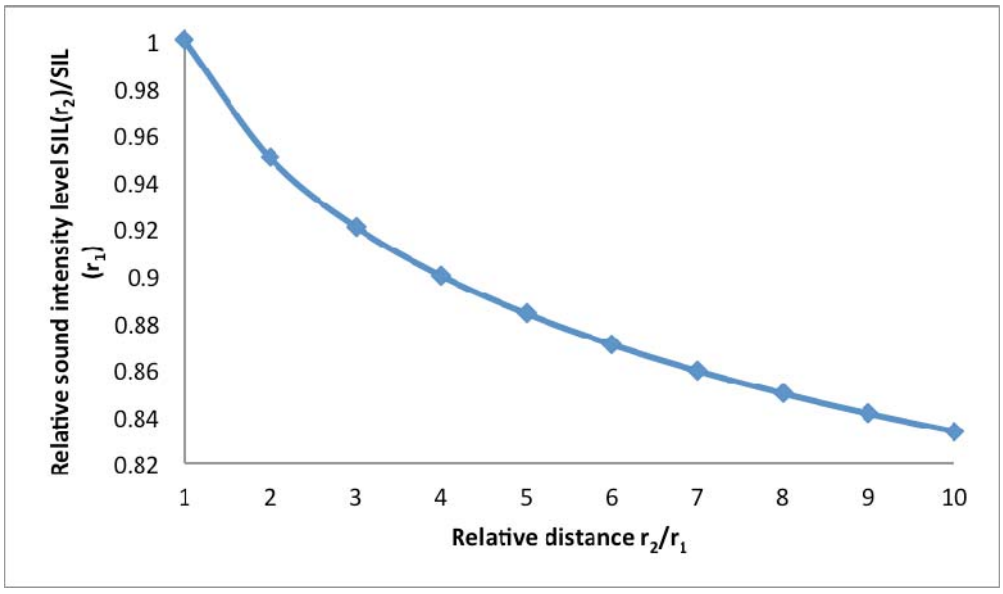

Fig. 2.19 Relative change of the sound intensity level with distance.

2.5 Experimental Procedure

2.5.1 Experimental Procedure of Sodium Cavitation

The experimental procedure for the sodium cavitation experiment to measure its noise and onset conditions is explained as follows:

1) Before the cavitation noise measurement, hitting test of the test section using hammer was conducted in no circulating condition to determine the resonance frequency of the test section.
2) The sodium loop was circulated at a desired temperature at 200°C.
3) The circulation was stopped shortly by turning off the EMP, and then the argon cover gas pressure in the expansion tank was controlled to 0.061 MPa-a and kept it constant. The term of the stagnant pressure used later was defined by the argon cover gas pressure in the expansion tank measured when the liquid sodium was not circulated.
4) When all the experimental conditions were satisfied, the EMP was turned on again to circulate the liquid sodium.
5) Sodium flow rate was increased gradually by increasing EMP voltage until cavitation occurred in the test section and the data were acquired. Cavitation noise was measured for 1 second with sampling frequency of 40,960 Hz. The frequency spectrum of the noise was recorded in the frequency range of 0-20,480 Hz. After all the necessary data were collected, the procedure was repeated again for higher stagnant pressure condition up to 0.181 MPa-a.
6) Next, the procedure was repeated for higher sodium temperature of 300°C and 400°C, respectively.

2.5.2. Experimental Procedure of Water Cavitation at High Temperature

For the water cavitation case at high temperature, the experiments were conducted in water at temperatures of 56°, 74° and 90°C and atmospheric pressure using the high pressure water loop apparatus. These temperatures were chosen because they had the same kinematic viscosity with those of liquid sodium at 200°, 300° and 400°C. The geometry of the venturi channel used for the experiment is the same between sodium and water that is 6.5 mm ID and 21 mm OD. The detailed experimental procedure in water at high temperature is explained as follows:

1) At the beginning, the concentration of the dissolved oxygen (DO) in the water was measured first by using a dissolved oxygen meter (Horiba OM-51). The measurement was conducted three times and the results were averaged.
2) Next, the water at the loop was circulated at low flow rate.
3) Using pre-heater, the temperature of the water was increased to a desired level of experimental condition, i.e. 56°C and kept constant during experiment.
4) After that the flow rate of the main pump was increased gradually until cavitation occurred at the test section that was indicated by its higher noise intensity. The onset cavitation condition was determined by an increase of the noise intensity, since the occurrence of cavitation created bubbles that collapsed and produced sound noise. The data (noise, pressure, temperature and flow rate) were then recorded on a PC to be analyzed later. All the experiments were conducted at atmospheric condition of 0.101 MPa-a and using air as the cover gas in the water loop.

5) The experiment was repeated again for 74°C and 90°C. The experiments were first conducted for higher DO concentration, i.e. normal DO concentration in tap water without considering to reduce the DO concentration.
6) After the experiment at 56°, 74° and 90°C and higher DO concentration finished, next the experiments were conducted at lower DO concentration, i.e. below the normal DO concentration of tap water. Lower DO condition was achieved by heating the water at the loop at 90°C and vacuuming several days until the DO concentration decreased (about 1 week). The DO concentration was assumed not to change during the experiment. In order to keep the DO concentration low, after each experiment the loop was vacuumed to remove the remaining air.
7) The DO concentration after heating and vacuuming the loop was measured again and the experimental procedure was repeated again from step 2 to step 5.

2.5.3. Experimental Procedure of Water Cavitation at Room Temperature

The experimental procedure for water cavitation experiment at room temperature using the low-pressure water apparatus is explained as follows:

1) First, the concentration of the dissolved oxygen (DO) in the water was measured by using a dissolved oxygen meter (Horiba OM-51). The measurement was conducted three times and the results were averaged.
2) Second, the loop pressure was reduced by using a vacuum pump to 0.062 MPa-a so that cavitation can easily occurred inside the venturi channel.
3) Third, the flow rate of the main pump was increased gradually until cavitation bubbles formed at the venturi test section made from acrylic resin.

4) Next, stroboscope lamp (Sugawara Lab. MS-300) and high speed camera (Photron Fastcam-Net 1000) was used to obtain the dynamics of the bubbles during cavitation conditions from onset to develop. The stroboscope flashing frequency was operated at 500 Hz with flashing duration of 2.4 μs and flash energy of 5 W. The high speed camera was operated at 500 fps (frame per second). This will give an image with the size of 512 x 240 pixels and recording time of 2.1 seconds. Because the minimum shutter speed of the high speed camera is about 4 times larger than the duration of the stroboscope flashing, therefore it has no effect on the recording process as shown in the **Fig. 2.20**. The picture data were then stored into a computer to be analyzed.

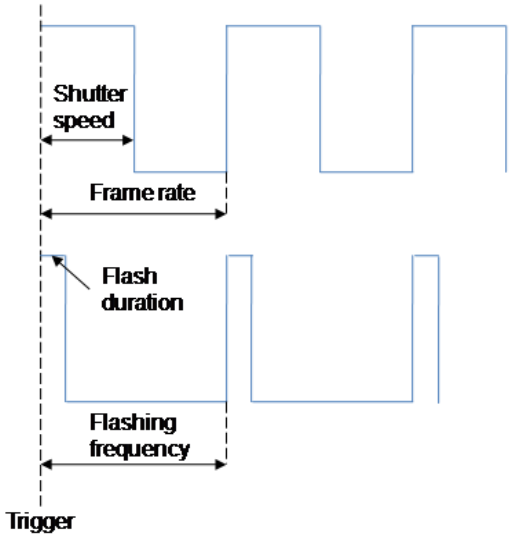

Fig. 2.20 Schematic of the high speed camera recording.

2.5.4 Experimental Procedure of Cavitation Erosion in Sodium

The detailed experimental procedures for sodium cavitation erosion experiment are explained as follows:

1) Sodium was circulated in the sodium flow loop with a desired temperature of 200°C.
2) The circulation was stopped shortly by turning off the EMP (Electromagnetic Pump). Then, the cover gas pressure in the expansion tank was controlled to the desired experimental condition by controlling argon gas in the expansion tank to 105-110 kPa (stagnant pressure). The stagnant pressure was defined by the measured argon gas pressure in the expansion tank when the sodium was not circulated.
3) The EMP was turned on again to circulate the sodium.
4) The EMP voltage was increased gradually to increase the flow rate to 27-28 L/min until cavitation became developed in the test section, which was indicated by its distinct and high noise sounds. A developed cavitation condition was set up, where the cavitation coefficient *K* defined by **Eq. (3-1)** had the value of 0.59-0.51.

$$K = \frac{P_0 - P_v}{\frac{\rho}{2}\left(V_1^2 - V_0^2\right)} \quad \text{.....(3-1)}$$

where P_0 is static pressure measured at the downstream of the venturi channel with the measured value of 0.042-0.052 MPa-a. P_v is the saturated vapor pressure of the sodium at 200°C. ρ is sodium density at 200°C. V_0 and V_1 are obtained from the measured flow rate divided by the maximum diameter (21 mm) and the minimum diameter (6.5 mm) of the venturi channel, respectively. The cavitation coefficient has been employed as a non-

dimensional parameter for determination of onset of cavitation condition. The cavitation coefficient expresses the degree of approach of local pressure at venturi part P_1 relative to the saturation pressure P_v of the liquid due to an increase of dynamic pressure. **Equation (3-1)** is derived from the Bernoulli`s equation for incompressible flow. It states that for inviscid flow an increase on the velocity of the fluid occurs simultaneously with the decrease of pressure as stated by:

$$P_1 + \frac{\rho}{2}V_1^2 = P_0 + \frac{\rho}{2}V_0^2 = \text{constant} \quad \text{.....(3-2)}$$

The cavitation coefficient *K* is defined by

$$K = \frac{P_0 - P_1}{\frac{\rho}{2}\left(V_1^2 - V_0^2\right)} \quad \text{.....(3-3)}$$

If P_1 approaches P_v, then **Eq. (3-3)** can be stated as **Eq. (3-1)** above. For $V_1 >> V_0$

$$K \approx \frac{P_0 - P_v}{\frac{\rho}{2}V_1^2} \quad \text{.....(3-4)}$$

The physical meaning of cavitation coefficient is:

- If K > 1; theoretically no vapor is formed because local static pressure P > saturated vapor pressure. Therefore no cavitation bubbles are formed in the liquid.
- If K = 1; theoretically vapor starts to form because local static pressure P = saturated vapor pressure. Cavitation bubbles start to form in the liquid.
- If K < 1; theoretically more vapor will be formed because local static pressure P < saturated vapor pressure. More cavitation bubbles will be formed due to reduce pressure. In general, cavitation takes place when cavitation coefficient *K*

approaches unity. Therefore, it could be used as a prediction of cavity bubbles formation.

In sodium cavitation erosion experiment, the saturated vapor pressure of sodium at 200°C is calculated by using the following equation **[2-3]**:

$$\ln P = 11.9463 - 12633.73/T - 0.4672 \ln T \quad \text{.....(3-5)}$$

where P is in MPa and T is in K. The density is calculated by **[2-3]**:

$$\rho_l = \rho_c + f\left(1 - \frac{T}{T_C}\right) + g\left(1 - \frac{T}{T_C}\right)^h \quad \text{.....(3-6)}$$

where

$\rho_c = 219.0$
$f = 275.32$
$g = 511.58$
$h = 0.5$
$T_C = 2503.7\ \text{K}$

The cavitation coefficient K with the value of 0.59-0.51 (developed cavitation condition) was maintained for 600 hours during the experiment. After the experiment, the venturi channel was cut and washed by ethanol and water to remove the remaining sodium that might adhere to the surface of the test section. Then the surface of the test section was analyzed by using an optical micrograph and SEM (Scanning Electron Microscope).

2.6 Conclusion

Experimental apparatuses and venturi channel test section for sodium and water cavitation have been designed and utilized for this study. The noise measurement was

successfully set up to measure the cavitation noise as well as for the prediction of cavitation onset in sodium and water.

2.7 References

2-1 Fink, J. K. and Leibowitz, L., (1995), Thermodynamic and Transport Properties of Sodium Liquid and Vapor, ANL/RE-95/2.

2-2 Koivula, T., (2000), On Cavitation in Fluid Power, Proceedings of 1st FPNI-PhD Symposium, pp. 371-382.

2-3 Fink, J. K. and Leibowitz, L., (1995), Thermodynamic and Transport Properties of Sodium Liquid and Vapor, ANL/RE-95/2.

CHAPTER 3

CHARACTERISTICS OF ONSET CONDITION IN SODIUM AND WATER CAVITATION

3.1 Introduction

The prevention of cavitation is one of the most important necessities for the hydrodynamic design of the sodium-cooled fast reactors (SFR). There is possibility of cavitation in the flow components where flow channel area has contraction and as a result local velocity becomes higher and static pressure becomes lower than the saturation pressure, such as in the flow regulating system that consists of the slits of the connecting tubes of the inner structure and the orifices of the entrance nozzles of the fuel assemblies. Furthermore, the innovative compact design for more economic SFR leads to higher velocity of primary coolant, which could promote the occurrence of cavitation since local static pressure in the reactor vessel and piping goes below the saturation pressure of the coolant because of the increasing velocity.

Cavitation starts when the small bubbles grow into larger ones and collapse. The formation of small cavitation bubbles in flow components is an important phenomenon in cavitation stages before the bubbles can grow into violent ones and damage or erode the surface. This first stage in cavitation phenomena is known as the onset or inception of cavitation. The onset cavitation condition can be judged from the change of the audible sound noise. As the sound noise changes during the onset condition, the flow and fluid properties (static pressure, vapor pressure, density and velocity) can be grouped into one non-dimensional parameter known as cavitation coefficient or number K similar to that used in water cavitation. This cavitation coefficient or number can be used to predict the occurrence of cavitation in the flow. Since theoretically when cavitation starts to occur (onset condition) the value of cavitation coefficient is 1 (unity). Therefore any values lower than 1 indicates the existence of cavitation in the flow. Meanwhile, many

researchers have conducted the study of the cavitation by acoustic noise measurement. For instance, Sato and Kakutani **[3-1]** in his work found a relation between cavitation inception and cavitation coefficient and the cavitation number is influenced by the air content in water. Coubiere **[3-2]** carried out a work to determine the onset cavitation condition using sodium and found that the onset cavitation coefficient in case of orifice test section is around 2-3 and will change with the change of downstream pressure and free argon gas content. He also found that the ratio of the noise intensity increases rapidly in case of cavitation. Lin and Katz **[3-3]** in their experiment in water jet cavitation stated that the inception of cavitation are affected by the jet velocity, dissolved air content, nozzle geometry and size, boundary layer tripping and external excitation. Hammitt **[3-4 and 3-5]**, Hammitt, *et al* **[3-6 to 3-8]** and Ericson **[3-9]** conducted extensive researches on the effect of air/gas content on cavitation inception number in water and mercury. Hammitt, *et al* **[3-6]** stated that the effect of gas content (entrainment) upon cavitation initiation number for liquid metal (mercury) in a ½ inch venturi appears to be relatively small between the minimum attainable gas (around 0.2 ppm) and around 2 ppm for argon, but becomes a factor of around 2 or more for gas contents in the 3-4 ppm range. This has been demonstrated by the present data to be the case for mercury temperatures ranging from room temperature to about 400°F (around 204.44°C), at a single velocity and in the steel venturi. Hammitt **[3-4 and 3-5]** and Hammitt, *et al* **[3-7 and 3-8]** also reviewed the effect of air content on the cavitation coefficient for initiation of cavitation in water. In general, an increase in air content causes an increase in inception cavitation coefficient. Also the importance of air content upon inception cavitation coefficient depends upon the type of cavitation, i.e. bubble, laminar (steady cavity), vortex cavitation, etc., where the

bubble cavitation being the most sensitive. The type of cavitation found depends on geometry and other flow parameters. Ericson **[3-9]** also found the same result with Hammitt **[3-6]** in case of mercury with injected argon gas in stainless steel venturi where the trend of increasing cavitation coefficient number can be seen if the argon gas content rises above 2%.

Therefore in the present study, the onset condition of cavitation in sodium is investigated using venturi test section since there are limited data in the past concerning onset condition of sodium cavitation. This lack of data can be a major obstacle in developing SFR in the future. The results of the experiment are compared with the onset condition in water cavitation conducted for the same test section geometry. This is conducted in order to understand the differences of onset condition between sodium and water cavitation. CFD and high speed photography are also used in order to understand the detail of the cavitation process and the dynamics of cavitation bubbles in a venturi.

3.2 Experiment

3.2.1 Experimental Apparatus

In case of sodium cavitation, the experiment was conducted by using a sodium loop facility at Sukegawa Electric Co., Ltd. Argon gas was used as a cover gas pressure in the loop during the experiment. The downstream static pressure was measured by using a pressure transducer and the flow rate of liquid sodium was measured by using an electromagnetic flow meter. The test section for this experiment is a venturi made from 316 SS with an inner diameter of 6.5 mm, an outer diameter of 21 mm, and a length of 20 mm. The detail explanation of this apparatus can be found in **Chapter 2.1**.

While for the water cavitation, the experiment was conducted by using high-pressure water loop apparatus as explained in detail in **Chapter 2.2.1**. The test section used has the same diameter as that used for sodium cavitation experiment. It is also made from stainless steel since it will be used at temperatures higher than room temperature.

3.2.2 Experimental Condition

The experimental conditions for this experiment are explained in **Tables 3-1** and **3-2**. Since it is difficult to measure the gas solubility, therefore the solubility of air and argon gas in water and sodium was calculated analytically for estimation. The calculated solubility of air and argon gas in water from 10°-90°C and in sodium from 200°-400°C is shown in **Fig. 3.1** below. The minimum Re number in case of sodium during cavitation experiment at the outer diameter of the test section (21 mm) was around 37700 and at the inner diameter of the test section or venturi (6.5 mm) was around 122000. While the minimum Re number in case of water during cavitation experiment at the outer diameter of the test section (21 mm) was around 16000 and at the inner diameter of the test section or venturi (6.5 mm) was around 53800. The Re number during experiment is higher than 4000, therefore the flow was turbulent.

Table 3.1 Experimental conditions of sodium cavitation experiment.

Na Temperature [°C]	Stagnant Pressure in the Expansion Tank, MPa absolute [MPa-a]
200-400	0.061-0.181

Table 3.2 Experimental conditions of water cavitation experiment.

Water Temperature [°C]	Stagnant Pressure in the Buffer Tank, MPa absolute [MPa-a]
56-90	0.101 (atmospheric pressure)

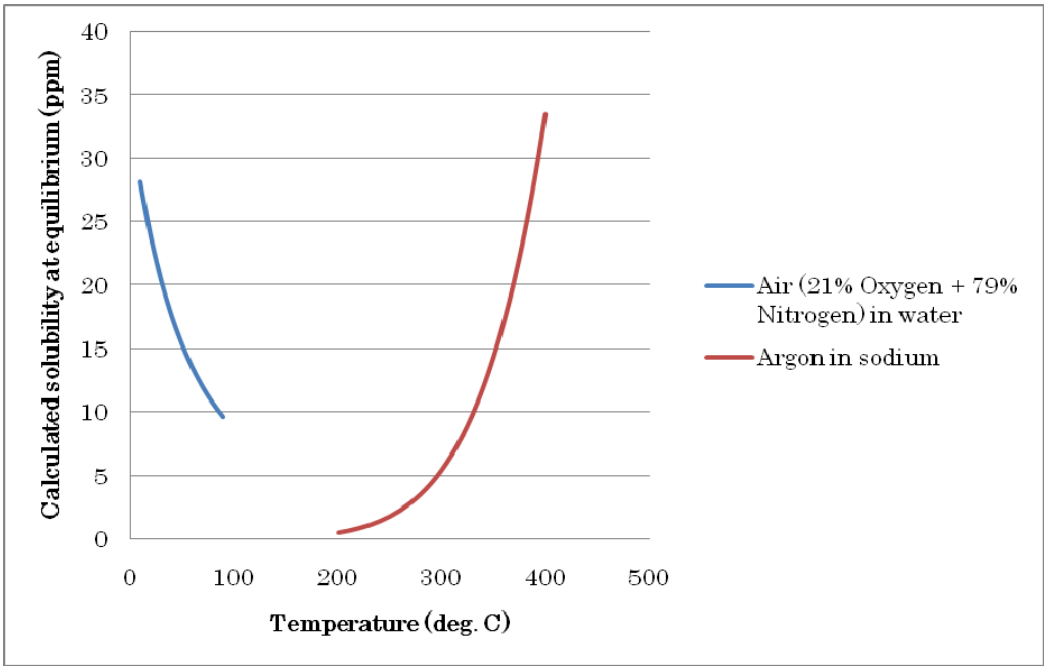

Fig. 3.1 Calculated solubility of air and argon in water and sodium at equilibrium, respectively.

3.3 Definition of Cavitation Coefficient

For any cavitation process, cavitation coefficient has been employed as a non-dimensional parameter for the judgment of cavitation onset. The cavitation coefficient expresses the degree of approach of local pressure P_1 relative to the saturation pressure P_v of the liquid due to an increase of dynamic pressure. Cavitation coefficient K is

derived from the Bernoulli`s equation for incompressible flow. The cavitation coefficient K is defined by

$$K = \frac{P_0 - P_v}{\frac{\rho}{2}\left(V_1^2 - V_0^2\right)} \quad \text{.....(5-1)}$$

In the experiment, the value of V_0 and V_1 is obtained from the measured flow rate divided by the maximum cross section (21 mm) and the minimum cross section (6.5 mm) of the venturi, respectively. In general, cavitation takes place when cavitation coefficient K approaches unity. Therefore, it could be used as a prediction of cavity bubbles formation.

3.4 Results and Discussion

3.4.1 Onset of Sodium Cavitation in Venturi Channel

The results of the cavitation experiment in flowing liquid sodium are presented in **Figs. 3.2** to **3.5**. **Figure 3.2 (a) and 3.2 (b)** show the result of the acoustic noise intensity over cavitation coefficient K calculated by **Eq. (3-1)** at 300° and 400°C. The results show that there are two different regions, i. e., the no cavitation region marked with the vacant symbols for cavitation coefficient $K>1$ and cavitation region marked with the solid color symbols for cavitation coefficient $K<1$. This figure shows that the noise intensity is relatively low when K is much higher than unity and expected there is no cavitation in the venturi region. The noise intensity begins to rise rapidly when K approaches unity, which implies the onset of cavitation. The relation of the onset of cavitation and the value of the cavitation coefficient K means the validity of the cavitation onset theory based on the Bernoulli's equation in incompressible flow. It has been also found that noise intensity increases at cavitation inception for orifice test section in sodium, but with a value higher

than 1 **[3-10]**. The differences between the present results and those of **[3-10]** can be attributed to the difference in free argon gas content which could act as nucleation sites for the growth of cavitation bubbles. According to **[3-10]**, the inception value is influenced by the change of free argon gas content in the liquid sodium flow. Based on **[3-11]**, the calculated argon gas content in liquid sodium ranging from 200°-400°C is estimated to be 4.5 x 10^{-3}-2.8 ppm, which is lower compared to 8-120 ppm in **[3-10]**.

Under developed cavitation condition where K is lower than unity, the noise intensity is relatively constant without changing drastically with the change of K caused by the choking of the flow. The change of the stagnant pressure in the expansion tank has no significant effect on the noise intensity in developed cavitation conditions. The noise intensity at 400°C has no significant differences with that at 300°C, which is around 43 dB rms (root mean square) at developed cavitation conditions.

The onset cavitation condition in this experiment was judged by hearing the rapid knocking sound of cavitation on the cavitation test section and observing the spectrum analyzer monitor for any changes on the noise amplitude signals. It is concluded that cavitation starts to occur (onset of cavitation) when there is a sudden increase on the amplitude of the acoustic noise signal, and rapid knocking sounds in the test tube. The onset condition cannot be judged directly from observation of the growth of cavity bubbles since sodium is opaque (non-transparent).

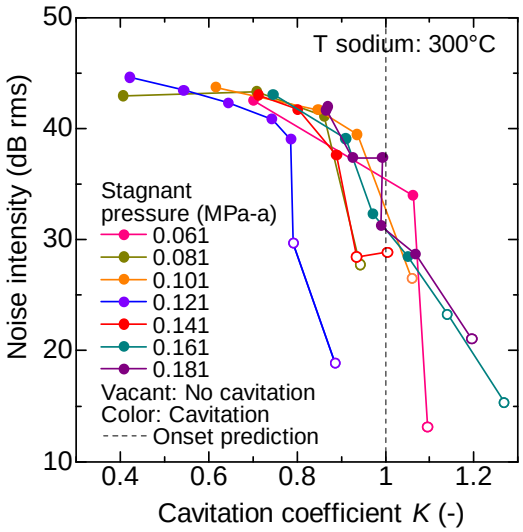

Fig. 3.2 (a) Noise intensity as a function of cavitation coefficient at 300°C.

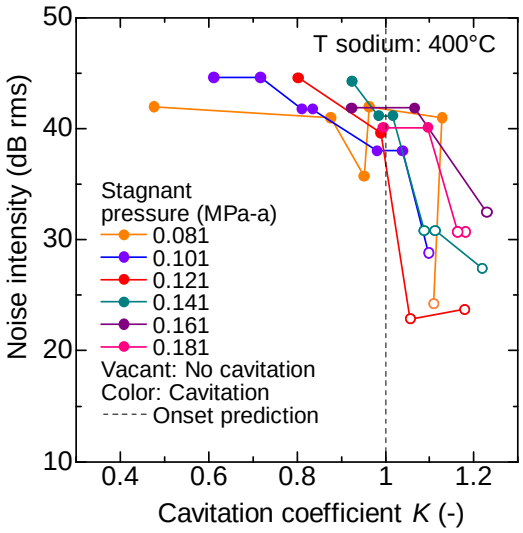

Fig. 3.2 (b) Noise intensity as a function of cavitation coefficient at 400°C.

Figures 3.3 to **3.5** show the results of no cavitation and occurrence of cavitation on the map of the venturi velocity, i. e., the sodium superficial velocity in the venturi part, [62]

as a function of cavitation coefficient at 200°, 300° and 400°C, respectively. For every temperature rise, it is clear that the stagnant pressure in the expansion tank has influence on the velocity in the venturi part at the onset of cavitation. The onset cavitation velocity at the venturi increases with the increase of the stagnant pressure conditions in the expansion tank. For instance, at 200°C the onset cavitation velocity is around 10 m/s for stagnant pressure at the expansion tank of 0.061 MPa-a and around 16 m/s for stagnant pressure at the expansion tank of 0.181 MPa-a. The velocity then becomes relatively constant in the developed cavitation conditions. It is concluded from these figures that the formation of cavitation bubbles is suppressed at higher stagnant pressure, therefore the onset cavitation velocity in the venturi increases as predicted from **Eq. (3-1)**. Moreover, these figures show that cavitation coefficient at the onset cavitation condition is nearly equal to unity. However, an increase in temperature shifts the cavitation coefficient to a value a little higher than unity. This is probably caused by an increase of sodium vapor pressure that increases the threshold for onset cavitation condition or because of the increased argon gas concentration that dissolved into sodium, since solubility of argon gas increases with the increase of sodium temperature as observed and calculated by using equation from **[3-11]**. It is also found from these figures that there are two distinct regions, i. e., no cavitation region for $K>1$, and cavitation region for $K<1$.

It is found in **Figs. 3.3** to **3.5** that even if the cavitation coefficient is decreased to below unity by decreasing downstream static pressure, the sodium superficial velocity in the venturi is nearly constant without changing significantly. These phenomena are similar to the choked flow or two-phase critical flow. For cavitation in a venturi, the choked flow is caused by the decrease of the sound velocity in the liquid sodium due to

the formation of cavitation bubbles. This formation of cavitation bubbles will restrict the liquid sodium velocity to increase further, therefore the sodium liquid velocity is relatively constant.

The physical phenomena of sodium cavitation can be explained in this way. When cavitation coefficient *K* is higher than unity, the liquid static pressure is still higher than the saturated vapor pressure of the sodium at a given temperature. At this condition the theoretically no cavitation bubbles will be formed. Therefore the acoustic noise intensity is still relatively low. If the sodium velocity is increased, the static pressure will reduce further based on the pressure-velocity relationship of the Bernoulli's equation. When cavitation coefficient *K* is equal to unity, the liquid static pressure of sodium will be equal to its saturated vapor pressure. At this condition cavitation bubbles start to form because of the vaporization process. This formation of cavitation bubbles will create high acoustic noise intensity because of the rapid formation and collapse of cavitation bubbles. This condition is known as the onset of cavitation. Increasing the liquid sodium velocity further will decrease the liquid sodium static pressure lower than its saturated vapor pressure and more cavitation bubbles will be formed that increase the phenomena of cavitation. At this condition the value of cavitation coefficient *K* is lower than unity and the cavitation condition is known as developed cavitation condition. The acoustic noise will increase. If there is some dissolved gas in the liquid, the dissolved gas could come out from the liquid to create small micro nucleation sites. This micro nucleation sites will increase the onset condition because of gas expansion at low pressure. Therefore cavitation could occur early.

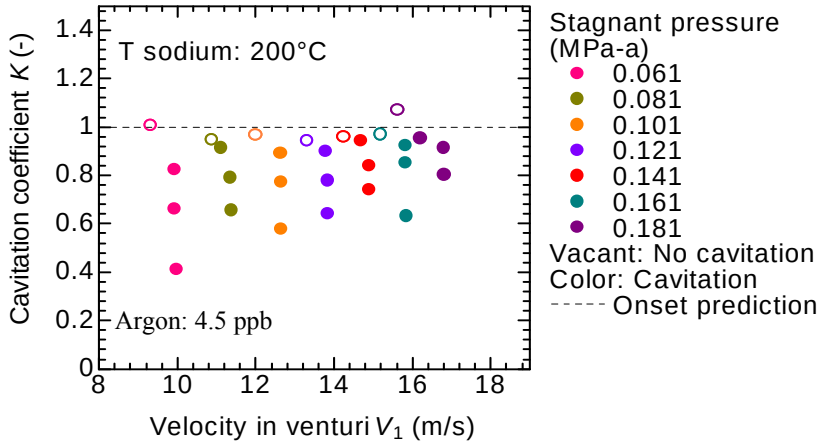

Fig. 3.3 Cavitation coefficient *K* as a function of venturi velocity at 200°C.

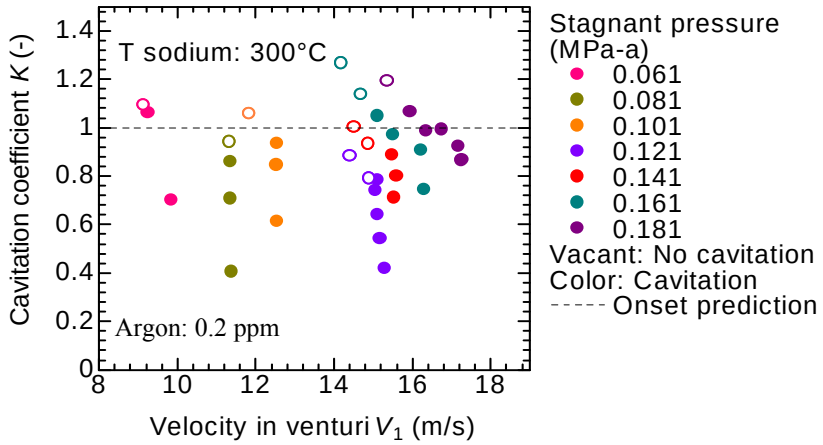

Fig. 3.4 Cavitation coefficient *K* as a function of venturi velocity at 300°C.

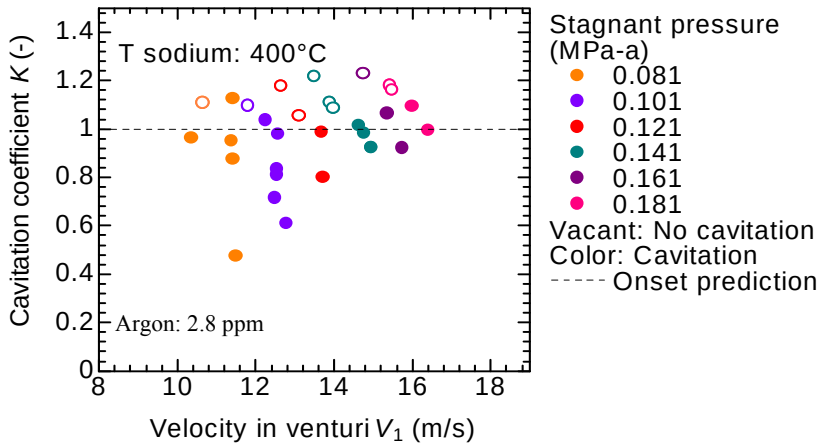

Fig. 3.5 Cavitation coefficient *K* as a function of venturi velocity at 400°C.

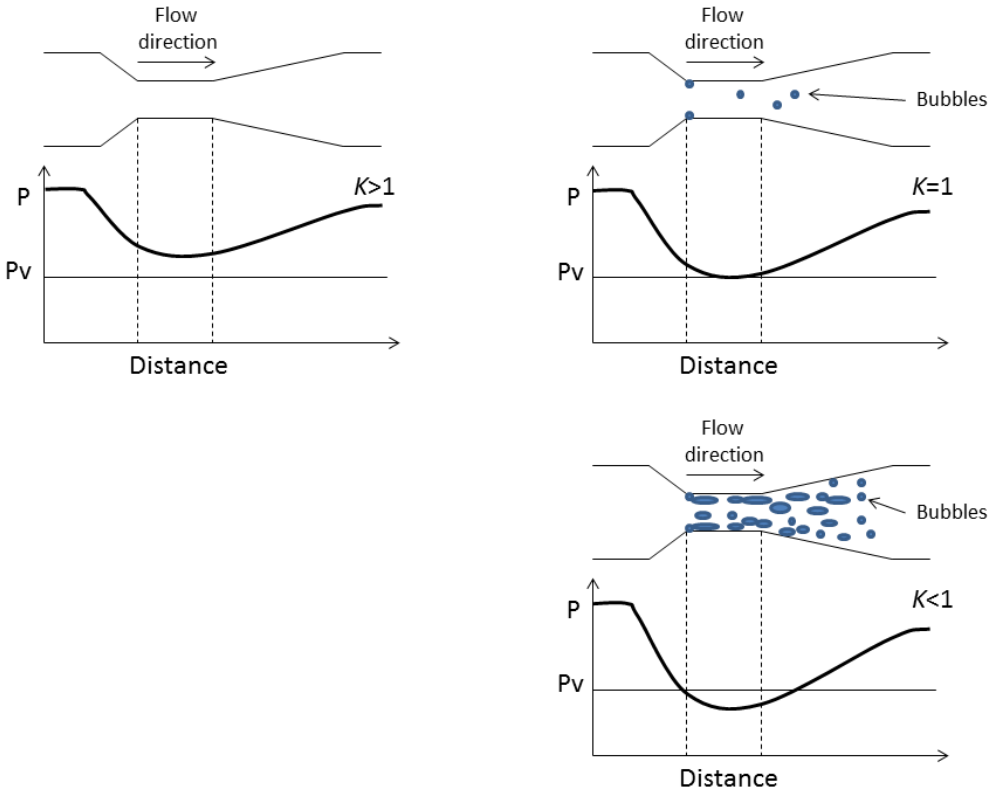

Fig. 3.6 Schematic of onset and developed cavitation formation.

3.4.2 Comparison of Cavitation Onset in Sodium and Water for Venturi Channel

Cavitation process in sodium and water is different due to different important factors such as velocity and pressure of the flow, saturated vapor pressure, density, surface tension, viscosity and dissolved gas in liquid. **Tables 3.3** and **3.4** show the different properties between sodium and water that can influence onset condition. The similarity of local pressure can be expressed using non-dimensional parameter known as cavitation coefficient *K*. This cavitation coefficient *K* is the function of pressure, saturated vapor pressure, density, and velocity. And the similarity of single phase flow can be expressed to non-dimensional parameter known as Re number that is the function of velocity, diameter and kinematic viscosity. However to consider all the fluid and flow properties in the experiment is very difficult. Therefore only kinematic viscosity and geometry of the test section are similarly considered. The kinematic viscosity of sodium at 200°-400°C is equal to the kinematic viscosity of water at 56°-90°C that has the value of $5.01 \times 10^{-7} – 3.23 \times 10^{-7}$ m^2/s. The test section geometry used in sodium is equal to the test section geometry used in water, which is 21 mm OD and 6.5 mm ID. And the results between sodium and water cavitation are compared based on these similarities at no cavitation, onset of cavitation and developed cavitation. In this experiment, the results are considered satisfy when the value of cavitation coefficient *K* is lower than unity that theoretically means developed cavitation condition, and when the acoustic noise intensity measured during experiment is constant.

Table 3.3 Thermodynamics properties of sodium.

Vapor pressure at 200°-400°C [kPa]	2.2×10^{-5} - 5.2×10^{-2}
Liquid density at 200°-400°C [$kg.m^{-3}$]	903.0 - 857.7
Surface tension at 200°-400°C [$N.m^{-1}$]	1.90×10^{-1} – 1.69×10^{-1}
Viscosity at 200°-400°C [Pa.s]	4.52×10^{-4} – 2.77×10^{-4}
Calculated argon gas solubility at equilibrium from 200°-400°C [ppm]	4.46×10^{-3} – 2.83
Kinematic viscosity at 200°-400°C [$m^2.s^{-1}$]	5.01×10^{-7} – 3.23×10^{-7}
Sound velocity 200°-400°C [$m.s^{-1}$]	2462.2 – 2366.2

Table 3.4 Thermodynamics properties of water.

Vapor pressure at 56°-90°C [kPa]	16.53 – 70.18
Liquid density at 56°-90°C [kg/m^3]	985.2 – 965.3
Surface tension at 56°-90°C [$N.m^{-1}$]	6.7×10^{-2} – 6.1×10^{-2}
Viscosity at 56°-90°C [Pa.s]	4.96×10^{-4} – 3.14×10^{-4}
Calculated air (21% O_2+79% N_2) solubility at equilibrium from 56°-90°C [ppm]	14.26 - 9.64
Kinematic viscosity at 56°-90°C [$m^2.s^{-1}$]	5.00×10^{-7} – 3.23×10^{-7}
Sound velocity 56°-90°C [$m.s^{-1}$]	1494.3 – 1509.8

The results of the water cavitation experiment can be seen in **Figs. 3.7** to **3.11**. The experiments were conducted for two different dissolved oxygen (DO) concentrations, i.e. higher and lower DO concentrations. The DO concentration in water was reduced by

heating the loop to 90°C for several hours. After that the loop was vacuumed to several hours also. This technique will remove some of the DO oxygen in water. However there was a saturated minimum DO concentration in which the level cannot be reduced further even with heating and vacuuming the loop for several times. As observed from the experiment, it was difficult to reduce the DO concentration below 3 mg/L. The results of the experiment in higher DO concentration can be seen from **Figs 3.7** and **3.8**. These figures show the onset condition of cavitation in water as a function of the noise intensity. For higher DO concentration in the water, the onset cavitation coefficient is around 2.7 at 56°C and around 2.9 at 74°C. It is also found that increasing the temperature in the water tends to increase the onset cavitation coefficient. This is because cavitation is actually a vaporization process that occurs if the static pressure falls below the vapor pressure of the liquid. In water, the vapor pressure is about 16.5 kPa at 56°C while it is about 36.9 kPa at 74°C. The increase of vapor pressure from 56°C to 74°C is more than twice. Therefore, an increase of temperature can have important effect on the growth of cavitation bubbles.

In case of lower DO concentrations, **Figs. 3.9** to **3.11** show the results of the onset coefficients of cavitation in water. The results show that DO concentration seems to have some effects on the onset of cavitation in water. The change of the onset cavitation coefficient is not so large, which is about 2.1 at 56°C and 2.3 at 74°C. However there is a trend that the onset condition decreases with the decrease of DO concentration. The decrease of DO concentration in water might cause this condition. In the experiment, heating and vacuuming the loop reduced DO concentration. Since it was difficult to differentiate between dissolved and floating micro bubbles of air that contained oxygen, therefore a reduction of DO by heating and vacuuming might also decrease the number of

nucleation sites (micro bubbles) as the growing sites of cavitation bubbles. And it is widely known that nucleation sites (micro bubbles) can have significant effect on the degree and onset cavitation coefficient. Higher concentration of dissolved/entrained air corresponds to more violent cavitation in water as observed by **Bistafa [3-12]**. Other consideration affected by the decrease of DO concentration is the total pressure inside the micro bubble. According to **Brennen [3-13]**, the inside pressure of the cavitation bubble is the mixture of partial pressure of liquid vapor pressure and gas. Since there is a decrease of DO concentration in the water (gas), therefore it is also expected that the total pressure will decrease. This decrease causes the micro bubble have smaller radius. Also the decrease of total pressure required for the growth of cavitation bubble will increase the dynamic pressure (faster velocity) in order to realize the formation of cavitation bubbles in the flow (lower static pressure) and decrease the onset cavitation condition (lower cavitation coefficient K).

From the results presented in **Figs. 3.2** to **3.11**, the comparison of onset condition between sodium at 300° and 400°C and water at 56°, 74° and 90°C can be analyzed because of the same kinematic viscosity. **Figure 3.11** shows the comparison of the onset condition in sodium and water. The comparison of onset cavitation condition expressed in the form of cavitation coefficient K between sodium and water is conducted when cavitation starts to occur in the flow (onset condition) as can be seen from the sharp increase of the acoustic noise intensity signal and hearing the rapid knocking sound on the venturi channel. For water at 56° and 74°C, the onset cavitation coefficient is almost the same which is about 2.1 and 2.3, respectively. While at 90°C the onset cavitation coefficient is about 1.8. The onset cavitation coefficients in the water case are relatively

higher than those in the sodium case which are about unity at 300° and 400°C. Even with lower DO concentration, the cavitation coefficient in water is still larger as compared to sodium. This difference might be caused by the difference of dissolved gas in water and sodium. In this case, water has higher dissolved gas concentration as compared to sodium. It is because air is easy to dissolve in water than argon in sodium, and based on the experiment this will increase the onset cavitation condition in water. Therefore in sodium, cavitation might occur mostly in the form of vaporous cavitation since the dissolved argon gas is very little while in water in the form of gaseous cavitation.

Comparing the results of sodium and water cavitation, it can be stated that the noise intensity has the same tendency or trend to increase as cavitation coefficient gradually decrease in both sodium and water. In case of sodium, the increase of the noise intensity is very steep as cavitation coefficient approaches unity. Therefore it is relatively easy to determine the onset condition. While in water, the increase of the noise intensity occurs gradually and less steep in higher DO concentration, at this condition the determination of the onset condition is relatively difficult. Except at lower DO concentration where the increase is relatively steep. The physical phenomena of this condition might be explained in this way. Since cavitation in sodium is dominated by vaporous cavitation due to very low dissolved gas concentration, therefore vaporization will not occur if the static pressure does not fall below the sodium saturated vapor pressure at a given temperature. As the static pressure falls below the saturated vapor pressure of sodium, vaporization or onset of cavitation starts to occur suddenly and a sudden increase of noise intensity is observed. This sudden increase of acoustic noise intensity at onset condition creates a steep acoustic noise gradient as observed in the

sodium cavitation experiment. These phenomena are different in case of water. In water due to very high dissolved gas concentration, the dissolved gas could precipitate from water at low static pressure creating micro bubbles. As the static pressure gradually decrease, the micro bubbles will also grow or expand gradually at low pressure creating gradual increase of acoustic noise intensity. Therefore the acoustic noise gradient is less steep as compared to sodium during the onset condition.

Analytical prediction of onset condition of cavitation was also conducted in the past by Kamiyama, *et al* **[3-15 to 3-17].** Comparing with their study in the past, they predict qualitatively that the gradient of the onset condition is not so steep due to gaseous cavitation in various liquids. The onset condition in sodium at high temperature was predicted analytically to have the same tendency with that in cold water in case of gaseous cavitation. Their assumption for the analytical prediction of onset condition lies in the dominant gaseous cavitation process rather than vaporous cavitation. In this study, it is shown that from sodium cavitation experiment the gradient is steep at onset condition due to vaporous cavitation. While in water is gradual and not so steep due to gaseous cavitation. Experimental results in sodium and water also show that onset condition has difference tendency between sodium and water that is caused by different dissolved gas concentration. Therefore onset condition in water is higher than in sodium. Also in sodium the most dominant cavitation process is vaporous cavitation due to very low dissolved gas concentration, while in water is gaseous cavitation due to very high dissolved gas concentration.

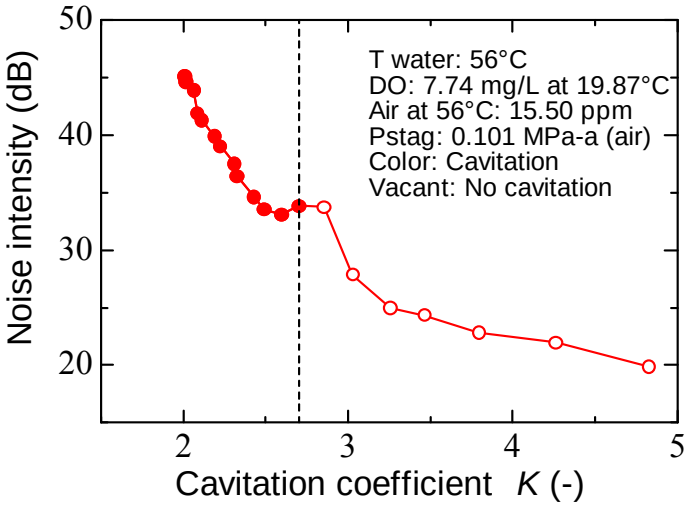

Fig. 3.7 Onset of cavitation in water at 56°C and higher dissolved oxygen content.

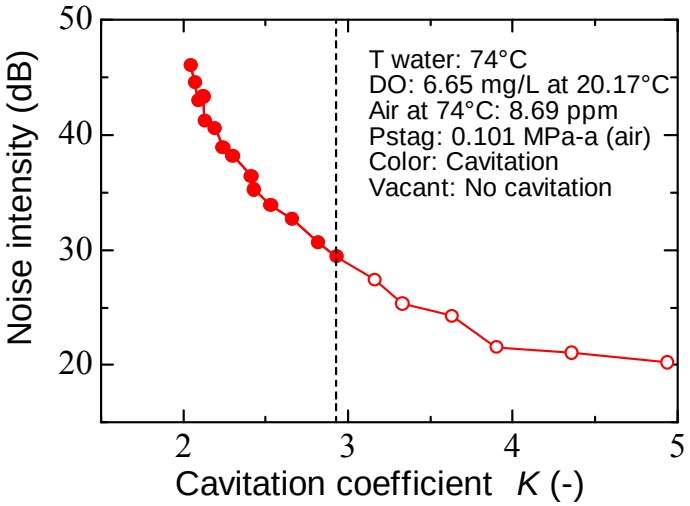

Fig. 3.8 Onset of cavitation in water at 74°C and higher dissolved oxygen content.

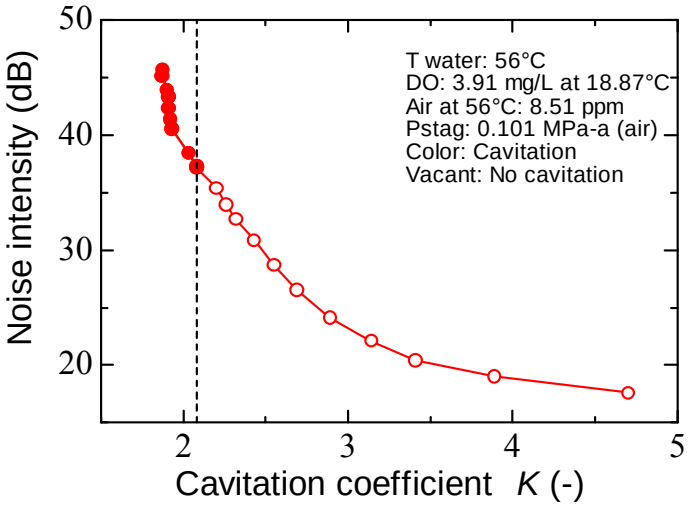

Fig. 3.9 Onset of cavitation in water at 56°C and lower dissolved oxygen content.

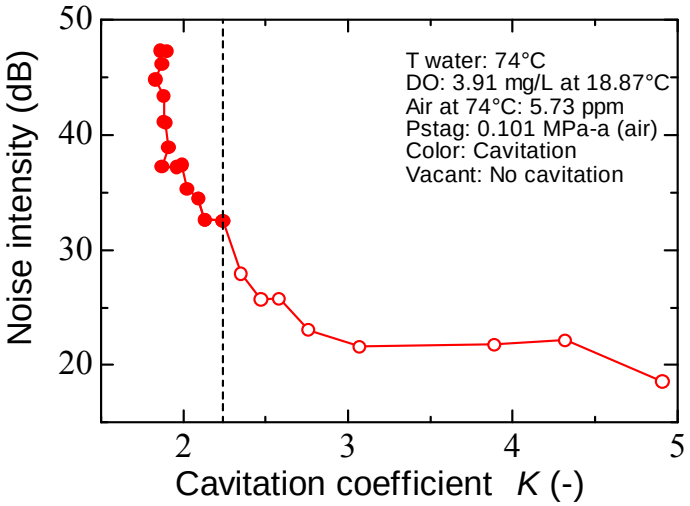

Fig. 3.10 Onset of cavitation in water at 74°C and lower dissolved oxygen content.

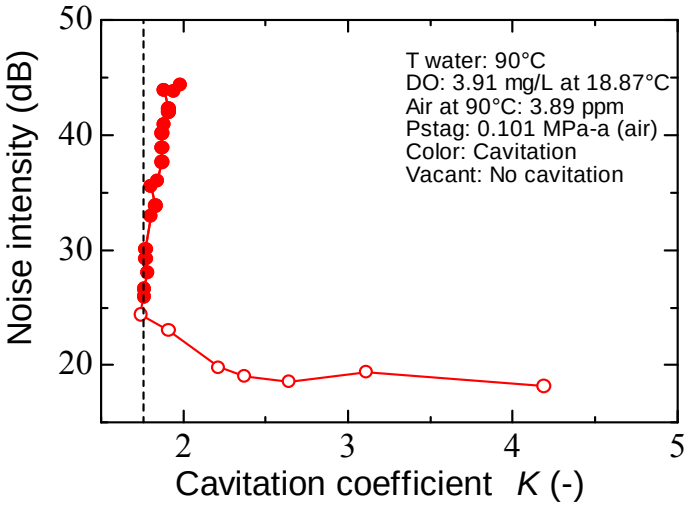

Fig. 3.11 Onset of cavitation in water at 90°C and lower dissolved oxygen content.

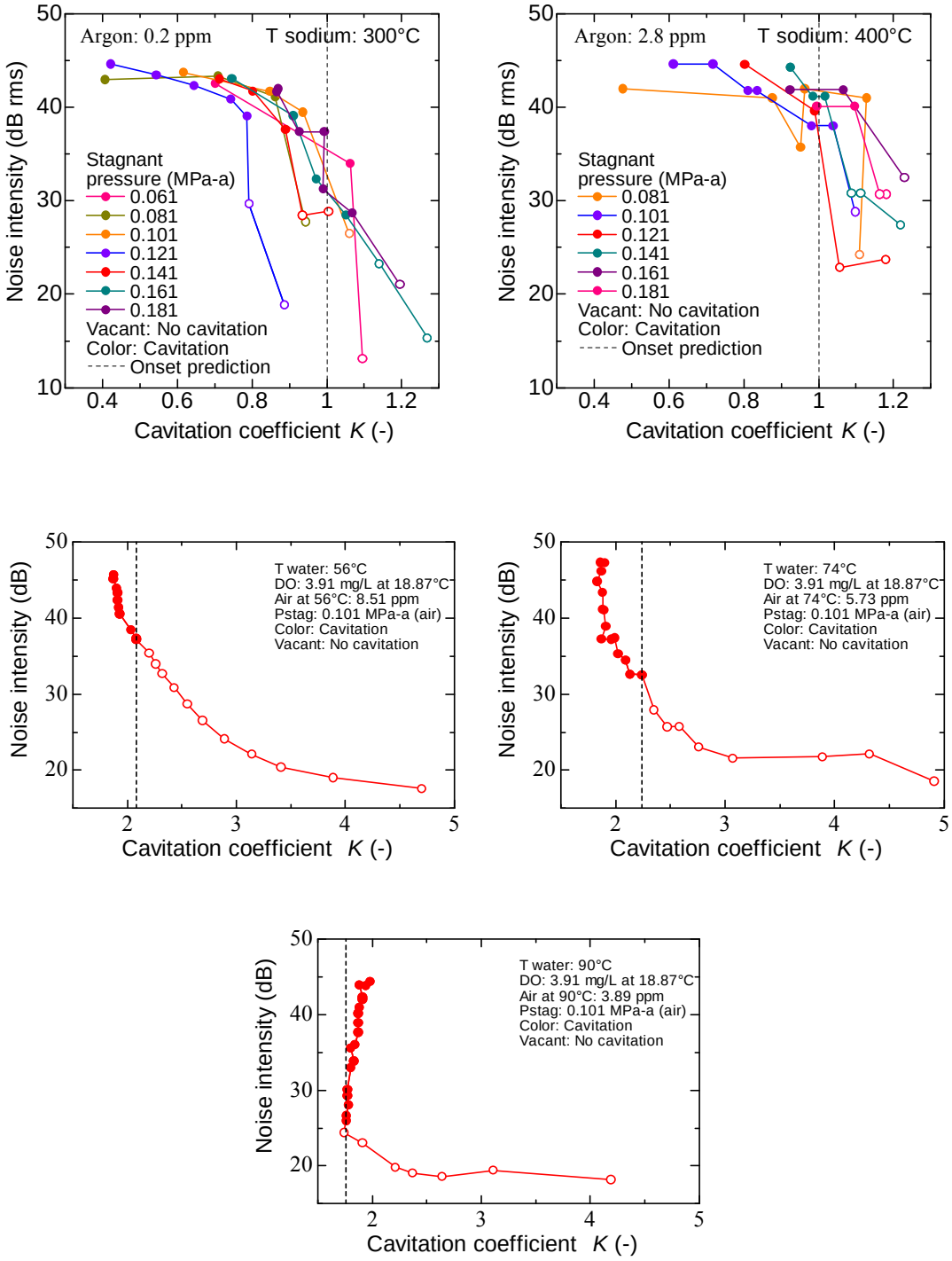

Fig. 3.12 Comparison of onset condition in sodium and water.

3.4.3 CFD Calculation of Cavitation for the Comparison of Sodium and Water Cavitation

In order to understand the detail of the cavitation process and the dynamics of cavitation bubbles for sodium and water cavitation, numerical calculation using CFD code is employed and the effect of gas on onset or inception of cavitation is also discussed in this chapter.

3.4.3.1 Mixture Model

The two-phase model used is based on the mixture model theory **[3-18]**. This model is a simplified multiphase model that can model phases, which move at different velocities. However this model assumes local equilibrium over short spatial length scale which means the coupling between two-phases should be strong. The mixture model can model n-phases (fluid or particulate) by solving the momentum, continuity, and energy equations for the mixture, the volume fraction equations for the secondary phases, and algebraic expressions for the relative velocities. Typical applications include sedimentation, cyclone separators, particle-laden flows with low loading, and bubbly flows where the gas volume fraction remains low. The mixture model uses a single-fluid approach just like VOF model. However it differs in two respects:

- The model allows the phases to be interpenetrating. The volume fractions α_q and α_p for a control volume can therefore be equal to any value between 0 and 1, depending on the space occupied by phase *q* and phase *p*.

- The model allows the phases to move at different velocities using the concept of slip velocities. If the phases are assumed to move at the same velocity, then the mixture model reduces to a homogenous multiphase model.

The mixture model solves the continuity equation, momentum equation, energy equation and the volume fraction equation for the secondary phases for the mixture.

The continuity equation for the mixture is stated as

$$\frac{\partial}{\partial t}(\rho_m) + \nabla.\left(\rho_m \vec{v}_m\right) = 0 \quad \text{.....(3-2)}$$

where $\vec{v}_m$ is the mass-averaged velocity:

$$\vec{v}_m = \frac{\sum_{k=1}^{n} \alpha_k \rho_k \vec{v}_k}{\rho_m} \quad \text{.....(3-3)}$$

and ρ_m is the mixture density:

$$\rho_m = \sum_{k=1}^{n} \alpha_k \rho_k \quad \text{.....(3-4)}$$

α_k is the volume fraction of phase *k*.

The momentum equation for the mixture is

$$\frac{\partial}{\partial t}\left(\rho_m \vec{v}_m\right) + \nabla.\left(\rho_m \vec{v}_m \vec{v}_m\right) = -\nabla p + \nabla.\left[\mu_m\left(\nabla \vec{v}_m + \vec{v}_m^T\right)\right] + \rho_m \vec{g} + \vec{F} + \nabla.\left(\sum_{k=1}^{n} \alpha_k \rho_k \vec{v}_{dr,k} \vec{v}_{dr,k}\right) \quad \text{.....(3-5)}$$

where *n* is the number of phases, $\vec{F}$ is a body force, and μ_m is the viscosity of the mixture:

$$\mu_m = \sum_{k=1}^{n} \alpha_k \mu_k \quad \text{(3-6)}$$

$\vec{v}_{dr,k}$ is the drift velocity for secondary phase *k*:

$$\vec{v}_{dr,k} = \vec{v}_k - \vec{v}_m \quad \text{(3-7)}$$

and the energy equation for the mixture is

$$\frac{\partial}{\partial t}\sum_{k=1}^{n}(\alpha_k \rho_k E_k) + \nabla.\sum_{k=1}^{n}\left(\alpha_k \vec{v}_k(\rho_k E_k + p)\right) = \nabla.(k_{eff}\nabla T) + S_E \quad \text{(3-8)}$$

where k_{eff} is the effective conductivity $\left(\sum \alpha_k (k_k + k_t)\right)$, where k_t is the turbulent thermal conductivity, defined according to the turbulence model being used. The first term on the righ-hand side of the energy equation represents energy transfer due to conduction. S_E includes any other volumetric heat sources. In energy equation,

$$E_k = h_k - \frac{p}{\rho_k} + \frac{v_k^2}{2} \quad \text{(3-9)}$$

For a compressible phase, and $E_k = h_k$ for an incompressible phase, where h_k is the sensible enthalpy for phase *k*.

3.4.3.2 Cavitation Model

The cavitation model used in the numerical calculation is the full cavitation model based on the work by **[3-14]**. This model is embedded in the CFD code FLUENT version 6.3.26 as the basic cavitation model **[3-18]**. The basic cavitation model in FLUENT has the following assumptions:

1) The system under investigation involves two phases (liquid and its vapor) and a certain fraction of modeled non-condensable gases.

2) Both bubble formation (evaporation) and collapse (condensation) are taken into account in the model.
3) The mass fraction of non-condensable gas is known in advance.

3.4.3.3 Vapor Mass Fraction and Transport

The governing equation for the transport of vapor mass fraction, f, is given by:

$$\frac{\partial}{\partial t}(\rho_m f) + \nabla\left(\rho_m \overrightarrow{v_v} f\right) = \nabla(\gamma \nabla f) + R_e - R_c \quad \text{.....(3-10)}$$

where R_e and R_c are derived from the Rayleigh-Plesset equations $\frac{p_B - p_\infty}{\rho} = R\frac{d^2R}{dt^2} + \frac{3}{2}\left(\frac{dR}{dt}\right)^2 + \frac{4\mu}{R}\frac{dR}{dt} + \frac{2S}{\rho R}$ and limiting bubble size considerations (interface surface area per unit volume) **[3-19]**.

when $p < p_{sat}$

$$R_e = C_e \frac{V_{ch}}{\sigma}\rho_l \rho_v \sqrt{\frac{2(p_{sat} - p)}{3\rho_l}}(1 - f) \quad \text{.....(3-11)}$$

when $p < p_{sat}$

$$R_c = C_c \frac{V_{ch}}{\sigma}\rho_l \rho_v \sqrt{\frac{2(p_{sat} - p)}{3\rho_l}} f \quad \text{.....(3-12)}$$

C_e and C_c are empirical constants with default value of 0.02 and 0.01, respectively and have been validated in sharp edge orifice and hydrofoil in water **[3-19]**. For sodium case in this study, the default empirical constants are validated with sodium cavitation experiment in venturi channel conducted at 200˚-400˚ and pressure range of 0.061-0.181 MPa-a for a total of 52 cases and show good agreement with experiments. Therefore, the

default value of C_e: 0.02 and C_c: 0.01 can be used for numerical calculation of sodium cavitation. V_{ch} is the characteristic velocity which is approximated by the local turbulence intensity, i.e. $V_{ch} = \sqrt{k}$.

3.4.3.4 Turbulence Induced Pressure Fluctuations

The effect of turbulence on cavitating flow is included in the FLUENT's cavitation model **[3-18]** and the equation for p_{sat} is therefore changed to the form

$$p_v = 0.5\left(p_{sat} + p_{turb}\right) \quad \text{(3-13)}$$

where

$$p_{turb} = 0.39\rho k \quad \text{(3-14)}$$

3.4.3.5 Effect of Gas β

The working fluid in the FLUENT's cavitation model is assumed to be a mixture of the liquid phase and the gaseous phase, with the gaseous phase comprising of the liquid vapor and the gas, such as air or argon gas **[3-18]**. With the effect of gas β**,** the density of the mixture ρ_m, is calculated as

$$\rho_m = \alpha_v \rho_v + \alpha_g \rho_g + \left(1 - \alpha_v - \alpha_g\right)\rho_l \quad \text{(3-15)}$$

The relationship between the mass fraction, f_i, and the volume fraction, α_i is

$$\alpha_i = f_i \frac{\rho}{\rho_i} \quad \text{(3-16)}$$

3.4.3.6 Phase Change Rates

The final form of the phase change rates [**Eqs. (3-11)** and **(3-12)**] after accounting for the effects of turbulence and gases are

when $p < p_v$

$$R_e = C_e \frac{\sqrt{k}}{\sigma} \rho_l \rho_v \sqrt{\frac{2(p_v - p)}{3\rho_l}} (1 - f_v - f_g) \quad \textbf{(3-17)}$$

when $p < p_v$

$$R_c = C_c \frac{\sqrt{k}}{\sigma} \rho_l \rho_v \sqrt{\frac{2(p_v - p)}{3\rho_l}} f_v \quad \textbf{(3-18)}$$

3.4.3.7 Standard $k-\varepsilon$ Model

The standard $k-\varepsilon$ model is a semi-empirical model based on model transport equations for the turbulence kinetic energy (k) and its dissipation rate (ε). The model transport equation for k is derived from the exact equation, while the model transport equation for ε was obtained using physical reasoning and bears little resemblance to its mathematically exact counterpart. In the derivation of the $k-\varepsilon$ model, the assumption is that the flow is fully turbulent, and the effects of molecular viscosity are negligible. The standard $k-\varepsilon$ model is therefore valid only for fully turbulent flows **[3-18]**.

The turbulence kinetic energy, k, and its rate of dissipation, ε, are obtained from the following transport equations:

$$\frac{\partial}{\partial t}(\rho k) + \frac{\partial}{\partial x_i}(\rho k u_i) = \frac{\partial}{\partial x_j}\left[\left(\mu + \frac{\mu_t}{\sigma_k}\right)\frac{\partial k}{\partial x_j}\right] + G_k + G_b - \rho\varepsilon - Y_M + S_k \quad \textbf{(3-19)}$$

and

$$\frac{\partial}{\partial t}(\rho\varepsilon)+\frac{\partial}{\partial x_i}(\rho\varepsilon u_i)=\frac{\partial}{\partial x_j}\left[\left(\mu+\frac{\mu_t}{\sigma_\varepsilon}\right)\frac{\partial\varepsilon}{\partial x_j}\right]+C_{1\varepsilon}\frac{\varepsilon}{k}(G_k+C_{3\varepsilon}G_b)-C_{2\varepsilon}\rho\frac{\varepsilon^2}{k}+S_\varepsilon \text{ …...} \textbf{(3-20)}$$

In these equations, G_k represents the generation of turbulence kinetic energy due to the mean velocity gradients. G_b is the generation of turbulence kinetic energy due to buoyancy. Y_M represents the contribution of the fluctuating dilatation in compressible turbulence to the overall dissipation rate. $C_{1\varepsilon}$, $C_{2\varepsilon}$, and $C_{3\varepsilon}$ are constants. σ_k and σ_ε are the turbulent Prandtl numbers for k and ε, respectively. S_k and S_ε are user-defined source terms. The turbulent or eddy viscosity, μ_t, is computed by combining k and ε as follows:

$$\mu_t=\rho C_\mu\frac{k^2}{\varepsilon} \text{ ……...……} \textbf{(3-21)}$$

Where C_μ is a constant. The model constants $C_{1\varepsilon}$, $C_{2\varepsilon}$, C_μ, σ_k, and σ_ε have the following default values

$C_{1\varepsilon}=1.44, C_{2\varepsilon}=1.92, C_\mu=0.09, \sigma_k=1.0, \sigma_\varepsilon=1.3$

These default values have been determined from experiments with air and water for fundamental turbulent shear flows including homogenous shear flows and decaying isotropic grid turbulence. They have been found to work fairly well for a wide range of wall-bounded and free shear flows **[3-18]**.

3.4.3.8 Test Section Geometry

The simulated test section for numerical calculation is based on the cavitation experiments conducted by the authors in water and liquid sodium. The geometry of the venturi part of the test section for both sodium and water cavitation experiment is similar and can be seen in **Fig. 3.13**. The inner diameter (D1) and outer diameter (D0) is 6.5 mm and 21 mm, respectively.

Figure 3.14 shows the grid for the numerical solution. It consists of 11440 quadrilateral cells, axisymmetric. The results of the grid sensitivity dependency on the numerical solution are shown in **Fig. 3.15**. It shows that the numerical result of 11440 cells have no significant difference with a test section comprising of 45760 cells. Therefore 11440 quadrilateral cells were used for the calculation.

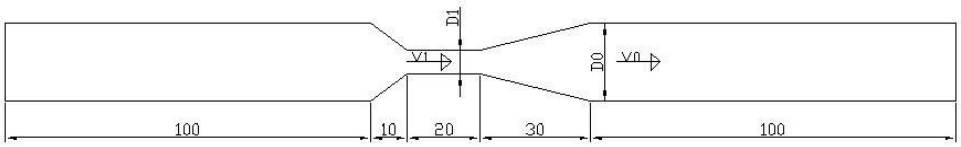

Fig. 3.13 Venturi test section for cavitation experiment (length is in mm).

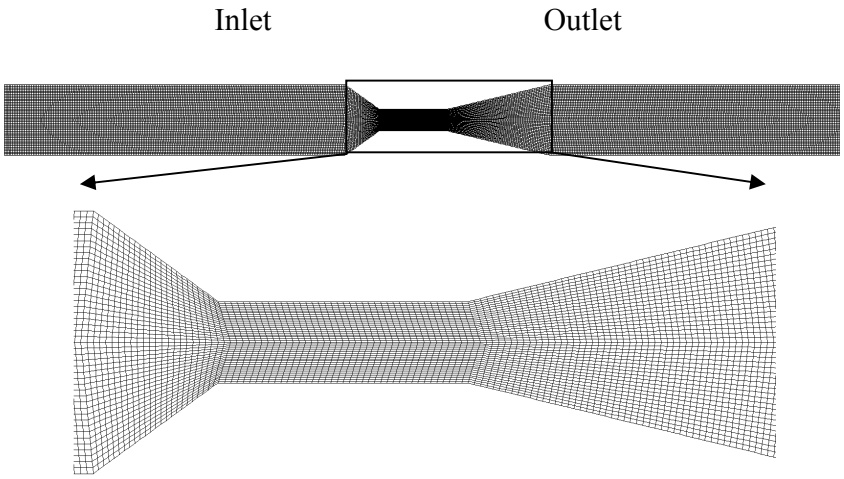

Fig. 3.14 Grid for numerical solution.

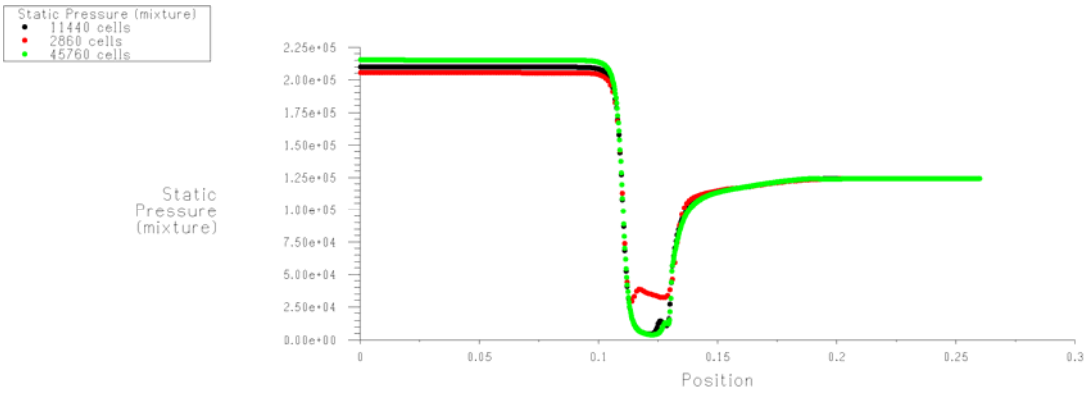

Fig. 3.15 Grid sensitivity check at central axis.

3.4.3.9 Results of CFD Calculation

Cavitation occurrences in numerical calculation are judged from the large increase of void fraction distribution at the central axis. The change of the void fraction at the wall will follow the change at the central axis. **Figure 3.16** shows an example of the result of void fraction distributions for water. The inlet and outlet of the venturi is at 110 mm and

130 mm, respectively. The figure indicates a sharp increase of the void fraction for cavitation coefficient *K* equals to 1.08 and 0.98. At these values, cavitation starts to occur because there is a sudden change of the void fraction distribution at the venturi part. This increase is caused by the formation of cavity bubbles at the venturi due to a large decrease of static pressure below the vapor pressure of the liquid due to evaporation as shown in **Fig. 3.16** by assuming that the air gas content is 15 ppm which is a typical value for tap water.

To check the validation of the cavitation model in sodium, cavitation calculation in sodium was conducted for different temperature and stagnant pressure range condition based on experiment data in sodium cavitation from 200°-400°C and 0.061-0.181 MPa (52 cases). The onset condition results are compared with the experiment and the results show reasonably good agreement as shown in **Figs. 3-17 to 3-19**.

The boundary conditions for the numerical simulation in this study are fixed inlet velocity and fixed outlet pressure. The values are based on experimental measurements conducted in sodium and water at different temperatures and pressures conditions. The relative velocity between gas and liquid is assumed to be zero (no slip). For the present experiment, the solubility of argon gas in liquid sodium was not measured since it was difficult to measure it using the present experimental apparatus. Therefore in sodium the dissolved argon gas concentration was calculated and assumed to be in equilibrium with the sodium temperature. The properties of sodium at 200°-400°C (saturated vapor pressure, density, surface tension and viscosity) for numerical calculation are shown in **Table 3.3** above. While for water, the properties of water at 10.8°-13°C are shown in **Table 3.5** below.

Table 3.5 Properties of water for numerical calculation.

Vapor pressure at 10.8°-13°C [kPa]	1.288 – 1.490
Liquid density at 10.8°-13°C [kg/m^3]	999.65 – 999.41
Surface tension at 10.8°-13°C [N.m^{-1}]	7.4 x 10^{-2} – 7.3 x 10^{-2}
Viscosity at 10.8°-13°C [Pa.s]	1.28 x 10^{-3} – 1.20 x 10^{-3}

Numerical calculation results of onset cavitation conditions in water and liquid sodium compared with the experiments for different value of gases β concentration are shown in **Figs. 3.20** and **3.21**. In water, the gas is assumed to be air; while in liquid sodium is assumed to be argon gas. For both cases, the change of the gas has significant effects on the onset conditions of cavitation. The onset conditions of cavitation increase with the increase of gases concentration because their existences in the fluid could enhance the growth process of cavity bubbles. These phenomena are caused by the increasing number of micro nucleation sites that will grow into cavitation bubbles when the liquid pressure is low. Reference **[3-12]** in his experiment stated that the gas content is very influential in the inception mechanism of cavitation. He showed that gaseous cavitation due to diffusion of air into the nuclei is easy to occur for flow with higher air concentration than with lower air concentration. The number of bubbles also increases for flow with higher air concentration than for lower one.

From the figures, for water with air gas content of 40 ppm, the results are close to the experimental data. While in sodium, the content of argon gas that gives the results close with the experimental data is 1 ppm. The difference of gas content might be caused by the different solubility of air and argon gas in water and liquid sodium. In water, air is

easily dissolved while in liquid sodium argon gas is not easily dissolved. For instance in equilibrium condition, the solubility of argon gas in liquid sodium at 400°C calculated by Veleckis' correlation **[3-19]** and the solubility of air in water at 10.8°C-13°C calculated based on the averaged value of dissolved oxygen measurement at average water temperature of 10.96°C are 2.83 ppm and 27.03 ppm, respectively. In water, the value of air gas content in the numerical calculation that gives the result close to the experimental data is much higher than the calculated value at equilibrium condition as calculated by using Henry's law **[3-20]**. While in sodium, the value of argon gas in the numerical calculation that gives the result close to the experimental data is lower than the calculated value at equilibrium condition. These differences are caused by the different onset cavitation condition judgment between experiments and numerical calculations. In water experiment the judgment of onset cavitation was conducted by visual observation, therefore cavitation can be seen and occurred earlier than numerical prediction. While in sodium, the judgment was based from acoustical noise, therefore cavitation occurred later because of the influence of background noise than predicted from numerical calculation.

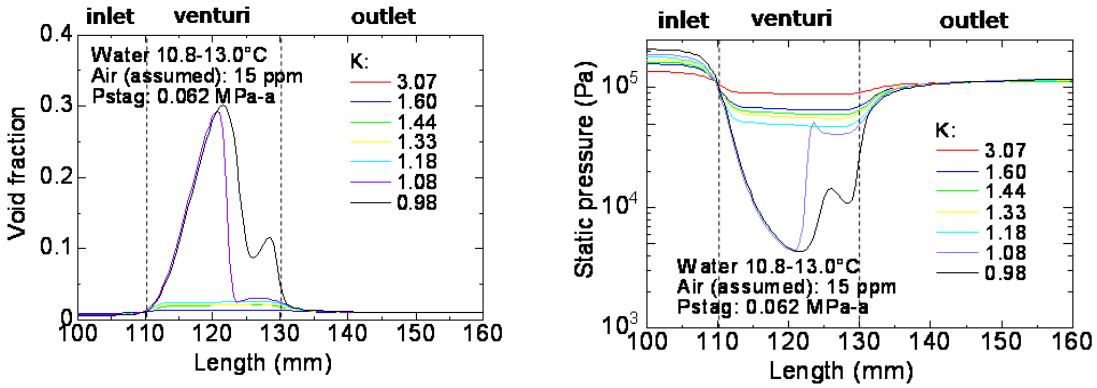

Fig. 3.16 Calculation results of void fraction (left figure) and static pressure (right figure) at central axis of the test section.

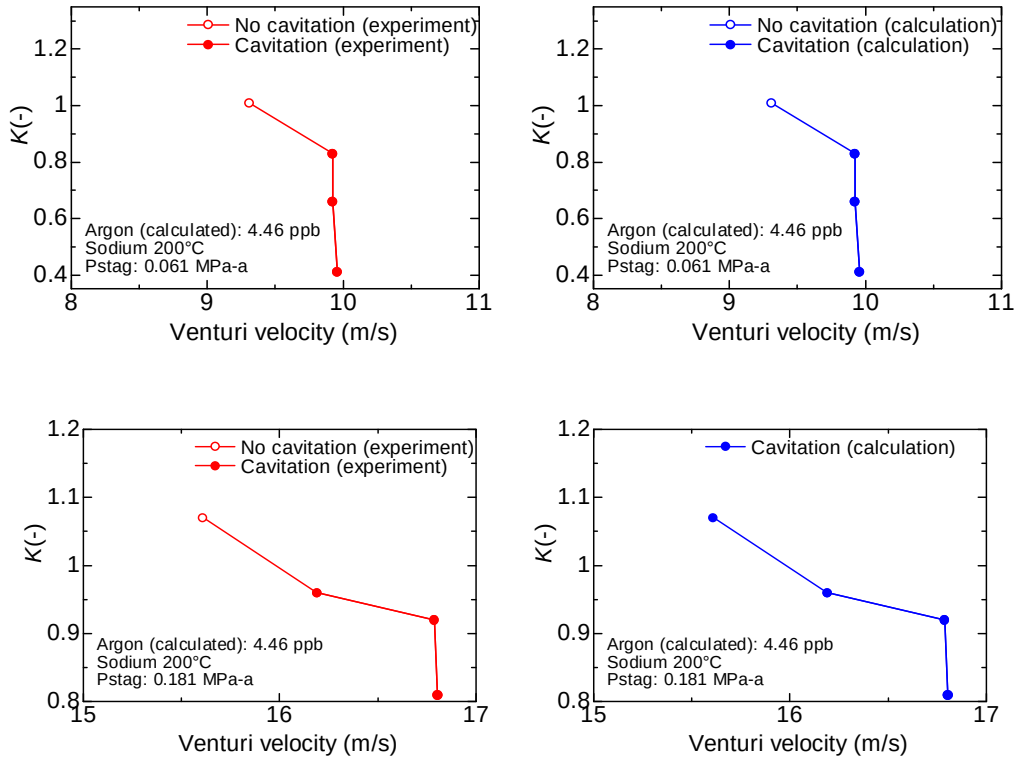

Fig. 3.17 Comparison of onset cavitation condition in sodium between experiment (left figures) and numerical calculation (right figures) at 200°C.

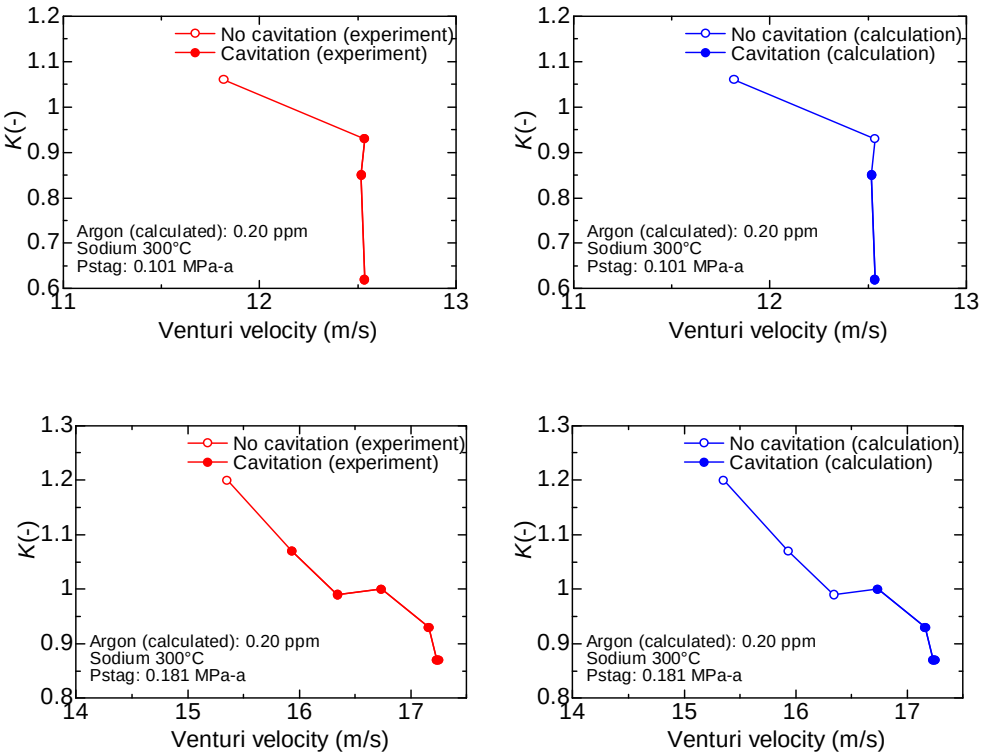

Fig. 3.18 Comparison of onset cavitation condition in sodium between experiment (left figures) and numerical calculation (right figures) at 300°C.

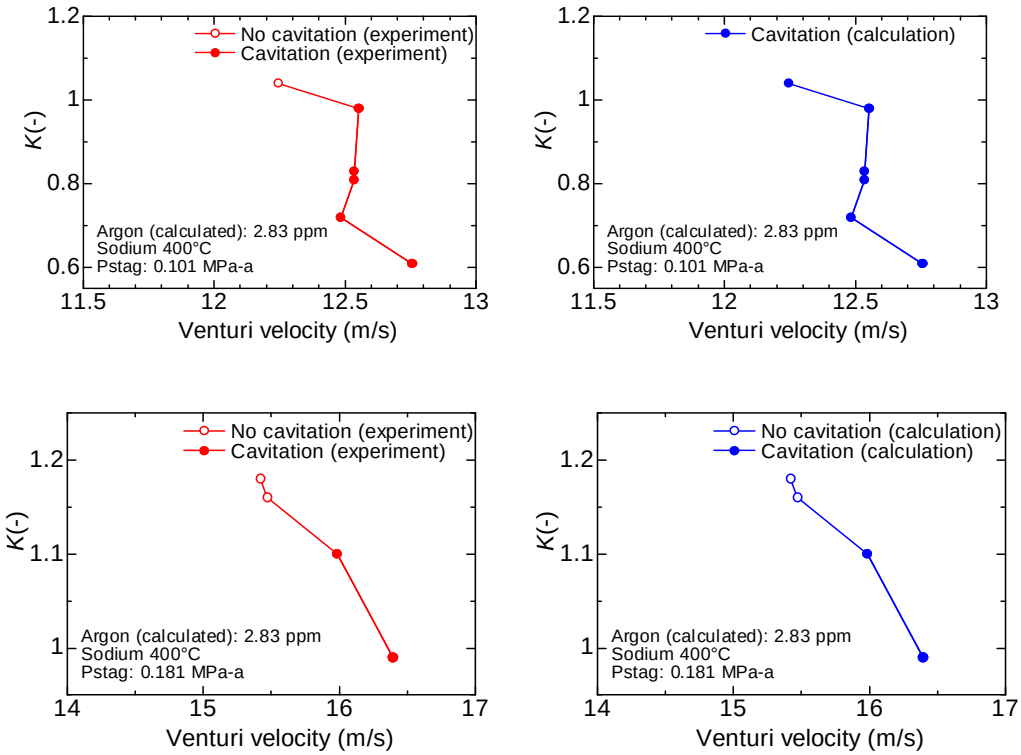

Fig. 3.19 Comparison of onset cavitation condition in sodium between experiment (left figures) and numerical calculation (right figures) at 300°C.

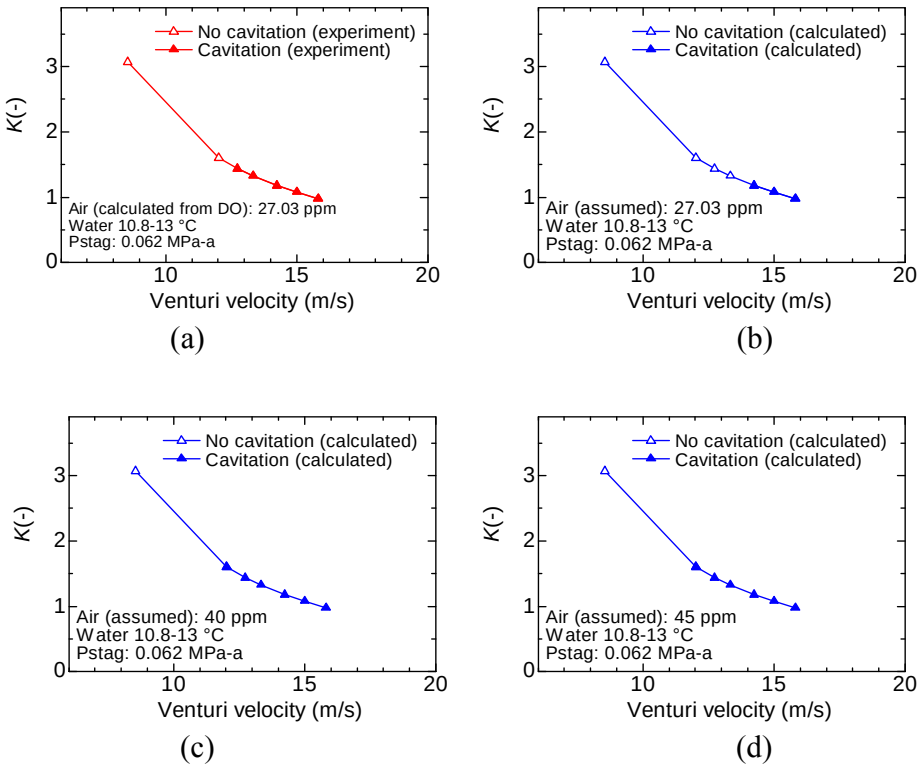

Fig. 3.20 Comparison of onset cavitation condition in water (flow rate: 17.02-31.47 l/min; K: 3.07-0.98; P_{ds}: 0.114-0.124 MPa-a).

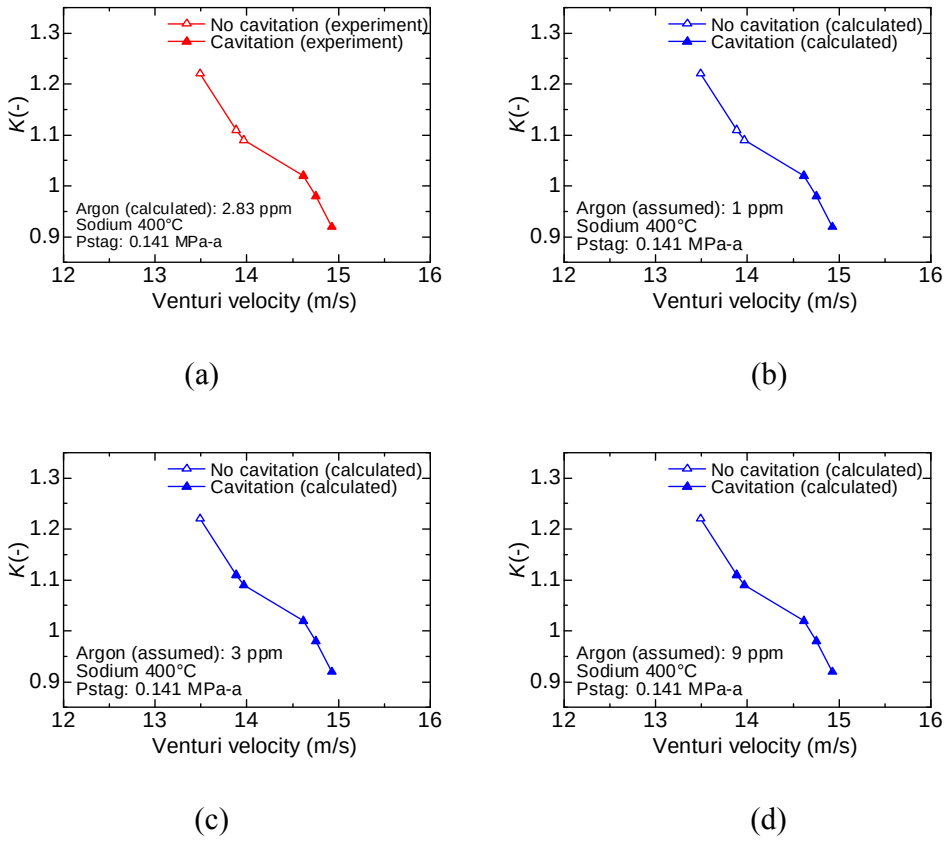

Fig. 3.21 Comparison of onset cavitation condition in sodium (flow rate: 26.86-29.72 l/min; K: 1.22-0.93; P_{ds}: 0.094-0.087 MPa-a.

Figures 3.22 and **3.23** show the contours of void fractions for water and liquid sodium with different gas contents (air or argon gas). The contours show the formations of voids (cavity bubbles) at the throat of the venturi inlet. The high void fractions (cavity bubbles) are caused by the high turbulent intensity and large pressure drop when the liquid (water and sodium) flowing through the throat of the venturi region, especially at the inlet throat of the venturi channel. This will cause evaporation and the bubbles grow into large cavitation bubbles. Because of the increase of the gas content (air or argon), the voids filling up the venturi part of the test section shown in **Fig. 3.22** (lower figure) and

Fig. 3.23 (lower figure) and might choke the flow. In the experiment, choking conditions are observed in case of sodium cavitation. These choking conditions might be caused by the decrease of sound velocity in the liquid due to the increasing amount of cavitation bubbles (vapors). These figures also show that the voids (cavity bubbles) are carried away downstream by the flow and collapse (condense) due to the high pressure downstream of the test section that creates condensation.

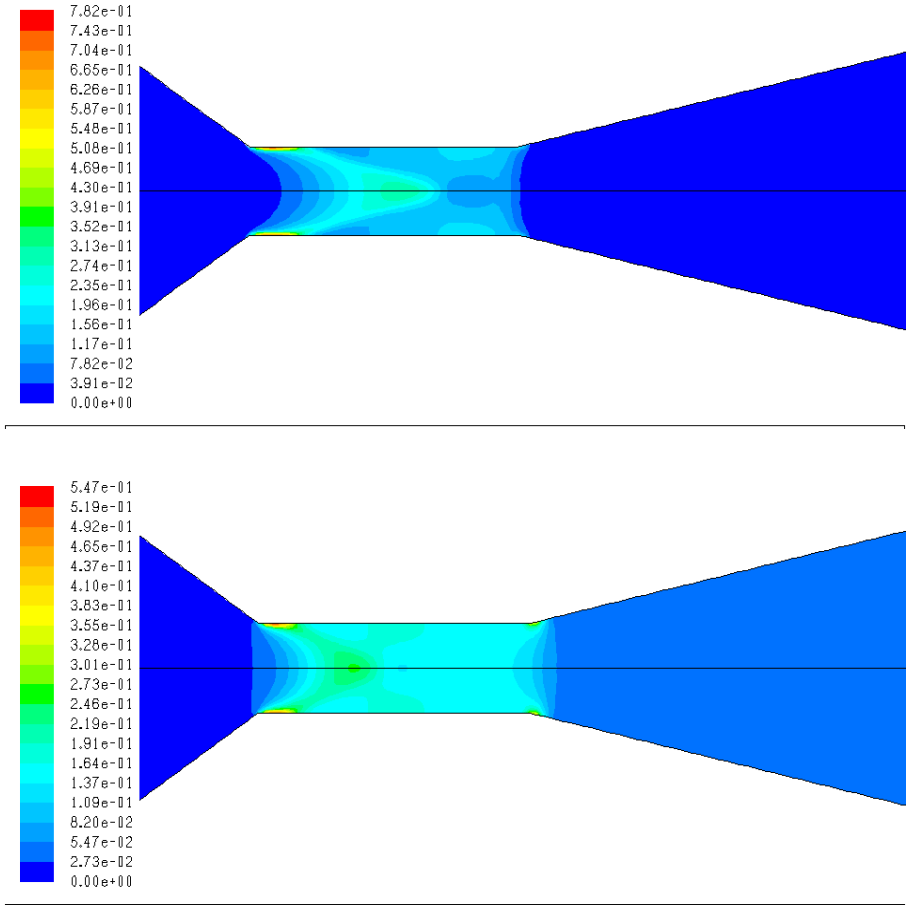

Fig. 3.22 Contours of void fraction (0: liquid, 1: vapor) in water for *K*: 0.98 and T: 10.8-13.0°C, β (air): 15 ppm (upper figure), and β (air): 45 ppm (lower figure).

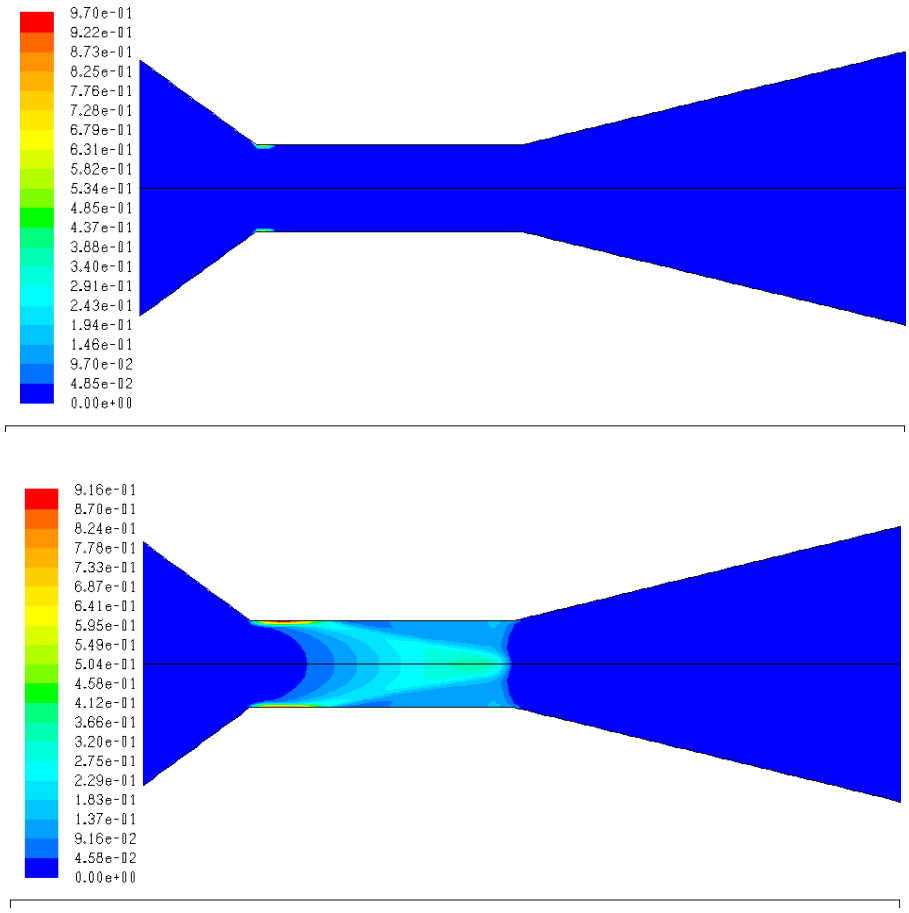

Fig. 3.23 Contours of void fraction (0: liquid, 1: vapor) in liquid sodium for *K*: 0.92 and T: 400°C, β (argon): 1 ppm (upper figure), and β (argon): 3 ppm (lower figure).

Numerical simulation of cavitation in sodium for different conditions i.e. no cavitation, intermittent, and developed cavitation is shown in **Fig. 3.24**. The calculation conditions and boundary conditions are based on the experimental measurement conducted at stagnant pressure in the expansion tank of 0.181 MPa-a and sodium temperature of 200°C. The relative velocity between gas and liquid is assumed to be zero (no slip condition). The gas (argon) content β in sodium is assumed to be 1 ppb in order to have the computed result in close agreement with the experiments, since in the

experiments the argon gas content in liquid sodium was not measured. **Figure 3.24** shows the contours of calculated void fractions for no cavitation at *K*: 1.07, intermittent cavitation at *K*: 0.95 and developed cavitation at *K*: 0.91 at 200°C.

The calculated result shows that cavitation bubbles are produced at the throat of the venturi as shown in **Fig. 3.24 (a)**. These bubbles are produced by the high velocity that decreases the static pressure below the static pressure of liquid sodium at 200°C. However, the bubbles are very small and can condense quickly before growing to large bubbles and collapse downstream. For this condition, sodium flow rate is not high enough to detach the bubbles from the wall. Therefore, there is no cavitation bubbles observed in the downstream of the venturi.

Meanwhile in intermittent and developed cavitation conditions shown in **Fig. 3.24 (b)** and **3.24 (c)**, respectively, pressure drop at the throat of the venturi becomes larger due to an increase of liquid sodium flow rate. This initiates bubbles to grow even larger. The cavitaton bubbles are easily detached from the wall because of higher flow rate, and conveyed downstream. At downstream, these bubbles collapse due to condensation caused by an increase in static pressure of liquid sodium.

Moreover, more bubbles are produced in developed cavitation in **Fig. 3.24 (c)** compared to in intermittent cavitation in **Fig. 3.24 (b)** because of larger pressure drop. These bubbles occupy most of the test section. Since more bubbles are produced with an increase in the flow rate, it is possible that choking conditions will occur at some certain void fractions, in which the speed of liquid sodium is close to or equal to the sonic speed in two-phase liquid sodium. At this condition, the number of bubbles produced is relatively constant; therefore the magnitude of the noise intensity is also relatively

constant. Furthermore, more erosion should be expected at developed cavitation because of more cavitation bubbles collapse.

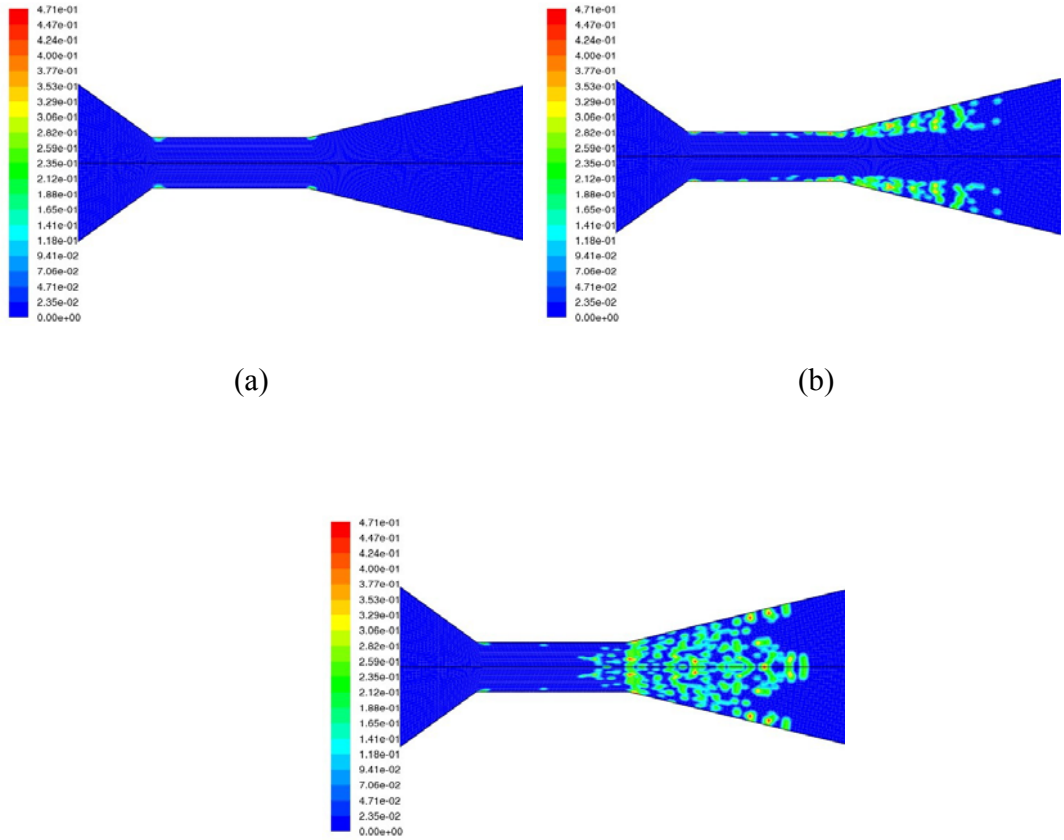

Fig. 3.24 Contours of void fraction (0: liquid, 1: vapor) in liquid sodium at 200°C and β (argon): 1 ppb, for (a) K: 1.07; (b) K: 0.95; and (c) K: 0.91.

3.4.4 High Speed Photography of Cavitation Bubbles in Water

In order to support the CFD calculation results of the cavitation process and how the bubble dynamics progress during the onset and developed cavitation conditions, cavitation in water at room temperature using venturi test section made from acrylic resin [97]

was conducted. This experiment was conducted using the low pressure water loop apparatus. The pressure at the loop was reduced to 0.062 MPa-a so that cavitation can easily occur in the venturi channel. The dynamics of the cavitation bubbles during the onset and developed cavitation conditions are recorded by using high speed camera with stroboscope lights. The stroboscope lights frequency is 500 Hz with flashing duration of 2.4 μs and flashing energy of 5 W. The high speed camera was operated at 500 fps (frame per second) and digital shutter speed of 1/500 second. This will give an image with the size of 512 x 240 pixels and recording time of 2.1 seconds.

The results of the cavitation conditions from onset to develop are shown in **Figures 3.25** and **3.26**. At intermittent condition where the cavitation bubbles occur intermittently as shown in **Fig. 3.25**, the high speed camera pictures show that cavitation bubbles at the beginning occurred at the throat of the venturi channel inlet (at time 0/500 s). This small bubbles start to elongate into long cavitation bubbles attached on the surface of the venturi channel following the flow of the water inside the channel (at time 2/500-6/500 s). The shape of the elongated bubbles are relatively straight. At the end of the venturi outlet, the bubbles start to separate from the wall (at time 7/500-8/500 s). At develop cavitation condition shown in **Fig. 3.26**, the elongated cavitation bubbles that attached on the surface of the venturi channel start to grow at the throat of the venturi channel outlet (at time 0/500 s). The growing bubbles will separate from the wall and collapse downstream (at time 1/500-2/500 s). The collapse of the cavitation bubbles downstream will alter or disturb the flow at the venturi channel shown at time 3/500-7/500, where the shape of the elongated bubbles that attached on the surface are disturbed and not relatively straight. Especially close to the throat of the venturi channel outlet.

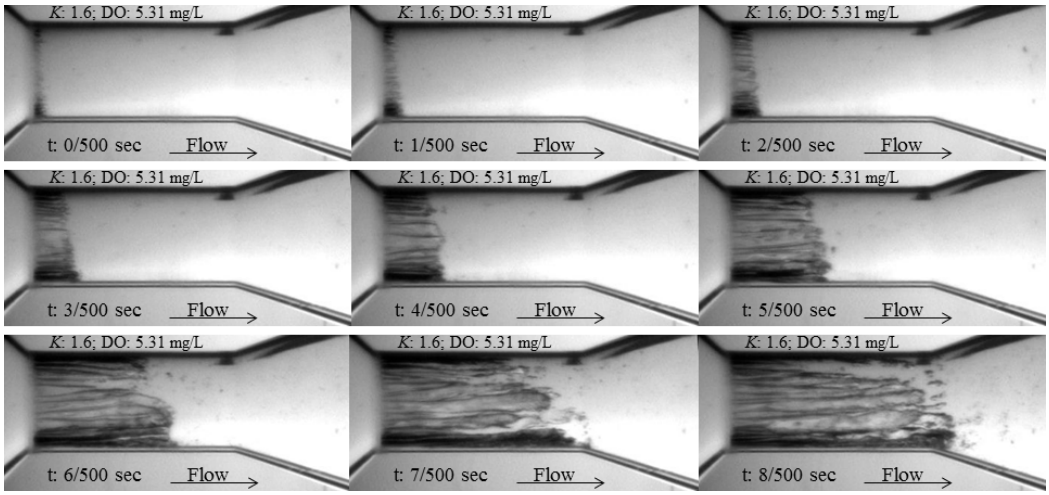

Fig. 3.25 High speed camera of water cavitation at intermittent condition. Water temperature is 21.2°-22.4°C (room temperature).

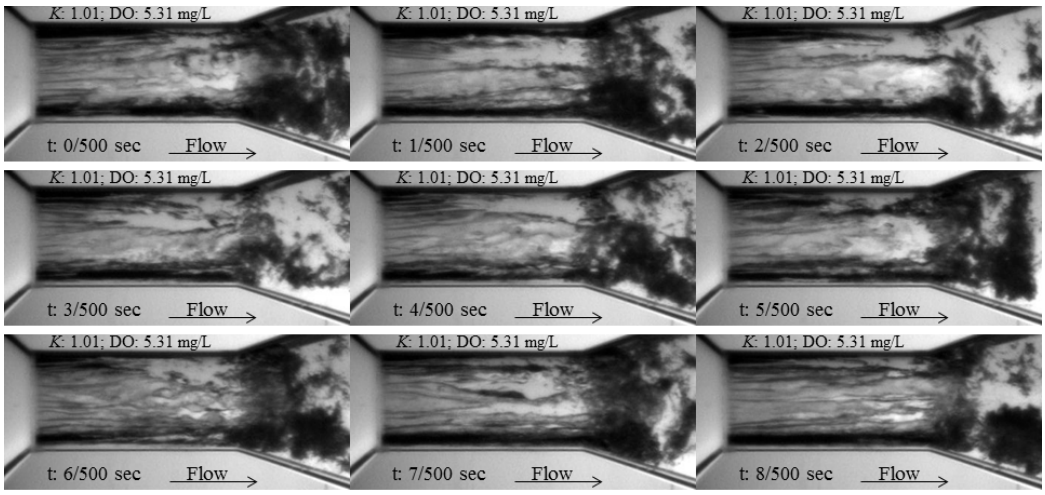

Fig. 3.26 High speed camera of water cavitation at develop condition. Water temperature is 21.2°-22.4°C (room temperature).

3.5 Conclusion

From the experimental results of sodium and water cavitation it can be concluded that:

1) The onset condition of sodium cavitation was around unity (a little bit higher than 1). This value was lower than onset condition of water cavitation that had a value higher than unity. This condition might be caused by the lower concentration of dissolved gas (argon) in sodium as compared to air in water.
2) The increase of the stagnant pressure at the expansion tank in sodium cavitation will increase the onset velocity for the realization of cavitation in venturi test section. The high stagnant pressure could suppressed the formation of cavitation bubbles during the onset condition, therefore the onset cavitation velocity in the venturi increased in order to decrease the local static pressure below the sodium vapor pressure (cavitation bubbles formation).
3) The onset condition of sodium cavitation can be predicted easily on the map of noise intensity change with the change of cavitation coefficient since the gradient of the noise intensity with the change of cavitation coefficient was steep (the increase of noise intensity from no cavitation to onset of cavitation condition was steep). In the water cavitation case, the determination of the onset condition was rather difficult at lower temperature since the change of the noise intensity was gradual with the change of cavitation coefficient from no cavitation to onset of cavitation condition. However at higher temperature the change of the noise intensity became steep again. The differences of the onset condition and change in the noise intensity with the change of cavitation coefficient between sodium and water might be caused by the difference

mechanism of cavitation. The dominant cavitation process during the onset of cavitation in case of sodium was vaporous cavitation while in water it was in the form of gaseous cavitation. These different mechanisms caused the onset cavitation condition in sodium were lower than in water and the change of noise intensity was steep when cavitation occurred at the venturi.

4) From the numerical simulation of cavitation for water and liquid sodium, it can be concluded that the onset conditions of cavitation were influenced by the amount of non-condensable gases in the liquid, i.e. argon and air. Comparing with the experimental results, the gas contents that gave close predictions on onset cavitation conditions with the experiments were larger in water than in liquid sodium because of the different solubility of air and argon gas.
5) The high-speed camera used to observe the cavitation process in water showed that cavitation bubbles first produced at the venturi throat and increased with the increased of the flow. These voids were then conveyed and collapsed at downstream because of an increase in the static pressure.

3.6 References

3-1 Sato, K. and Kakutani, K., (1994), Measurement of Cavitation Inception, JSME International Journal Series B, Vol. 37, No. 2, pp. 306-312.

3-2 Courbiere, P., (1984), An acoustic Method for Characterizing The Onset of Cavitation in Nozzles and Pumps, International Symposium on Cavitation Inception, pp. 137-143.

3-3 Lin, H. J. and Katz, J., (1987), The Effect of Background Noise on Cavitation Phenomena in Water Jets, Cavitation and Multiphase Flow Forum, FED-Vol. 50, June 14-17, pp. 41-44.

3-4 Hammitt, F. G., (1971), Effects of Gas Content Upon Cavitation Inception, Performance, and Damage, UMICH 01357-19-T.

3-5 Hammitt, F. G., (1971), Effects of Gas Content Upon Cavitation Inception, Performance, and Damage (Summary Report for Working Group No. 1 of Section for Hydraulic Machinery, Equipment and Cavitation of IAHR), UMICH 01357-21-T.

3-6 Hammitt, F. G., Robinson, M. J., Kersppainen, D. J. and Robinson, R. A., (1965), Gas Entrainment Effects on Cavitation Number in Mercury in ½ inch Venturi to 400°F, Internal report 06110-7-I.

3-7 Hammitt, F. G., Robinson, M. J., Koopman, R. P. and Ericson, D. M., (1966), Gas Content Effects on Cavitation Number in Water in A Cavitating Venturi, TR-19.

3-8 Hammitt and Ericson, D. M., (1969), Scale Effects Including Gas Content Upon Cavitation in A Flowing System, TR-01357-11-T.

3-9 Ericson, D. M., (1969), Observations and Analyses of Cavitating Flow in Venturi Systems, Ph.D dissertation, University of Michigan.

3-10 Coubiere, P., (1984), An Acoustic Method for Characterizing The Onset of Cavitation in Nozzles and Pumps, International Symposium on Cavitation Inception, pp. 137-145.

3-11 Veleckis, E., Dhar, S. K., Cafasso, F. A. and Feder, H. M., (1971), Solubility of Helium and Argon in Liquid Sodium, The Journal of Physical Chemistry, Vol. 75, No. 18, pp. 2832-2838.

3-12 Bistafa, S. R., (1986), Noise Generated by Cavitation in Orifice-Plates with Some Gaseous Effects, International Symposium on Cavitation and Multiphase Flow Noise, pp. 41-52.

3-13 Brennen, C. E., (1995), Cavitation and Bubble Dynamics, Oxford University Press, New York.

3-14 Singhal, A. K., Athavale, M. M., Li, H. and Jiang, Y., (2002), Mathematical Basis and Validation of the Full Cavitation Model, Journal of Fluids Engineering, 124, pp. 617-624.

3-15 Kamiyama, S. and Yamasaki, T., (1986), Critical Condition of Cavitation Occurrence in Various Liquids, Journal of Fluids Engineering, Vol. 108, pp. 428-432.

3-16 Kamiyama, S. and Yamasaki, T., (1980), One Predicting Method of Gaseous Cavitation Occurrence in Water and Sodium, Bulletin of the JSME, Vol. 23, No. 183, pp. 1428-1434.

3-17 Kamiyama, S. and Yamasaki, T., (1982), One Prediction Method of Cavitation Occurrence in Special Liquids (in Japanese), Bulletin of the JSME, Vol. 48, No. 125, pp. 43-49.

3-18 FLUENT 6.3 User's Guide, (2006), Fluent Inc.

3-19 Fink, J. K., and Leibowitz, L., (1995), Thermodynamic and Transport Properties of Sodium Liquid and Vapor. Argonne National Laboratory, USA.

3-20 Sander, R., (1999), Compilation of Henry's Law Constants for Inorganic and Organic Species of Potential Importance in Environmental Chemistry, Max-Planck Institute of Chemistry, Germany.

CHAPTER 4

CHARACTERISTICS OF NOISE SPECTRUM IN SODIUM AND WATER CAVITATION

4.1 Introduction

The early detection of cavitation in SFR is very important part in order to ensure the safety of the flow components. This could prevent further damages caused by cavitation such as erosion on the material surface. In regard with the occurrence of cavitation in the fluid system besides its potential to create erosion, it is generally accepted especially in the water system case that the onset of cavitation is associated with its acoustic noise as one of the characteristics of cavitation since the noise is produced by the formation and collapse of cavitation bubbles. Therefore, the noise emitted from cavitation bubbles can be used as a tool to detect the occurrence of cavitation in the sodium similar to that used in water. The differentiation of cavitation noise from the background noise can be used to judge whether cavitation already occurred or not in the flow system. Bistafa in 1986 **[4-1]** measured the noise generated by cavitation in orifice plates immersed in water and found an increase of about 20 dB between the background and cavitation. Sato in 1987 **[4-2]** studied the cavitation process by means of acoustic pulse measurement has been conducted by using long orifice in water. He stated that cavitation stages could be divided according to the acoustic pulse count rate. Frizell, *et al* in 1987 **[4-3]** found that noise frequency from a bubble generated by a nozzle in water is associated with the volume pulsation of the bubble. The sound produced is in the form of a damped sinusoidal oscillation. Research on the noise produced by bubbles splitting in a turbulent free shear flow in water showed that splitting can be a substantial noise producer with sound level above single phase jet noise **[4-4]**. The study of the cavitation noise and its correlation with the cavitation coefficient has been conducted by Zhuang, *et al* in 1988 **[4-5]** on three different headforms in water. They found that for higher

cavitation coefficient the sound spectra were dominated by the background noise over low frequency. In cavitation inception, the noise levels do not increase very much in the low frequency range but increase drastically in the high frequency range. Sanjay, *et al* **[4-6]** found that the multiple peaks of noise spectrum observed in single bubbles cavitation around two axisymmetric headforms in water were resulted from several shock waves emitted during the collapse process. Arakeri, *et al* **[4-7]** stated that cavitation noise is a complex process that is not only affected by the degree of cavitation but also by the influence of the nuclei number density present in the fluid. Testud, *et al* in 2007 **[4-8]**, investigated the effect of geometry on the cavitation noise. In their experiment they stated that the acoustic noise in high degree of cavitation condition (develop cavitation) shows no differences between single-hole and multi-hole orifices.

In the present study, the cavitation noise spectrum is investigated for sodium cavitation using venturi channel since noise spectrum of sodium cavitation has not been analyzed in detail in the past. The results of the experiment are compared with the water cavitation noise spectrum conducted for the same test section geometry in order to understand the differences between sodium and water cavitation noise spectrums.

4.2 Experiment

4.2.1 Experimental Apparatus

In case of sodium cavitation, the experiment was conducted by using a sodium loop facility at Sukegawa Electric Co., Ltd. Argon gas was used as a cover gas pressure in the loop during the experiment. The downstream static pressure was measured by using a pressure transducer and the flow rate of liquid sodium was measured by using an

electromagnetic flow meter. The test section for this experiment is a venturi made from 316 SS with an inner diameter of 6.5 mm, an outer diameter of 21 mm, and a length of 20 mm. The detail explanation of this apparatus can be found in **Chapter 2.1** and **ref. [4-9]**.

While for the water cavitation, the experiment was conducted by using high-pressure water loop apparatus as explained in detail in **Chapter 2.2.1**. The test section used has the same diameter as that used for sodium cavitation experiment. It is also made from stainless steel since it will be used at temperatures higher than room temperature.

4.2.2 Experimental Condition

The experimental conditions for sodium cavitation experiment are listed in **Tables 4.1** and **4.2**. The minimum Re number during experiments was around 37700 at outer diameter (21 mm) and 122000 at inner diameter (6.5 mm) for sodium. While it was around 16000 at outer diameter (21 mm) and 53800 at inner diameter (6.5 mm) for water. Therefore the flow was turbulent.

Table 4.1 Experimental conditions of sodium cavitation experiment.

Na Temperature [°C]	Stagnant Pressure in the Expansion Tank, MPa absolute [MPa-a]
200-400	0.061-0.181

Table 4.2 Experimental conditions of water cavitation experiment.

Water Temperature [°C]	Stagnant Pressure in the Buffer Tank, MPa absolute [MPa-a]
56-90	0.101 (atmospheric pressure)

4.3 Results and Discussion

4.3.1 Noise Spectrum of Sodium Cavitation in Venturi Channel

The formation and collapse of cavitation bubbles produce acoustic noise that can be recorded. In case of large system such as in cooling pipes, the differentiation of sodium cavitation noise from the background noise can be used to judge whether cavitation occurs or not. This could prevent further damages caused by cavitation such as erosion on the material surface. **Figure 4.1** shows the resonance frequencies of the test section under uncirculated condition. The peaks of noise intensity corresponding to the resonance frequencies are around 1 kHz, 3 kHz, 5 kHz, 9 kHz, and 20 kHz.

It is found from the characteristics of noise signal that there are two typical cavitation conditions, namely intermittent and developed cavitation. Intermittent cavitation indicates that cavitation occurs intermittently for a few milliseconds and the noise signal fluctuates as the bubbles grow and collapse intermittently, while developed cavitation could occur for a relatively long time and the intensity of the noise signal is relatively constant.

Figures 4.2 (a) to **4.2 (g)** show the noise intensities spectrum at 200°C with the parameter of the stagnant pressure change. This figure also shows some resonance peaks similar with those obtained in **Fig. 4.1**. When the flow rate of liquid sodium is increased

gradually before the occurrence of cavitation, the intensity of flow noise with low frequency up to around 600 Hz increases and becomes saturated. As the flow rate is increased further, cavitation bubbles start to form which produce noise in the frequency from around 600 Hz up to 20 kHz. When cavitation condition changes from no cavitation to developed cavitation, the increase of the noise intensity is more significant at higher frequency region than at the lower frequency region. This might be caused by the rapid formation of cavitation bubbles due to reduction of static pressure at the venturi inlet and collapse/condensation of cavitation bubbles due to recovery of static pressure at the venturi outlet. At very low cavitation coefficient corresponding to developed cavitation condition and very high noise, the noise intensity becomes constant with magnitude of around -50 dB. This condition is caused by the relatively constant formation and collapse of cavitation bubbles due to choking condition.

It is found from the comparison in **Figs. 4.2 (a)** to **4.2 (g)** that the change of the stagnant pressure in the expansion tank from 0.061 MPa-a to 0.181 MPa-a does not have significant effect on the frequency spectrum of the noise intensity.

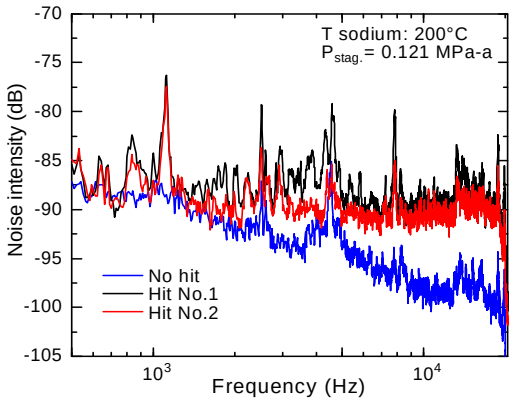

Fig. 4.1 Resonance frequency of the sodium test section.

The results of noise intensity spectrums at 300°C as shown in **Figs. 4.3 (a)** to **4.3 (g)** show similarity with those obtained at 200°C where the noise spectrum tends to increase at higher frequency region. At developed cavitation condition, the magnitude of the noise is also around -50 dB. A little instability of the noise spectrum was observed at 0.161 MPa-a.

Figures 4.4 (a) to **4.4 (f)** show the result at 400°C. At 400°C, some instabilities or fluctuations were observed (**Figs. 4.4 (a), 4.4 (b), 4.4 (d), 4.4 (e),** and **4.4 (f)**) clearly from hearing the noise sounds and observing the spectrum on computer monitor. In this unstable cavitation sometimes the magnitude of the noise intensity was as large as in the developed cavitation for a relatively long time, but then suddenly the noise became as low as in no cavitation conditions. The noise intensity fluctuated between low and high intensities. The fluctuations might be caused by the shedding process of cavitation bubbles due to more violent cavitation bubbles collapse, since at high temperature the vapor pressure will increase as well as the solubility of argon gas. This might create a more violent cavitation bubbles that disturb the flow. Therefore, any disturbances in the flow may have the possibility to disturb cavitation conditions **[4-10]**. The collapse of cavitation bubbles at downstream of the test section will in turn produce shock waves and reentrant flows traveling to the upstream direction. These shock waves and reentrant flows could disturb the flow that could stop cavitation suddenly. The flow velocity in the venturi could also decrease to very low value momentarily, which corresponds to the decrease of its noise intensity spectrum shown for K: 0.88 since noise is a function of

flow velocity (flow rate). It should be noted that the cavitation coefficient K in this figure was calculated when the noise spectrum became stable (no instabilities).

It is found from the data with temperatures ranging from 200°-400°C that the stagnant pressure change in the expansion tank does not affect the spectrum of the noise intensity at intermittent and developed cavitation for 200°, 300°, and 400°C. Therefore, it is independent of the stagnant pressure level.

The phenomena of the acoustic noise generation due to cavitation are explained in this way. When the liquid velocity is very high at the venturi channel the static pressure could fall to the saturated vapor pressure and evaporation could occur (K=1 theoretically) creating small cavitation bubbles. Because the inside pressure of the bubble is higher than the outside pressure (liquid static pressure), bubbles will expand. If there is some dissolved gas in the liquid, the dissolved gas could come out from the liquid and creating some micro nucleation bubbles. The mixing of the saturated vapor pressure that cause evaporation and dissolved gas partial pressures could increase the bubble inside pressure and the growth process will be larger. This large cavitation bubbles could collapse when the liquid static pressure recovers again to its original pressure at downstream of the venturi channel creating compression process to the bubble by the liquid. This collapse process will be very intense and the inside pressure and temperature of the collapse bubble will increase sharply. This high collapse energy will be transformed into acoustic noise pulse that hit the surface of the test section. The surface of the test section will vibrate and the vibration is transferred to the accelerometer. Reducing the pressure further will increase the evaporation process at venturi channel and more cavitation bubbles will be formed (K<1 theoretically). Bubbles will also grow larger because of

pressure decrease. Therefore the acoustic noise intensity will increase because of large cavitation bubbles collapse as measured by accelerometer.

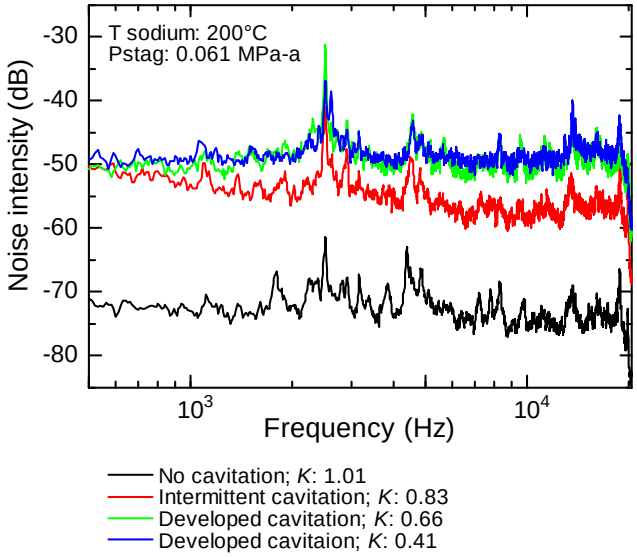

Fig. 4.2 (a) Noise intensity spectrum at 200°C and Pstag: 0.061 MPa-a.

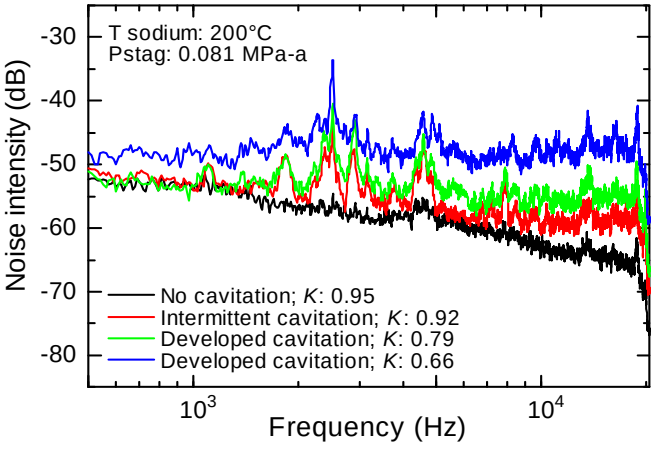

Fig. 4.2 (b) Noise intensity spectrum at 200°C and Pstag: 0.081 MPa-a.

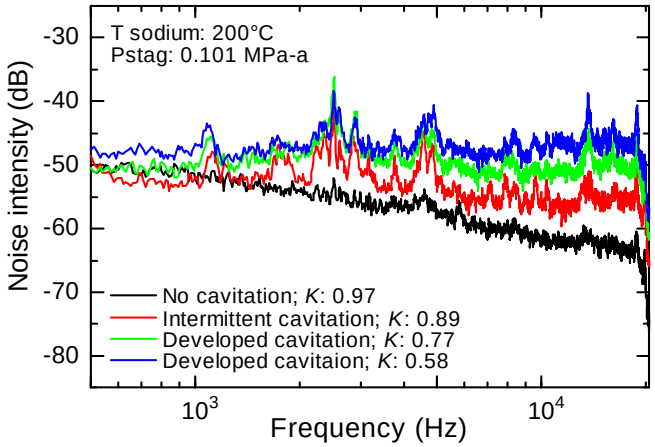

Fig. 4.2 (c) Noise intensity spectrum at 200°C and Pstag: 0.101 MPa-a.

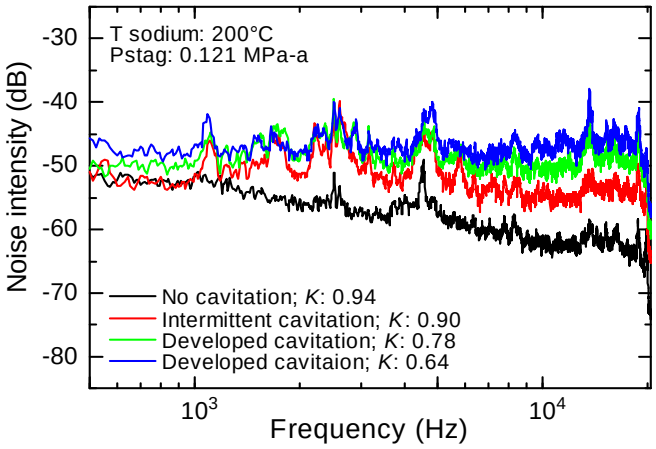

Fig. 4.2 (d) Noise intensity spectrum at 200°C and Pstag: 0.121 MPa-a.

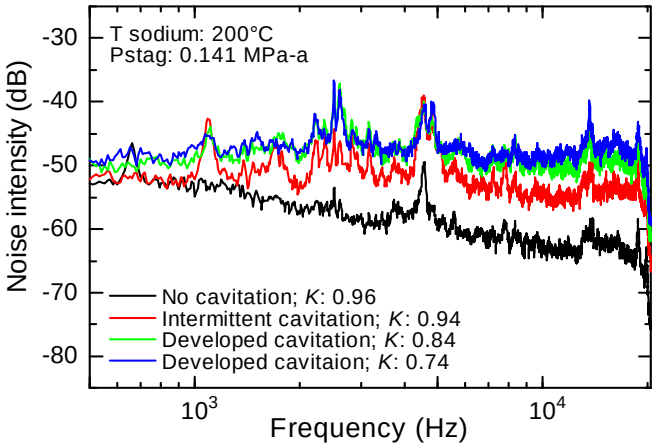

Fig. 4.2 (e) Noise intensity spectrum at 200°C and Pstag: 0.141 MPa-a.

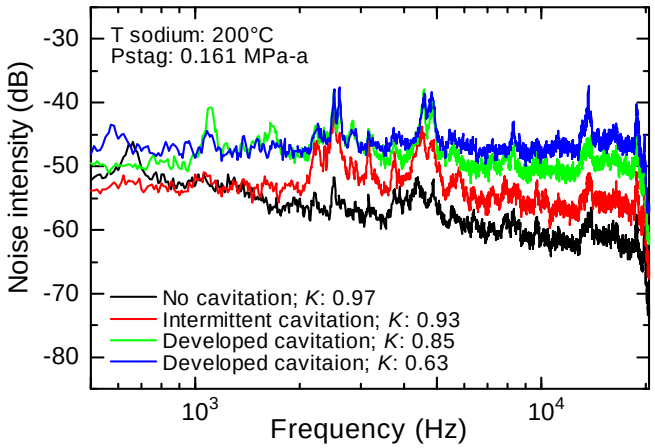

Fig. 4.2 (f) Noise intensity spectrum at 200°C and Pstag: 0.161 MPa-a.

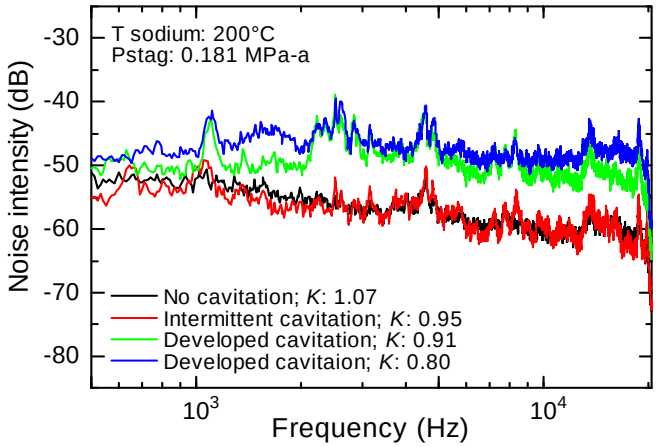

Fig. 4.2 (g) Noise intensity spectrum at 200°C and Pstag: 0.181 MPa-a.

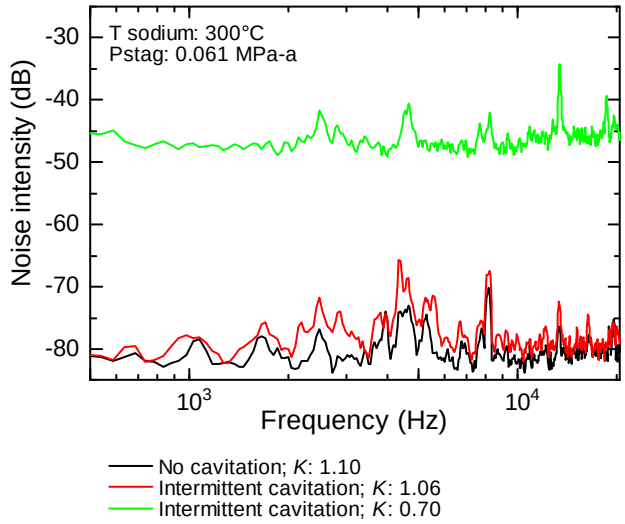

Fig. 4.3 (a) Noise intensity spectrum at 300°C and Pstag: 0.061 MPa-a.

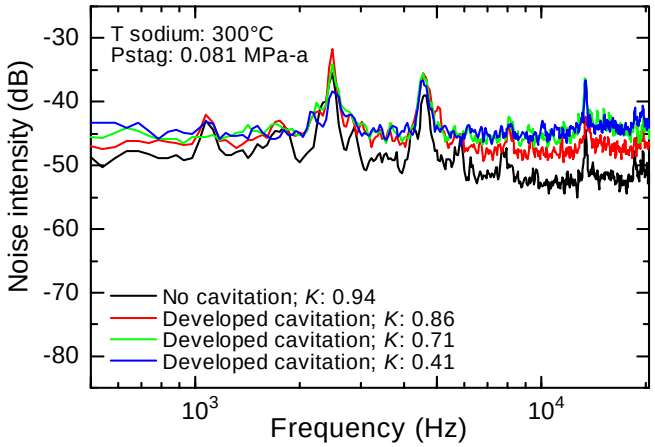

Fig. 4.3 (b) Noise intensity spectrum at 300°C and Pstag: 0.081 MPa-a.

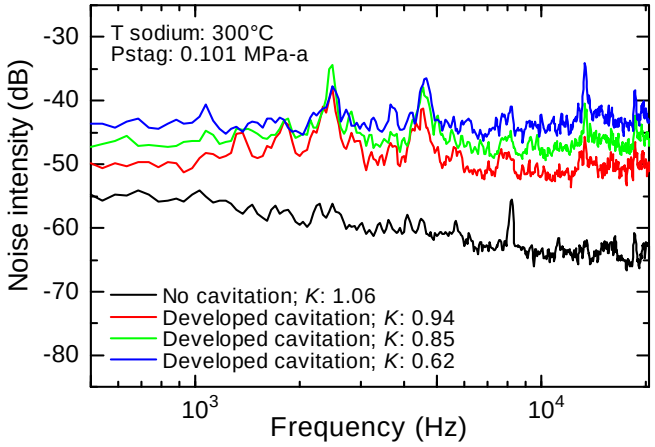

Fig. 4.3 (c) Noise intensity spectrum at 300°C and Pstag: 0.101 MPa-a.

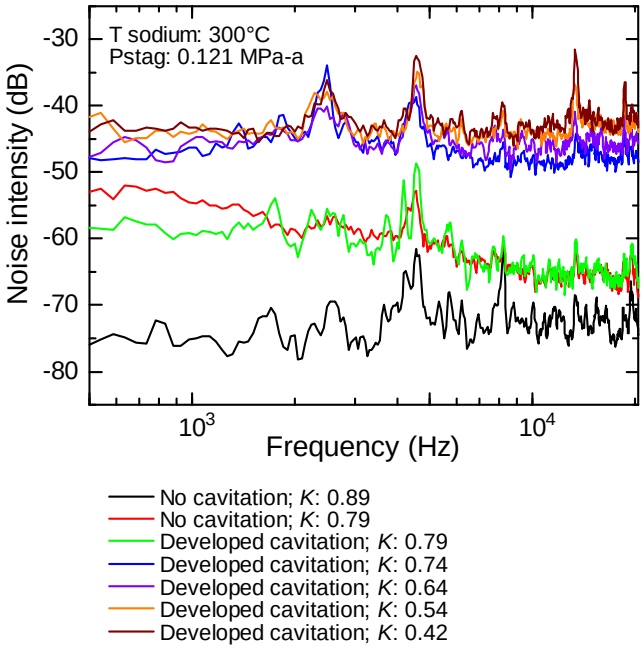

Fig. 4.3 (d) Noise intensity spectrum at 300°C and Pstag: 0.121 MPa-a.

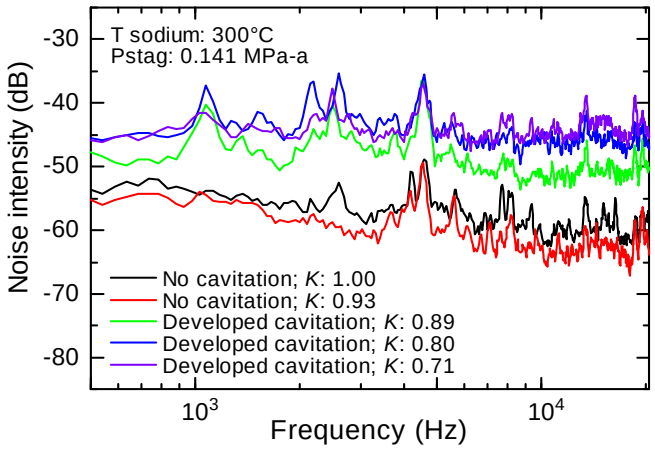

Fig. 4.3 (e) Noise intensity spectrum at 300°C and Pstag: 0.141 MPa-a.

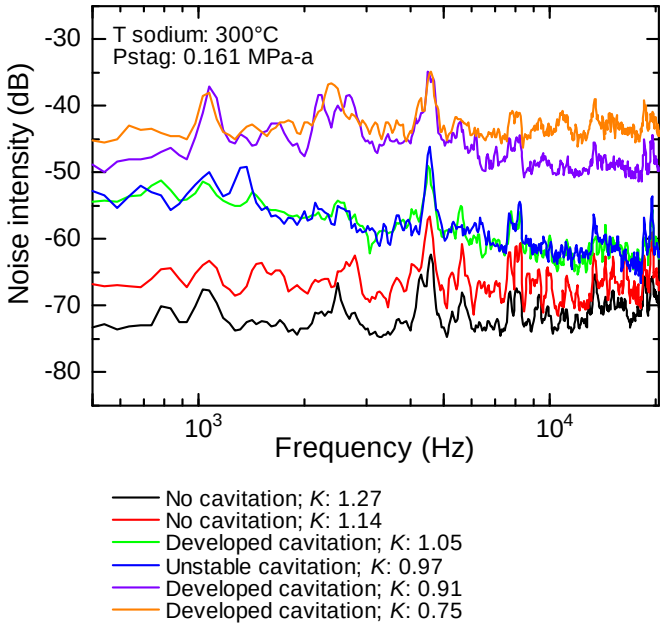

Fig. 4.3 (f) Noise intensity spectrum at 300°C and Pstag: 0.161 MPa-a.

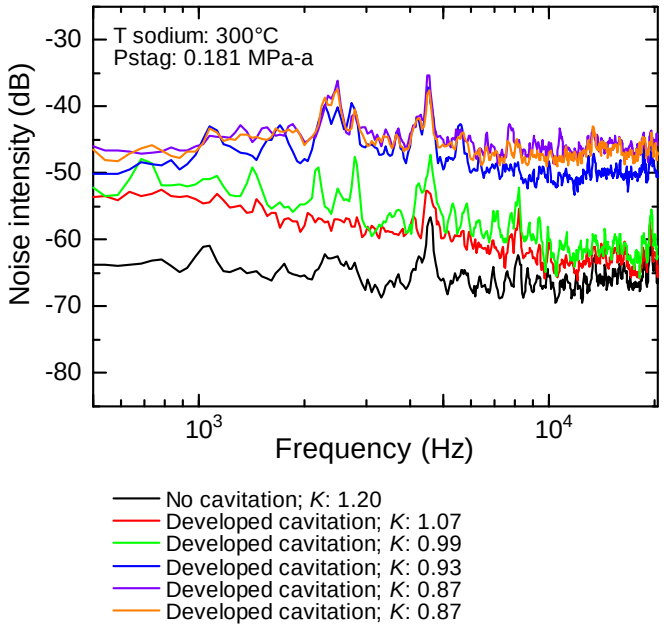

Fig. 4.3 (g) Noise intensity spectrum at 300°C and Pstag: 0.181 MPa-a. [119]

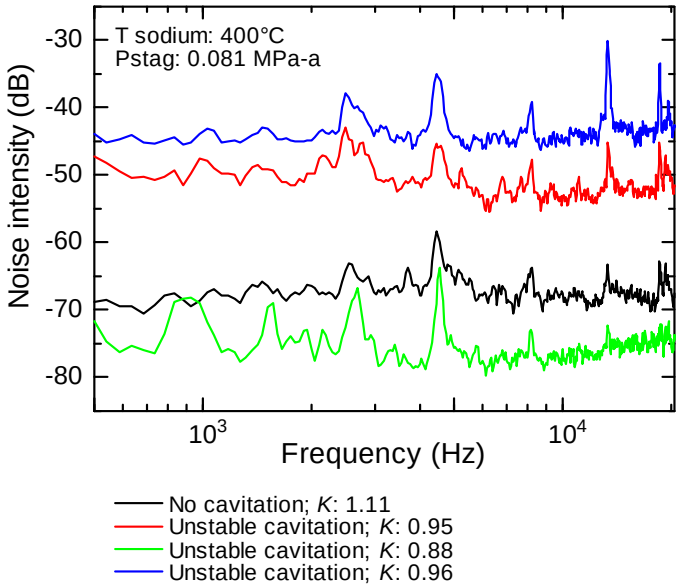

Fig. 4.4 (a) Noise intensity spectrum at 400°C and Pstag: 0.081 MPa-a.

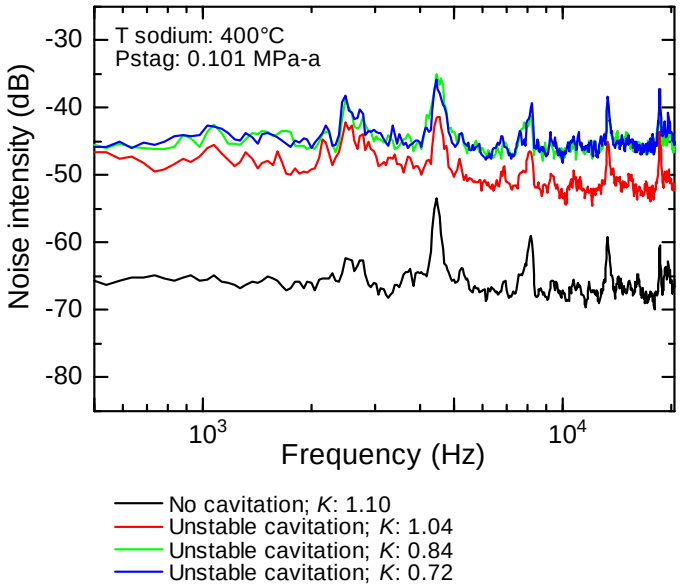

Fig. 4.4 (b) Noise intensity spectrum at 400°C and Pstag: 0.101 MPa-a.

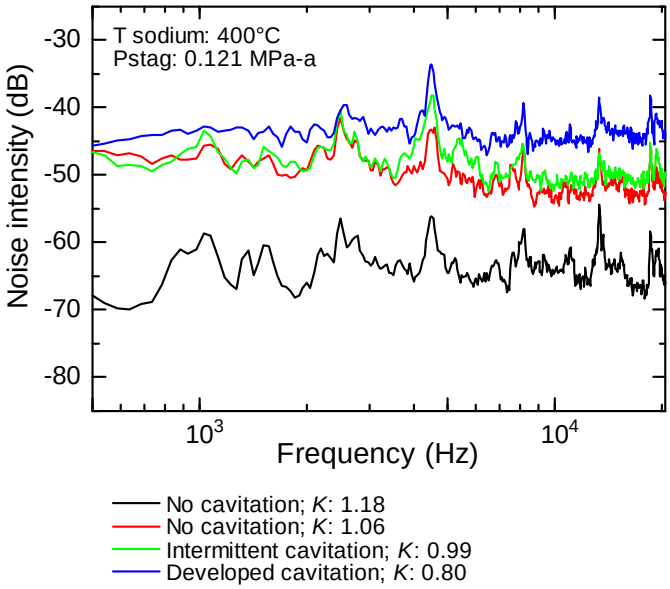

Fig. 4.4 (c) Noise intensity spectrum at 400°C and Pstag: 0.121 MPa-a.

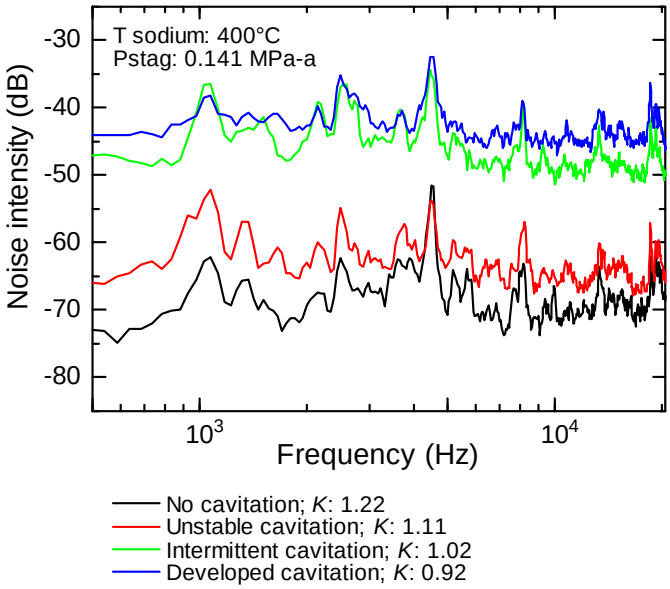

Fig. 4.4 (d) Noise intensity spectrum at 400°C and Pstag: 0.141 MPa-a.

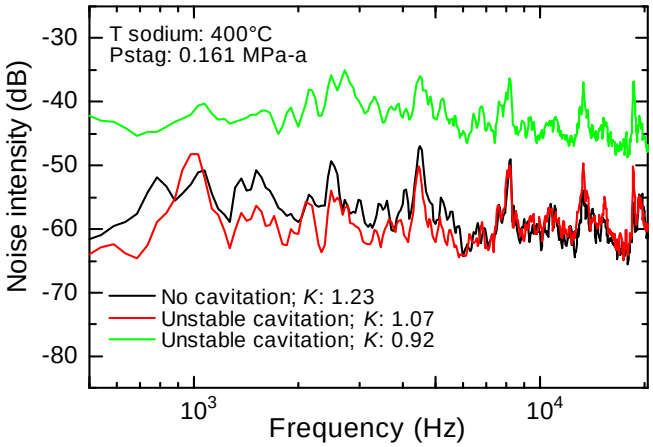

Fig. 4.4 (e) Noise intensity spectrum at 400°C and Pstag: 0.161 MPa-a.

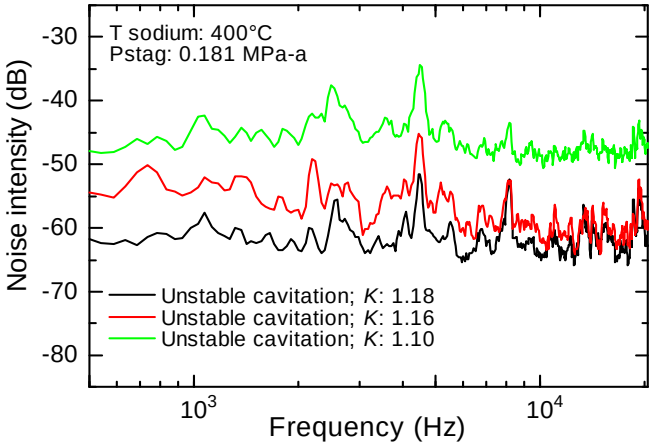

Fig. 4.4 (f) Noise intensity spectrum at 400°C and Pstag: 0.181 MPa-a.

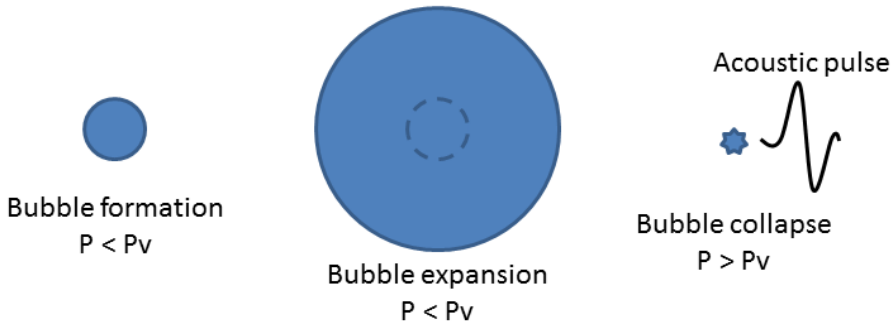

Fig. 4.5 Schematic of acoustic noise pulse formation.

4.3.2 Comparison of Cavitation Noise Spectrum in Sodium and Water for Venturi Channel

Experiments in water cavitation for comparison with sodium cavitation results were also conducted at 56°C, 74°C and 90°C because of the same kinematic viscosity with sodium at 200°C, 300°C and 400°C, and with the same venturi channel geometry (21 mm OD and 6.5 mm ID). The acoustic noise results are compared based on these similarities from no cavitation to developed cavitation. The results are considered satisfy when acoustic noise intensity becomes constant (developed cavitation condition). **Figures 4.6** shows the resonance frequency of the test section used in water with some multiple resonance peaks. **Figures 4.7 (a)** and **4.7 (b)** show the results of the acoustic noise spectrum in water at 56°C and 74°C for higher DO concentration. While **Figs. 4.8 (a)** to **4.8 (c)** show the results of the noise spectrum in water at 56°C, 74°C and 90°C for lower DO concentration. From the results of the noise spectrum in **Figs. 4.7** and **4.8**, it seems that there are no significant differences between the spectrums observed at 56°C to 90°C at higher and lower DO concentrations. The spectrums at no cavitation, intermittent and developed cavitation are similar in their shapes. The noise spectrum increases from

low to high frequency regions at developed cavitation condition with intensity of around -50 dB.

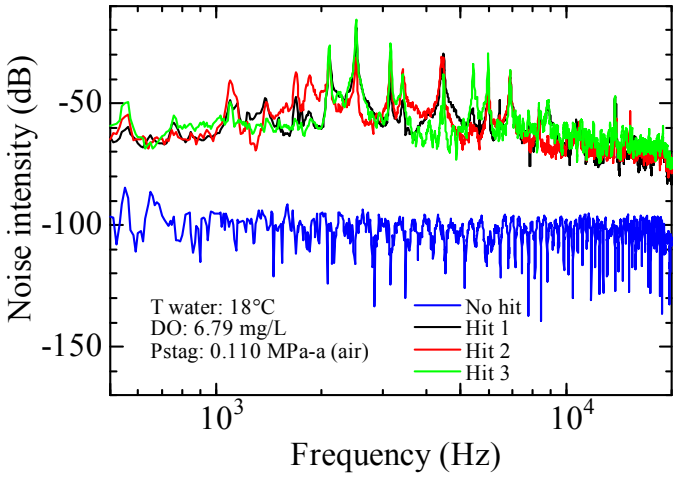

Fig. 4.6 Resonance frequency of the water test section.

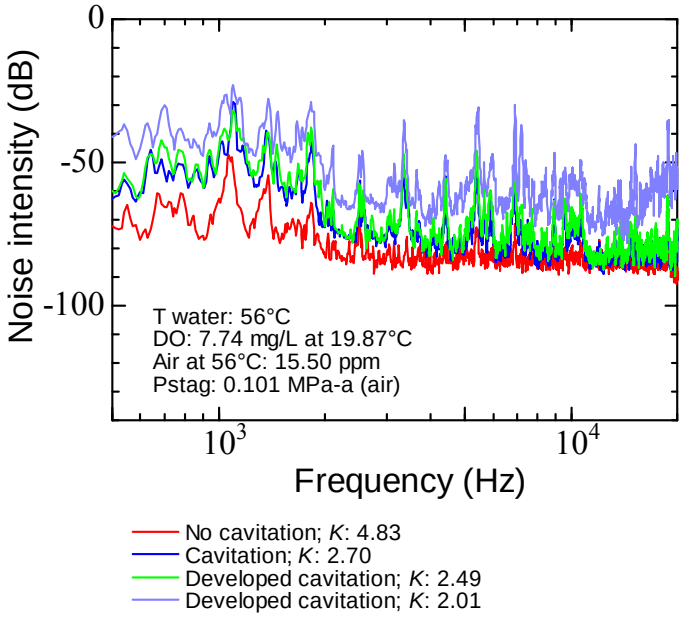

Fig. 4.7 (a) Noise spectrum in water at 56°C and higher DO concentration. [124]

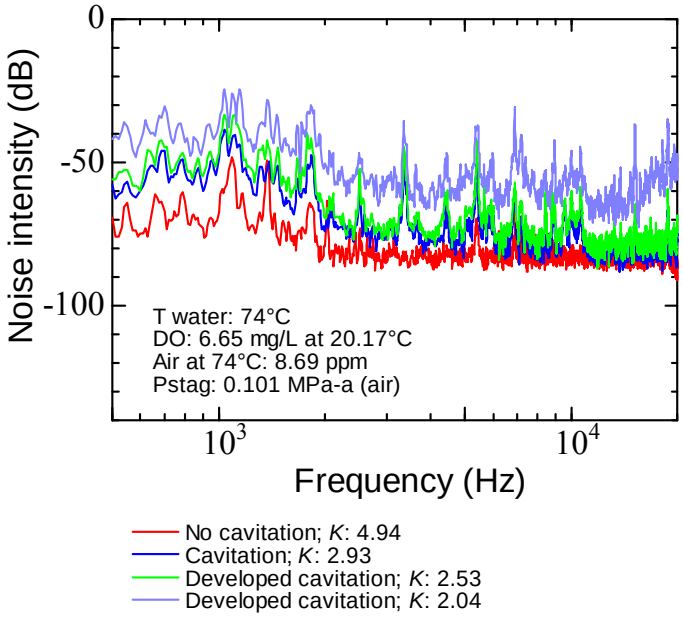

Fig. 4.7 (b) Noise spectrum in water at 74°C and higher DO concentration.

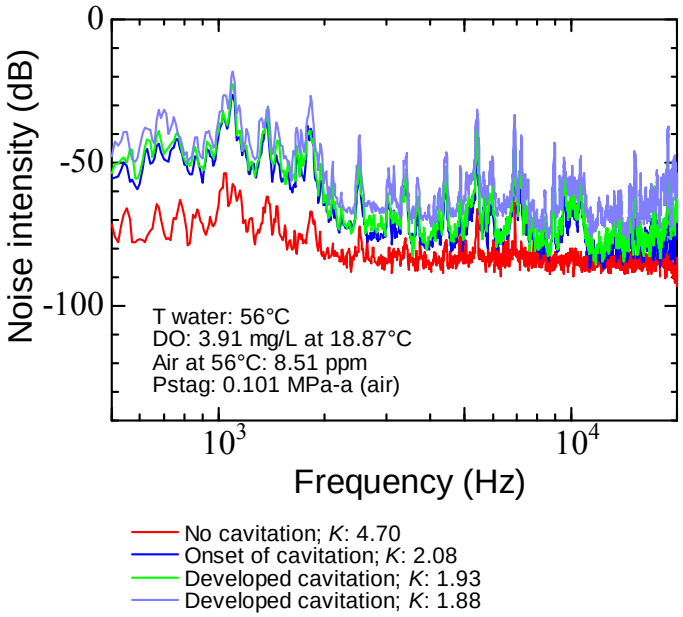

Fig. 4.8 (a) Noise spectrum in water at 56°C and lower DO concentration. [125]

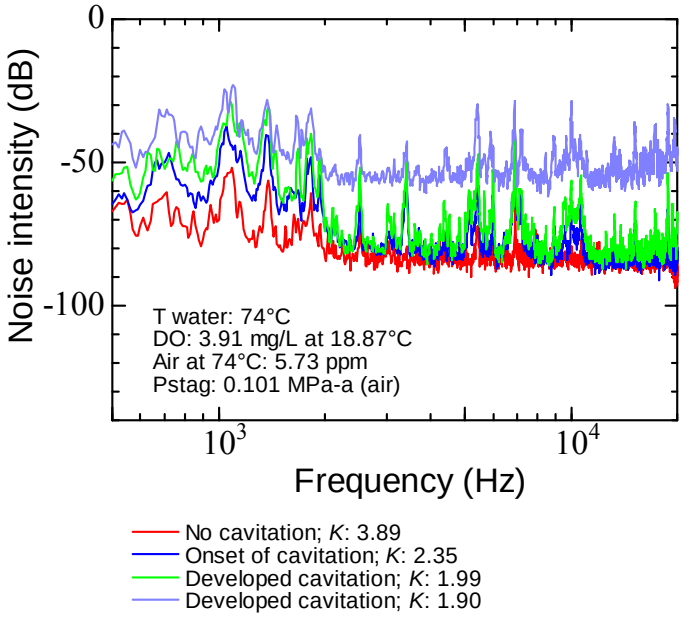

Fig. 4.8 (b) Noise spectrum in water at 74°C and lower DO concentration.

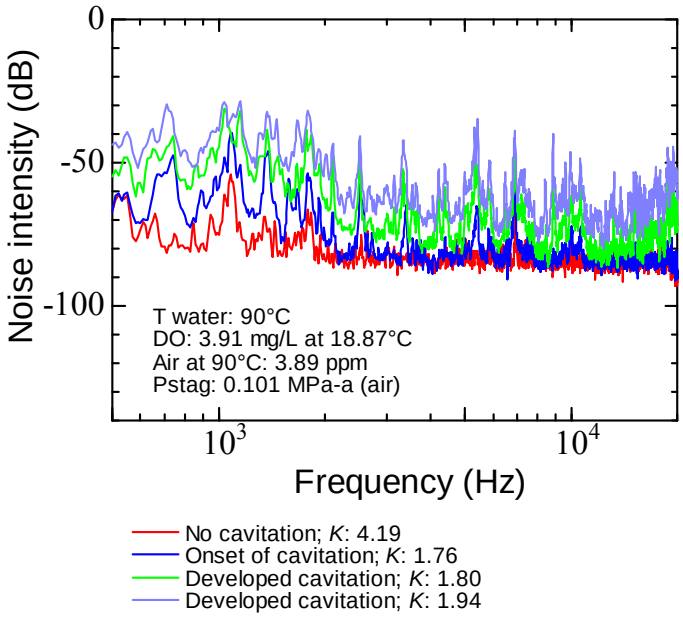

Fig. 4.8 (c) Noise spectrum in water at 90°C and lower DO concentration. [126]

Comparison of the acoustic noise intensity spectrum between water at 56°C, DO concentration 3.91 mg/L, Pstag: 0.101 MPa-a (air) and sodium at 200°C, Pstag: 0.101 MPa-a (argon) were shown in **Fig. 4.8 (d)**. The noise spectrum results between sodium and water are compared based on the acoustic noise spectrum recorded from no cavitation to developed cavitation conditions. The comparison shows that the noise intensity during the onset and developed of cavitation increase at high frequency region. The increase at high frequency region is clearer in case of sodium than in water. The physical phenomena of this result can be explained in this way. In sodium, the increase of the acoustic noise intensity at high frequency region is clearer than in water. These phenomena might be caused by the more dominant vaporous cavitation in sodium due to very low dissolved gas concentration. Therefore, cavitation bubbles can collapse rapidly in sodium without the damping effect from partial gas pressure of the dissolved gas. The rapid collapse will produce clear acoustic noise intensity increase at high frequency region. In case of water during no cavitation condition, the noise intensity spectrum increases at low frequency region (up to about 2 kHz). At onset and developed cavitation conditions, the noise spectrum gradually increases from low frequency up to 20 kHz. The increase of the noise at low frequency is probably caused by the noise coming from small nuclei due to dissolved gas. The dissolved gas at low pressure will precipitate, expand and collapse creating acoustic noise at low frequency region. Also because the collapse of the nuclei is not so rapid due to damping effect of the gas partial pressure, the acoustic noise produced might have low frequency. However since evaporation also occurs in water, the bubbles produced by evaporation might collapse rapidly creating high

frequency noise. Therefore in water the noise intensity occurs from low to high frequency regions. But because gaseous cavitation effect is more dominant, the increase of the noise intensity at high frequency region is not so clear as compared to sodium.

The results also show some spectrum peaks on the figures for both water and sodium that were resulted from resonance frequencies of the test section. Although both noise intensity spectrums in sodium and water cavitation cases are different in their shapes, however their noise intensities show sharp increase at higher frequency region than at lower one. The increase of the noise spectrum at higher frequency region is more apparent in case of sodium cavitation than in water cavitation. At develop cavitation, the noise spectrum increases at higher frequency region for both sodium and water. It indicates that the bubble behavior during developed cavitation stages for both sodium and water is similar. Also, because the frequency spectrum mostly changes at high frequency region during cavitation, therefore it can be used as a tool for the detection of cavitation in the flow.

The acoustic noise in sodium and water are influenced by some important factors such as the transmission of sound in the liquid (sound velocity), sound intensity and bubble fraction. The velocity of sound in the sodium and water are very high as shown in **Tables 3.3** and **3.4** above. In liquid metal and water, the occurrence of cavitation will produce bubbles that can change the sound transmission. The sound intensity and velocity can decrease due to some fraction of bubbles present in the liquid. Even small amount of bubbles can significantly reduce sound velocity and intensity as shown by **[4-11]**. However in the experiment the venturi channel geometry (21 mm OD and 6.5 mm ID) is smaller than the decrease of sound velocity and intensity due to cavitation bubbles

as observed from experiment in water by Huang, *et al* **[4-11]**. Therefore in the experiment it is assumed that sound intensity decrease is very low because of the small diameter of the test section. And acoustic noise can be easily transmitted to the accelerometer.

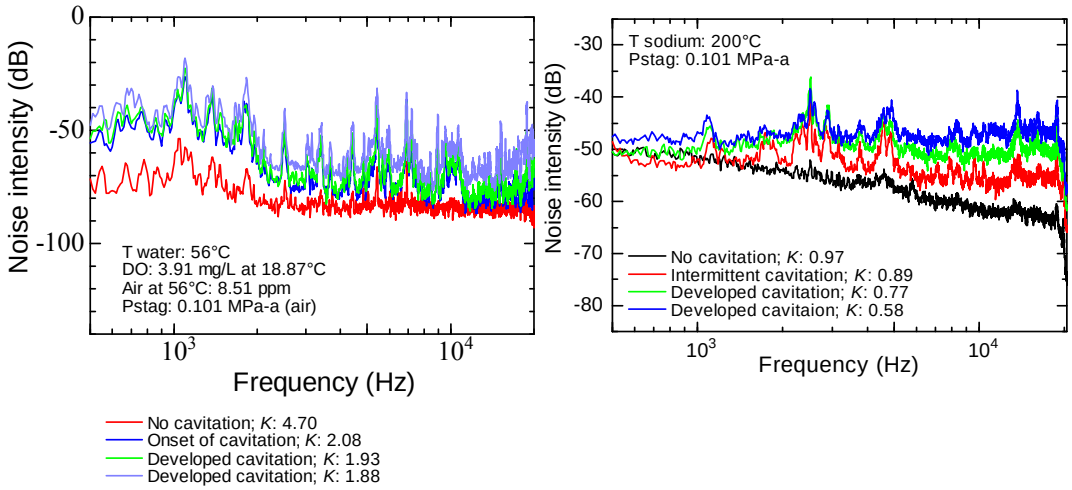

Fig. 4.8 (d) Noise spectrum comparison in water at 56°C and sodium at 200°C.

4.3.3 Numerical Simulation of Cavitation Spectrum

A numerical simulation of noise spectrum resulting from the growth and collapse of cavitation bubbles were performed in this study. The purpose is to understand how the spectrum is generated during the growth and collapse of cavitation bubble.

4.3.3.1 Keller-Miksis Equation

The equation used for the simulation is the Keller-Miksis equation **[4-12]** that describes the radial motion of two-coupled spherical bubbles in a compressible liquid. The Keller-Miksis equation is stated as:

$$\left(1-\frac{dR_i}{dt}\frac{1}{c}\right)R_i\frac{d^2R_i}{dt^2}+\left(\frac{3}{2}-\frac{dR_i}{dt}\frac{1}{2c}\right)\left(\frac{dR_i}{dt}\right)^2 \\ -\frac{1}{\rho}\left(1+\frac{dR_i}{dt}\frac{1}{c}\right)p_{s,i}+\frac{R_i}{\rho c}\frac{dp_{s,i}}{dt}-\sum_{j=1,j\neq 1}^{N}\frac{1}{D_{ij}}\frac{d\left(R_j^2\dot{R}_j\right)}{dt} \quad \text{.....(4-1)}$$

where $R_i = R_i(t)$ is the instantaneous radius of bubble i, D_{ij} is the center-to-center distance between bubbles i and j, and the over dots denote the time derivate. The surrounding liquid is assumed to be water at temperature of 56°C. The density ρ = 985.228 kg/m^3, viscosity μ = 0.000496 kg/m.s, sound speed c = 1500 m/s, surface tension σ = 0.0669 N/m, and vapor pressure p_v = 16469.79 Pa.

$$p_{s,i} = p_{b,i} - \frac{2\sigma}{R_i} - \frac{4\mu\dot{R}_i}{R_i} - p_\infty \text{ for } i = 1,2 \quad \text{.....(4-2)}$$

The pressure inside bubble is determined by **[4-13]**

$$p_{b,i} = \left(p_v + \frac{2\sigma}{R_{i0}}\right)\left(\frac{R_{i0}^3 - h_i^3}{R_i^3 - h_i^3}\right)^\kappa \quad \text{.....(4-3)}$$

where R_{i0} is the ambient radius and h_i is the hard-core radius ($R_{i0}/8.54$ for air **[4-13]**) and p_∞ is the far field pressure in the liquid. The polytrophic exponent of the gas, κ is assumed to be equal to its specific heat ratio γ (1.4 for air). The pressure wave emitted from pulsating sphere is calculated by **[4-12]**

$$p_i = \frac{\rho}{r_i}\frac{d\left(R_i^2\dot{R}_i\right)}{dt} = \frac{\rho}{r_i}\left(2R_i\dot{R}_i^2 + R_i^2\ddot{R}_i\right) \quad \text{.....(4-4)}$$

In order to solve the differential equation, an ODE45 solver utilizing Runge-Kutta method is used to solve the change of the bubble radius with time as

$$
\begin{aligned}
&R_{n+1} = R_n + \frac{1}{6}[k1 + 2k2 + 2k3 + k4] \\
&k1 = h.f(t_n, R_n) \\
&k2 = h.f\left(t_n + \frac{1}{2}h, R_n + \frac{1}{2}k1\right) \\
&k3 = h.f\left(t_n + \frac{1}{2}h, R_n + \frac{1}{2}k2\right) \\
&k4 = h.f(t_n + h, R_n + k3)
\end{aligned}
\qquad \text{.....(4-5)}
$$

where $k1$, $k2$, $k3$, and $k4$ are the deltas based on the slope at the beginning, midpoint and end of the interval. $f(t,R)$ is the derivative of bubble radius R with respect to time t, and bubble radius R, while h is the time step used for the calculation (Δt).

4.3.3.2 Fast Fourier Transform (FFT)

Fourier analysis stated that a complicated mathematical function that depends on time could be transformed into different function as the sum of sines and cosines of different frequencies, or in other word from time domain to frequency domain. In this calculation, the calculated pressure waves are presented in the time domain and assumed to be the sum of sines and cosines waves with different frequencies. Therefore, to change the pressure wave result emitted from pulsating sphere from the time domain to frequency domain, a Fast Fourier Transform (FFT) is used. FFT is an algorithm to compute the Discrete Fourier Transform (DFT) of a sequence of values and decompose it into components of different frequencies. FFT transforms vectors of length N by:

$$X(k) = \sum_{j=1}^{N} x(j)\omega_N^{(j-1)(k-1)} \quad k = 0,1,...,N-1 \qquad \text{.....(4-6)}$$

where

$$
\begin{aligned}
&\omega_N = e^{(-2\pi i)/N} = \cos(2\pi i / N) - i\sin(2\pi i / N) \\
&= \mathrm{Re}\left\{e^{(-2\pi i)/N}\right\} - i\,\mathrm{Im}\left\{e^{(-2\pi i)/N}\right\}
\end{aligned}
\qquad \text{.....(4-7)}
$$

4.3.3.3 Initial and Boundary Condition

The initial condition for the calculation is

$$R(t=0)=10\,\mu m$$
$$\frac{dR}{dt}(t=0)=0 \qquad \text{.....(4-8)}$$

The boundary condition for the calculation is assumed to be the change of the far field pressure in the liquid p_∞ with time. The value is the static pressure change at inlet, venturi and outlet parts of the test section computed from the dynamic pressure and total pressure (P_{static} + $P_{dynamic}$ = constant = 0.101325 MPa). This value is calculated based on the experiment in water cavitation conducted at no cavitation, onset cavitation and developed cavitation conditions at 56°C. The value is plotted in **Fig. 4.8** below, where negative value represents vacuum condition.

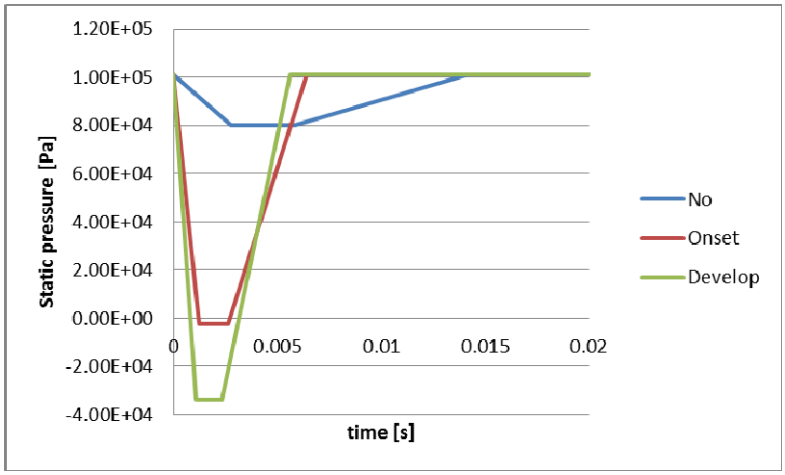

Fig. 4.9 Boundary conditions for calculation.

In this calculation it is assumed that the initial bubble radius of bubble 1 is the same with bubble 2 (R10=R20=10 μm). It is also assumed that no heat transfer occurs from or to the bubble during the growth and collapse process (bubbles are in thermal equilibrium with the fluid). Also the bubble is assumed to be remaining spherical during the growth and collapse.

4.3.3.4 Result of Calculation

The calculation result of the change of bubble radius with time is presented in **Figs. 4.10 (a)** to **4.10 (c)**. The result shows that at no cavitation condition, the bubble did not grow into larger one because of the damping from the liquid pressure, surface tension and viscosity. Reducing the far field pressure into smaller values at onset condition increases the bubble radius. Bubble starts to grow into larger one with diameter of around 0.002 m (2 mm) as shown at D_{12} = infinity, D_{12} = 300*R10 and D_{12} = 200*R10. At develop condition the change of the bubble radius is the largest of all as compared at no cavitation and onset cavitation conditions. It is caused by the higher pressure inside of the bubble following the change of the far field pressure in the liquid. Therefore, this large difference between inside pressure and the far field pressure increases the growth rate of the bubble from 10 μm to around 0.013 m (13 mm) for D_{12} = infinity, 0.010 m (10 mm) for D_{12} = 300*R10 and 0.0095 m (9.5 mm) for D_{12} = 200*R10. The figure also shows that bubble growth for center-to-center distance between bubble D_{12} = infinity is the largest as compared to D_{12} =300*R10 or D_{12} =200*R10. Since bubble 1 is equal to bubble 2 (R10=R20=10 μm), therefore the result of bubble 2 shows similarity with

bubble 1. The results also show that after the bubbles grow into larger ones and collapse at onset of cavitation, the collapse bubbles rebound several times before completely disappear because of the damping from viscosity and liquid compressibility. However, at developed cavitation the rebound process is not so large and the bubble seems to completely disappear after some small and short rebound steps.

The result of the pressure change with the change of center-to-center distance D_{12} between bubble 1 and 2 is presented in **Figs. 4.11 (a)** to **4.11 (c)** calculated at a distance r_i = 1 m from the bubble center. The calculated result shows that although the growth of the bubble radius at D_{12} = infinity is the largest; however the pressure pulse created is the smallest at developed cavitation condition. The largest pressure pulse is created when D_{12} = 200*R10 as shown in the **Fig. 4.11 (c)**. The peak of the pressure is produced during the collapse process since at this process the acceleration and velocity terms are the largest as shown in **Fig. 4.12**.

Result of the spectrum from the pressure pulse at D_{12} = infinity, D_{12} =300*R10 and D_{12} =200*R10 is shown in **Figs. 4.13 (a)** to **4.13 (c)** below. The spectrums were generated using the data of the pressure pulses shown in **Fig. 4.12 (a)** to **4.12 (c)** in a time period from 10^{-12} s to 0.01 s. The sampling frequency assumed is 2 MHz. The acoustical pressure is presented in dB values

$$\mathrm{dB} = 10.\log_{10}\left(\frac{\mathrm{P}}{\mathrm{P}_0}\right) \qquad \textbf{(4-9)}$$

where P is the acoustical pressure of the spectrum and P_0 is atmospheric pressure (0.101 MPa). The figure shows the result with the change of the conditions from no cavitation to

developed cavitation. The intensity of the acoustical pressure increases following the change from no cavitation to developed cavitation condition, which is from the value of around -1.8x10^2 dB at no cavitation to around -8x10^1 dB at develop cavitation. The intensity of the acoustical pressure is relatively flat from lower frequency up to about 10 kHz, and gradually increasing up to 20 kHz. The result of the spectrum at D_{12} = infinity shows similarity with the results at D_{12} = 200*R10 and D_{12} = 300*R10 where the spectrum increases at high frequency region and flat at lower one.

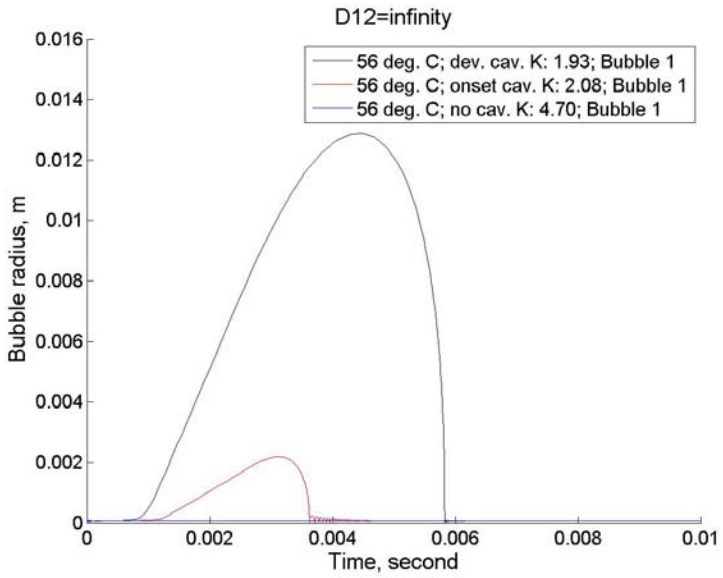

Fig. 4.10 (a) Bubble radius change with center-to-center distance $D_{12} = \infty$.

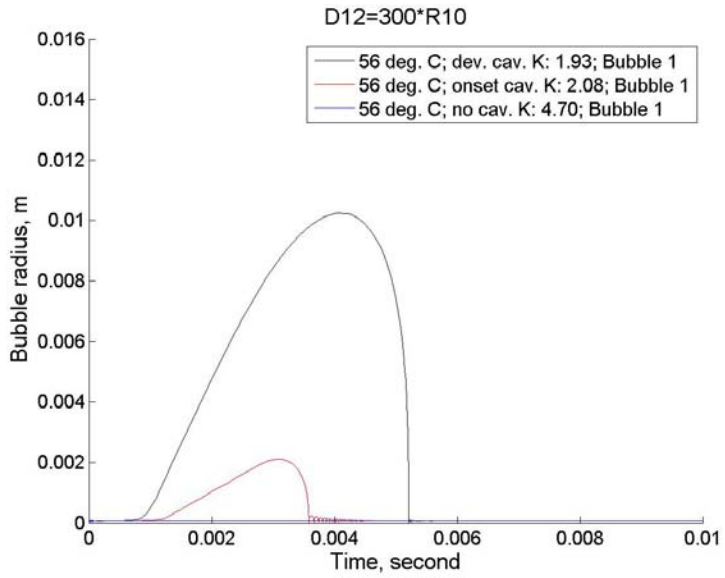

Fig. 4.10 (b) Bubble radius change with center-to-center distance D_{12} = 300xR10.

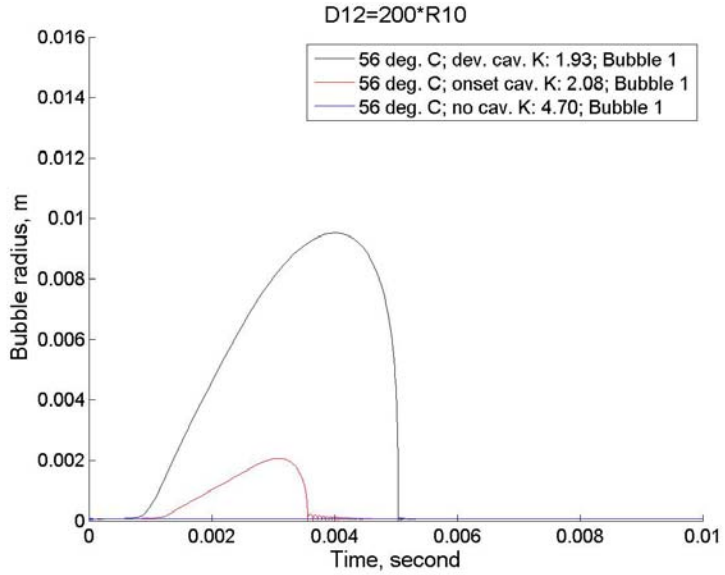

Fig. 4.10 (c) Bubble radius change with center-to-center distance D_{12} = 200xR10.

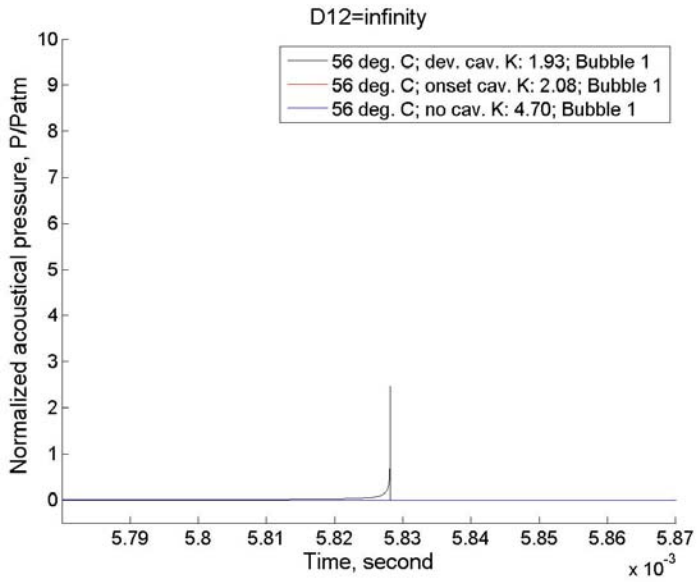

Fig. 4.11 (a) Pressure change with center-to-center distance $D_{12} = \infty$.

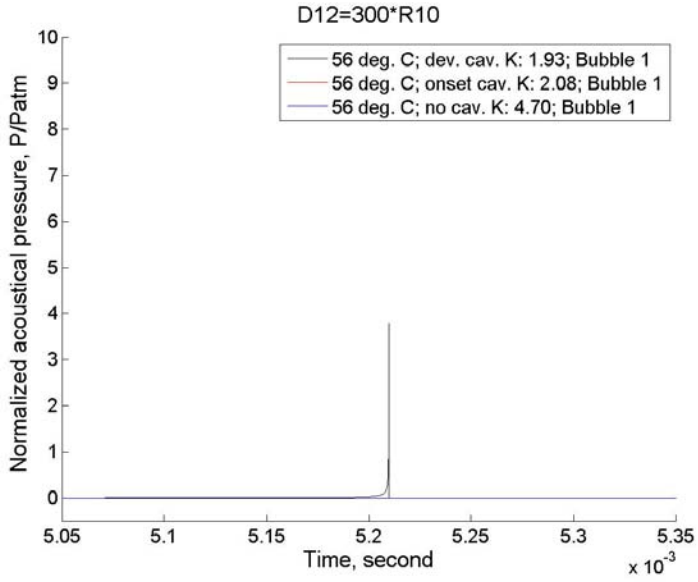

Fig. 4.11 (b) Pressure change with center-to-center distance D_{12} = 300xR10.

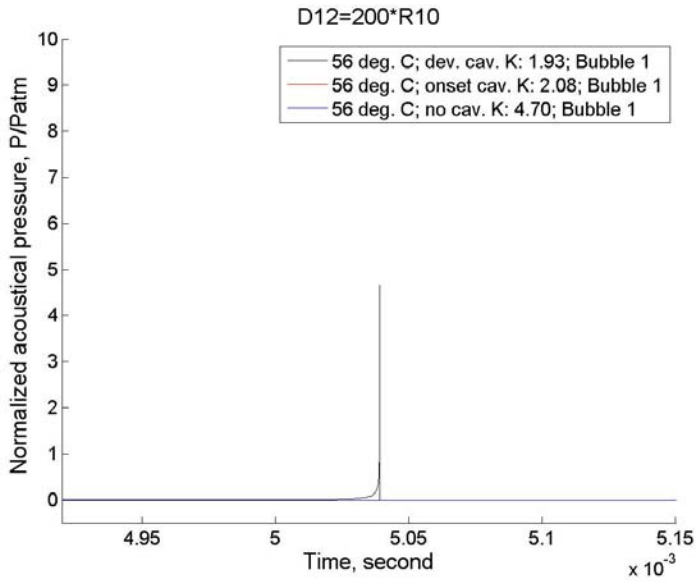

Fig. 4.11 (c) Pressure change with center-to-center distance D_{12} = 200xR10.

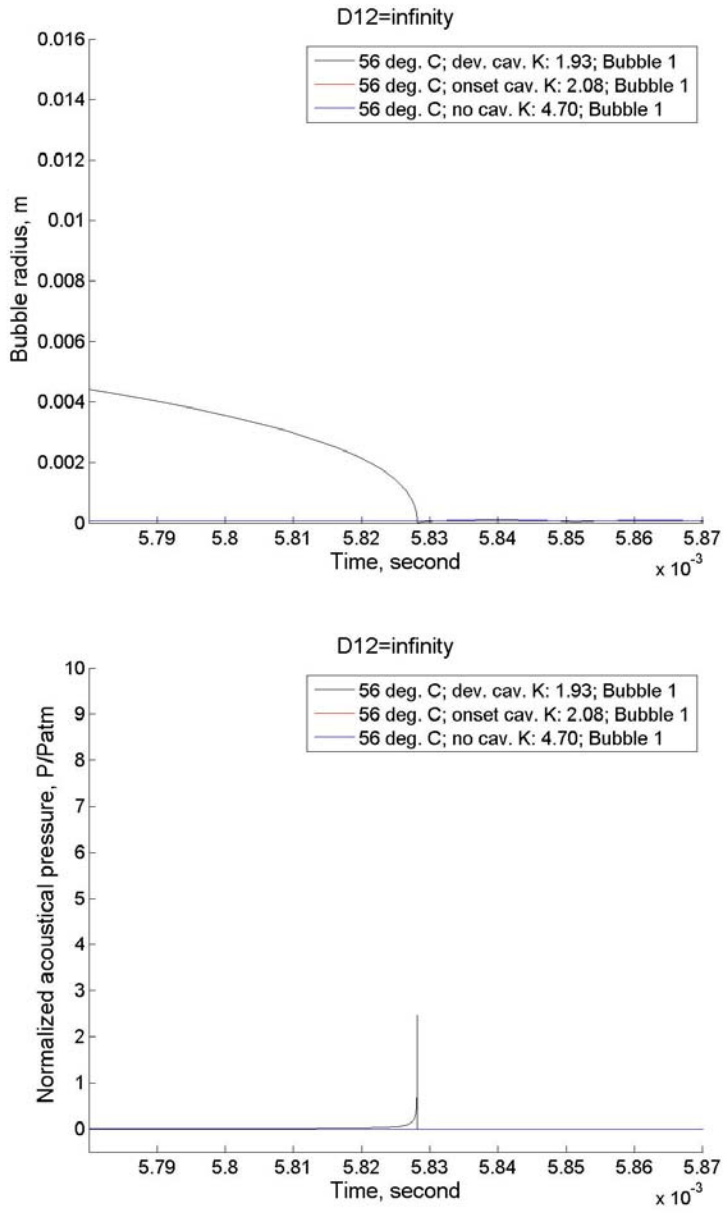

Fig. 4.12 Enlarge of bubble collapse at developed cavitation condition (upper figure) and its corresponding pressure pulse (lower figure) with center-to-center distance $D_{12} = \infty$.

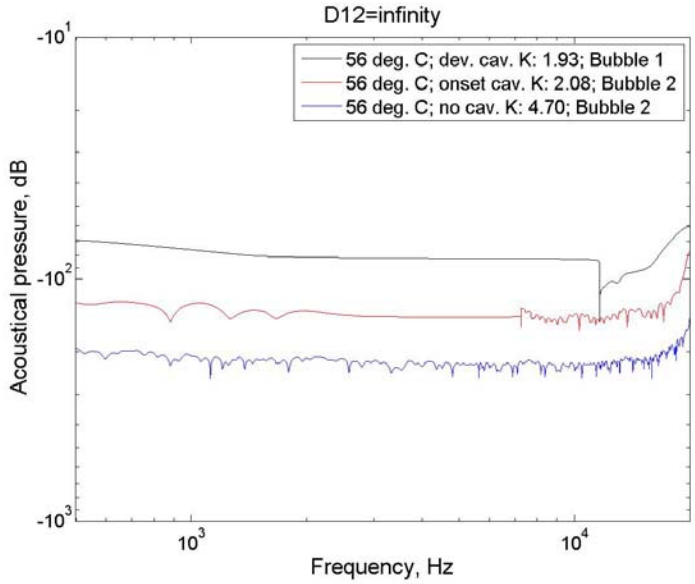

Fig. 4.13 (a) Acoustical pressure change with center-to-center distance $D_{12} = \infty$.

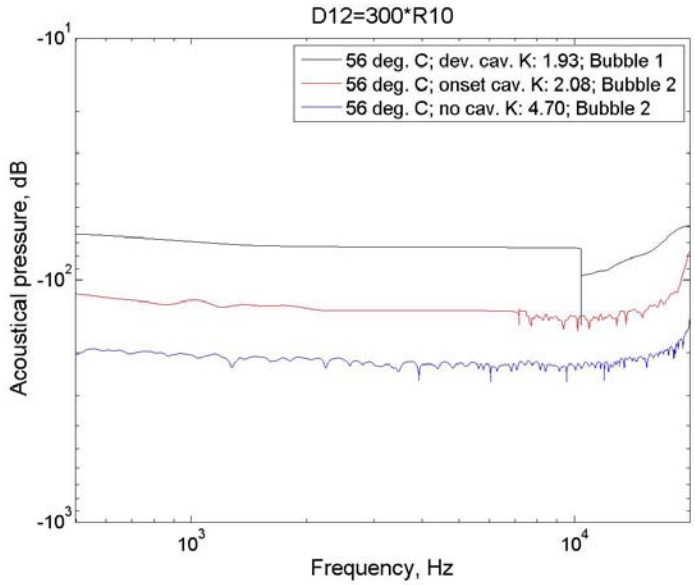

Fig. 4.13 (b) Acoustical pressure change with center-to-center distance $D_{12} = 300$xR10.

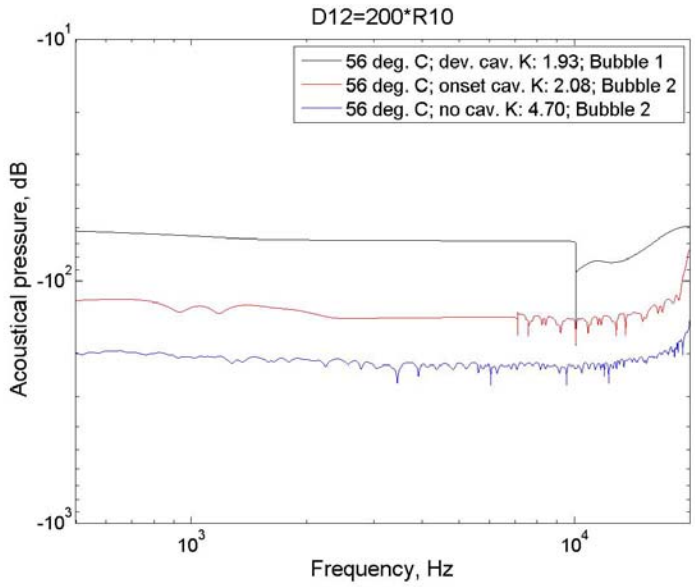

Fig. 4.13 (c) Acoustical pressure change with center-to-center distance D_{12} = 200xR10.

4.3.3.5 Thermal Effect on Bubble Growth

If the bubble temperature is different with the liquid temperature (not in thermal equilibrium with the liquid), then the heat transfer can have important effect on the bubble growth rate. The heat diffusion equation in the liquid is stated that

$$\frac{\partial T}{\partial t}+\frac{dR}{dt}\left(\frac{R}{r}\right)^2\frac{\partial T}{\partial r}=\frac{\alpha_l}{r^2}\frac{\partial}{\partial r}\left(r^2\frac{\partial T}{\partial r}\right) \quad \textbf{(4-10)}$$

The heat supplied to the bubble from the liquid is related by

$$\frac{\partial R}{\partial t}=\frac{\lambda_l}{\rho_v L}\left(\frac{\partial T}{\partial r}\right) \quad \textbf{(4-11)}$$

where L is the latent heat of vaporization. During bubble growth, the heat supplied to the interface creating a thermal boundary layer on the bubble wall. As for any diffusive process, the order magnitude of the boundary layer thickness is $\sqrt{\alpha_l t}$ where $\alpha_l=\lambda_l/\rho_l c_{pl}$ is

the thermal diffusivity of the liquid (λ_l, ρ_l and c_{pl} are the conductivity, density and heat capacity of the liquid). The typical temperature gradient within the boundary layer is $\Delta T/\sqrt{\alpha_l t}$, where $\Delta T = T_\infty - T_B$, the difference between liquid temperature and bubble temperature. According to Fourier's law, the conductive heat flux towards the interface is then of the order of $\Delta T/\sqrt{\alpha_l t}$ **[4-14]**. The energy balance express that at any time the heat supplied by conduction to the interface of area $4\pi R^2$ is used for vaporization and causes the increase of the mass of vapor $\frac{4}{3}\pi R^3 \rho_v$ inside the bubble (ρ_v is the vapor density). Hence, the energy balance can be written as

$$\lambda_l \frac{\Delta T}{\sqrt{\alpha_1 t}} 4\pi R^2 = \frac{d}{dt}\left(\frac{4}{3}\pi R^3\right)\rho_v L \quad \text{.....(4-12)}$$

Figures 4.14 (a) to 4.14 (c) show the comparison of the bubble radius, pressure and acoustical pressure without the difference of the liquid and bubble temperature, and with the difference of the liquid and bubble temperature of 20°C. The results show that the bubble radius will grow larger with temperature difference of 20°C as compared without temperature difference as shown in **Fig. 4.14 (a)**. The bubble slightly grows to around 0.011 m (11 mm) as compared to 0.010 m (10 mm) at developed cavitation condition. However, at intermittent condition the change of the bubble radius is noticeable between the upper and lower figures of **Fig. 4.14 (a)**. The bubble grows to around 0.004 m (4 mm) from around 0.002 m (2 mm), an increase of around 2 mm. At no cavitation condition, the results are about the same between the upper figure and lower figure where the bubble does not grow significantly.

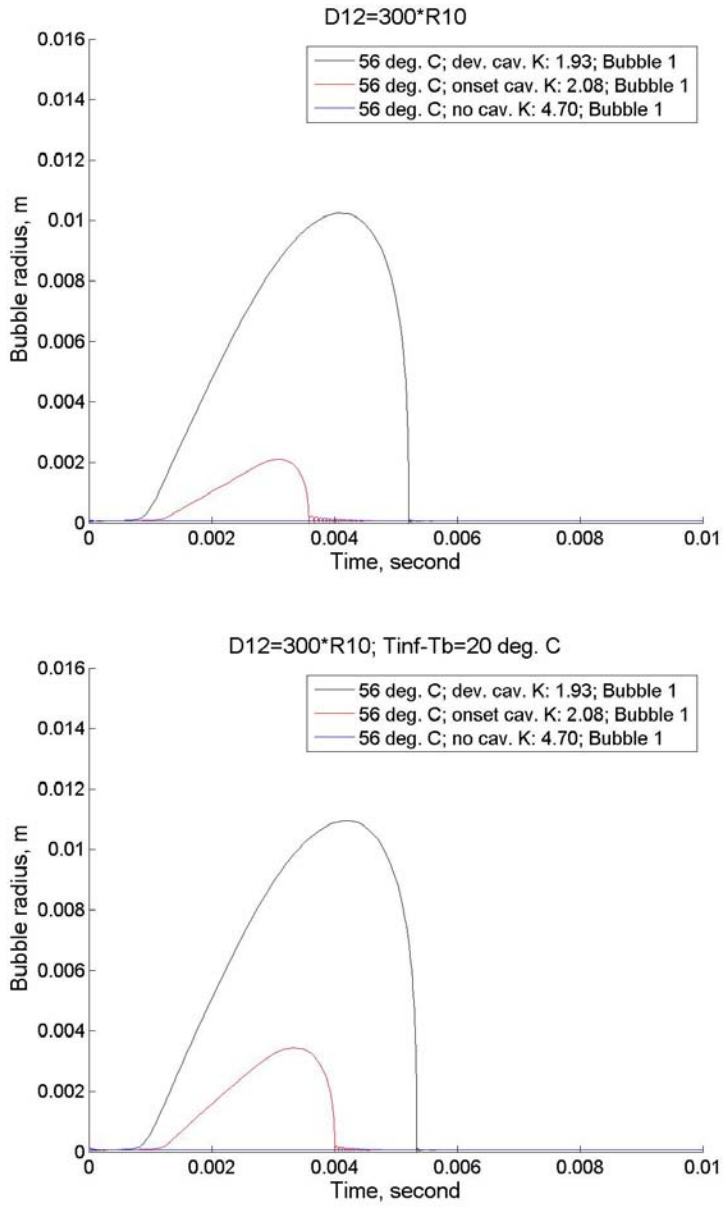

Fig. 4.14 (a) Comparison of bubble radius change with center-to-center distance D_{12}= 300xR10. Upper figure ($T_\infty - T_B = 0^\circ C$), lower figure ($T_\infty - T_B = 20^\circ C$).

Figure 4.14 (b) shows that the result with temperature difference of 20°C between liquid and bubble temperature have slightly higher normalized pressure pulse (about 4.5) as compared to without temperature difference (about 4). However, the noise

spectrums as shown in **Fig. 4.14 (c)** are similar for the bubbles with and without temperature difference, where the acoustical pressure increases at higher frequency region compared to lower frequency region.

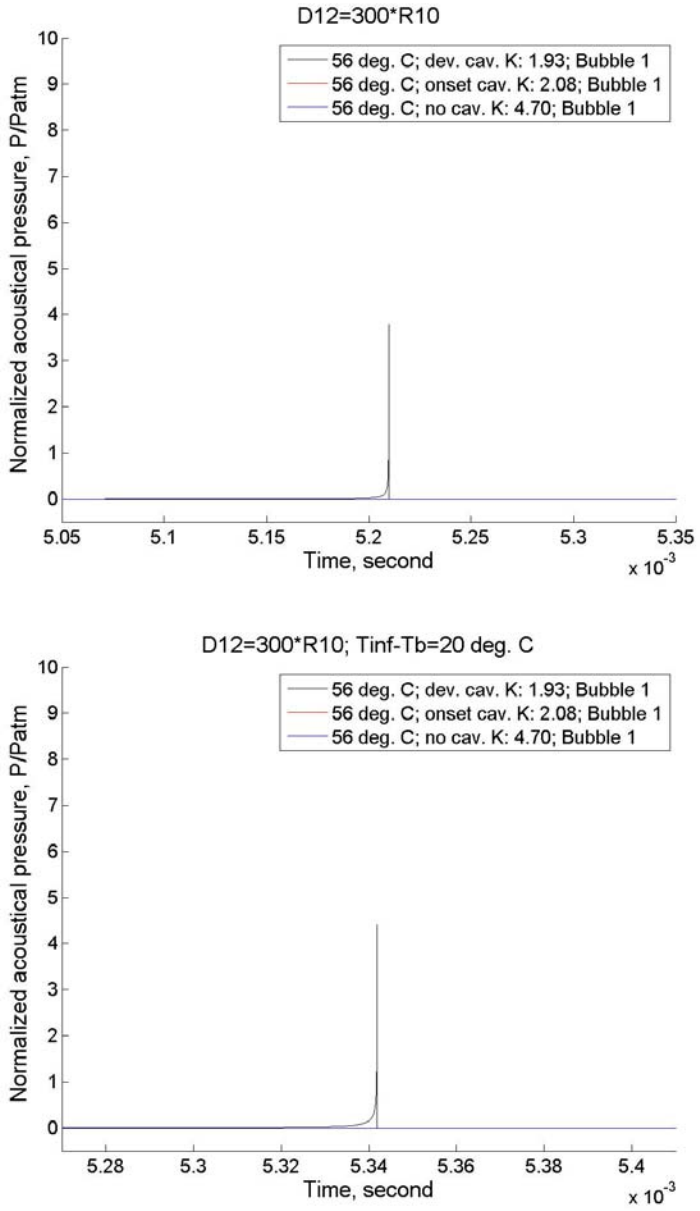

Fig. 4.14 (b) Comparison of pressure change with center-to-center distance D_{12} = 300xR10. Upper figure ($T_\infty - T_B = 0^\circ C$), lower figure ($T_\infty - T_B = 20^\circ C$).

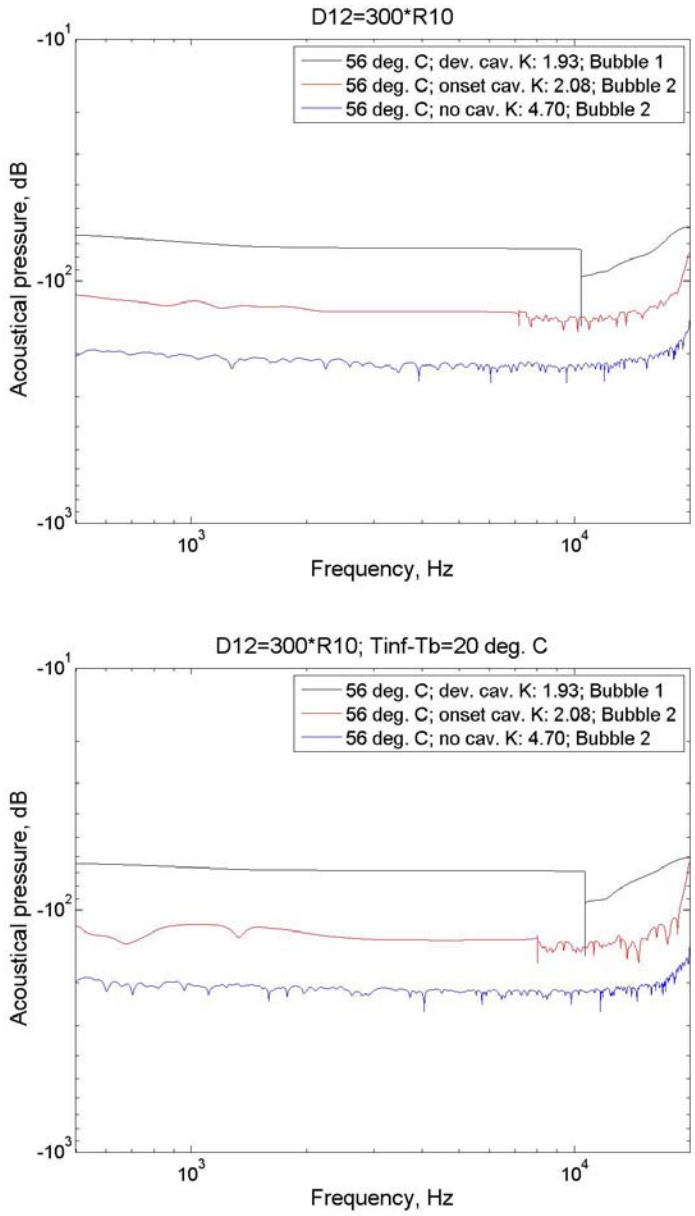

Fig. 4.14 (c) Comparison of acoustical pressure change with center-to-center distance D_{12}= 300xR10. Upper figure ($T_\infty - T_B = 0^\circ C$), lower figure ($T_\infty - T_B = 20^\circ C$).

4.4 Conclusion

Noise characteristics of sodium cavitation were investigated for a venturi with

inner diameter of 6.5 mm and length of 20 mm. The experiments were conducted at sodium stagnant pressures in the expansion tank in the range of 0.061-0.181 MPa-a and in temperatures range of 200°-400°C. The results were compared with water cavitation noise spectrum conducted with the same test section geometry. The major conclusions are summarized as follows:

1) Cavitation occurrence in sodium produced a noise in the range of 600 Hz to 20 kHz, while in water it increases for the whole frequency range. In sodium at developed cavitation condition, the noise intensity was relatively constant at around -50 dB which might be caused by the choking of the fluid. At 400°C, instabilities of the noise intensities were observed. These instabilities might be caused by the shedding process of cavitation bubbles that produce shock waves and disturb the flow conditions upstream.
2) The change of the stagnant pressure at the expansion tank did not affect the spectrum of the noise intensity at 200°-400°C during intermittent and developed cavitation.
3) Noise spectrum comparison with the water cavitation case showed that cavitation in water produced noise from low frequency up to 20 kHz. However, although both noise intensity spectrums in sodium and water cavitation cases were different in their shapes, but their noise intensities showed sharp increase at higher frequency region than at lower one. The increase of the noise spectrum at higher frequency region was more noticeable in case of sodium cavitation than in water cavitation. At develop cavitation, the noise spectrum increased at higher frequency region for both sodium and water. It indicated that the bubble behavior during developed cavitation stage for both sodium and water was similar.

4) Numerical calculation for bubble growth and collapse showed that the collapse process produced high pressure pulse. The intensity of the acoustical pressure was relatively flat from lower frequency up to about 10 kHz, and gradually increasing up to 20 kHz.

4.5 References

4-1 Bistafa, S. R., (1986), Noise Generated by Cavitation in Orifice-Plates with Some Gaseous Effects, International Symposium on Cavitation and Multiphase Flow Noise, pp. 41-52.

4-2 Sato, K., (1987), A Study of Cavitation Process by Means of Acoustic Pulse Measurement, International Symposium on Cavitation Research Facilities and Techniques, FED-Vol. 57, December, 13-18, pp. 115-121.

4-3 Frizell, K. W. and Cheng, J., (1987), Air Bubble Creation Noise, Cavitation and Multiphase Flow Forum, FED-Vol. 50, June 14-17, pp. 5-7.

4-4 Frizell, K. W., Cheng, J. and Arndt, R. E. A., (1987), Characteristics of Bubble Splitting Noise, Cavitation and Multiphase Flow Forum, FED-Vol. 50, June 14-17, pp. 38-40.

4-5 Zhuang, H. and Liu, K., (1988), An Experimental Study on Cavitation Noise on Headforms, Cavitation and Multiphase Flow Forum, FED-Vol. 64, July 24-28, pp. 68-70.

4-6 Kumar, S. and Brennen, C. E., (1991), Statistics of Noise Generated by Travelling Bubble Cavitation, Cavitation and Multiphase Flow Forum, FED-Vol. 109, June 23-27, pp. 55-61.

4-7 Arakeri, V. H. and Shanmuganathan, V., (1985), On the Evidence for the Effect of Bubble Interference on Cavitation Noise, Journal of Fluid Mechanics, Vol. 159, pp. 131-150.

4-8 Testud, P., Mussou, P., Hirschberg, A. and Auregan, Y., (2007), Noise Generated by Single-Hole and Multi-Hole Orifices in A Water Pipe, Journal of Fluid and Structures, Vol. 23, pp. 163-189.

4-9 Ardiansyah, T., Takahashi, M., Yoshizawa, Y., Nakagawa, M., Asaba, M. and Miura, K., (2010), The Onset of Cavitation and The Acoustic Noise Characteristics of Sodium Flow in a Venturi, Journal of Power and Energy Systems, Vol. 5, No. 1, pp. 33-44.

4-10 Sato, K. and Saito, Y., (2002), Unstable Cavitation Behaviour in a Circular-Cylindrical Orifice Flow, JSME International Journal Series B, Vol. 45, No. 3, pp. 638-645.

4-11 Huang, F., Takahashi, M. and Guo, L., (2005), Pressure Wave Propagation in Air-Water Bubbly and Slug Flow, Progress in Nuclear Energy, Vol. 47, No. 1-4, pp. 648-655.

4-12 Ida, Masato, (2009), Bubble-Bubble Interaction: A Potential Source of Cavitation Noise, Physical Review E 79, 016307.

4-13 Lofstedt, R., Barber, B. P., and Putterman, S. J., (1993), Toward a Hydrodynamic Theory of Sonoluminescence, Physical Fluids A 5, 2911.

4-14 Franc, Jean-Pierre, (2007), The Rayleigh-Plesset Equation: A Simple and Powerful Tool to Understand Various Aspects of Cavitation, Fluid Dynamics of Cavitation and Cavitating Turbopumps, CISM International Centre for Mechanical Sciences, Vol. 496, pp. 1-41.

CHAPTER 5

EROSION IN SODIUM CAVITATION

5.1 Introduction

Erosion caused by cavitation in sodium is one of the critical problems for developing Sodium-Cooled Fast Reactor (SFR) **[5-1]**. Damage of structural material caused by the collapse of cavitation bubbles in SFR may be expected in cases where the design requires a more compact reactor vessel and components, leading to higher sodium flow velocity. The cavitation might occur in local condition where the local pressure falls below the vapor pressure of the fluid due to high flow velocity. The damage of the structural material such as cracks or severe erosion leads to the failure of the reactor component. If the damage occurs in primary coolant pipes, the leak of reactor coolant from primary circuits could take place.

Previous researches have been conducted to study the damage of liquid metal cavitation and as a result, it has been known that cavitation causes damages on the surface of the materials **[5-2 to 5-9]**. For the study of liquid metal erosion itself, cavitation tests were conducted mostly by using vibratory apparatus since it can be done at relatively low cost, the liquid metals inventory can be easily operated and handled, and a large number of data can be obtained for various combinations of liquid metals and test materials for relatively short duration of time.

However, cavitation tests using the vibratory apparatus lack the information of the actual damage process in practical flowing condition, since most of the components that suffer from cavitation are operated in the flowing systems. The formation and collapse sites of cavitation bubbles in flowing systems are different from each other compared to vibratory apparatus where the formation and collapse sites are approximately the same. Also the growth and collapse process of the bubbles in flowing condition might be

difference since the shapes of the bubbles at flowing conditions are influenced by the flow. Moreover, it is known that pitting damages formed by cavitation in case of water system are influenced by the flow of the water **[5-10]**, and most of the data for cavitation damage in sodium are obtained for short period of time and by using vibratory apparatus that could enhance its collapse process. Therefore it is necessary to know in more detail the damage on the surface of the test section caused by cavitation in flowing sodium.

Therefore, in the present study the damage behavior is investigated in venturi channel made from 316 SS in order to understand the behavior of the damage in flowing sodium cavitation for long time period of 600 hours. The inner surfaces of the test section are observed using an optical micrograph and a scanning electron microscope (SEM) to investigate the erosion process.

5.2 Experiment

5.2.1 Experimental Apparatus

The experiment was conducted by using a sodium loop facility at Sukegawa Electric Co., Ltd. Argon gas was used as a cover gas pressure in the loop during the experiment. The downstream static pressure was measured by using a pressure transducer and the flow rate of sodium was measured by using an electromagnetic flow meter. The test section for this experiment is a venturi made from 316 SS with an inner diameter of 6.5 mm, an outer diameter of 21 mm, and a length of 20 mm. The detail explanation of this apparatus can be found in **Chapter 2.1** and **ref. [5-11]**.

5.2.2 Experimental Condition

The experimental conditions for sodium cavitation damage experiment are listed in **Table 5.1**. The physical and thermodynamic properties of sodium and the chemical compositions of 316 SS can be seen in **Tables 5.2** and **5.3**, respectively. The minimum Re number at outer diameter was around 56500 and at inner diameter was around 182600 indicating turbulent flow.

Table 5.1 Experimental conditions for cavitation erosion experiment.

Sodium temperature [°C]	200
Stagnant pressure at expansion tank [kPa]	105-110
Flow rate [L/min]	27-28
Cavitation coefficient, *K* [-]	0.59-0.51
Experimental time [h]	600

Table 5.2 Physical and thermodynamic properties of sodium **[5-12]**.

Melting point [°C]	98
Boiling point [°C]	883
Vapor pressure at 200°C [MPa]	2.20×10^{-8}
Liquid density at 200°C [$kg.m^{-3}$]	903

Table 5.3 Compositions of 316 SS.

Material	%
Fe	Balance
C	0.04-0.1
Mn	0.04-0.1
Si	0.0-0.75
P	0.0-0.045
S	0.0-0.03
Cr	16.0-18.0
Mo	2.0-3.0
Ni	10.0-14.0

Table 5.4 Mechanical properties of 316 SS.

Tensile strength [MPa]	515
Yield strength [MPa]	205
Hardness [HB]	217

5.3 Results and Discussion

In order to see the inner surface condition of the venturi channel before cavitation test, a hole with the same diameter of 6.5 mm was made in a 316 SS rod by the same machining method as that for the fabrication of the venturi channel as shown in **Fig. 5.1 (a)**. The cylinder was then cut into half in the axial direction, and the inner surface of the cylinder was observed by using SEM as shown in **Fig. 5.1 (b)**. Under SEM observation, clear lines made by machining were observed on the inner surface, and no indication of pits or erosion can be observed.

In this experiment, the venturi channel was tested in developed cavitation condition using sodium for 600 hours. After experiment, ethanol was used to wash the remaining sodium that might adhere on the surface by the following reaction

$2CH_3CH_2OH + 2Na \rightarrow 2CH_3CH_2ONa + H_2$

The solution was left to dry and leave the white solid sodium ethoxide that can be cleaned by water easily. This process was repeated several times to ensure that there is no sodium adhere on the surface of the test section. After that the test section was then cut into half in the horizontal direction as shown in **Fig. 5.1 (c)**. The cut part of the test section was polished smoothly using polisher from grit size of 120 and gradually increasing to grit size of 2400 with water as grease. Next, velvet polisher was used until the surface of the material became a mirror like surface to observe the damage part from its cross section. From visual observation using naked eyes on the inner surface of the cross section, there were not found any eroded parts appreciably. However, color degradation from white-colored surface to brown-colored one was observed on inner surface in the downstream part, which suggests the occurrence of erosion. Since cavitation bubbles are formed at the venturi part, transported downstream through the venturi part, and collapse in the downstream part due to the recovery of sodium static pressure.

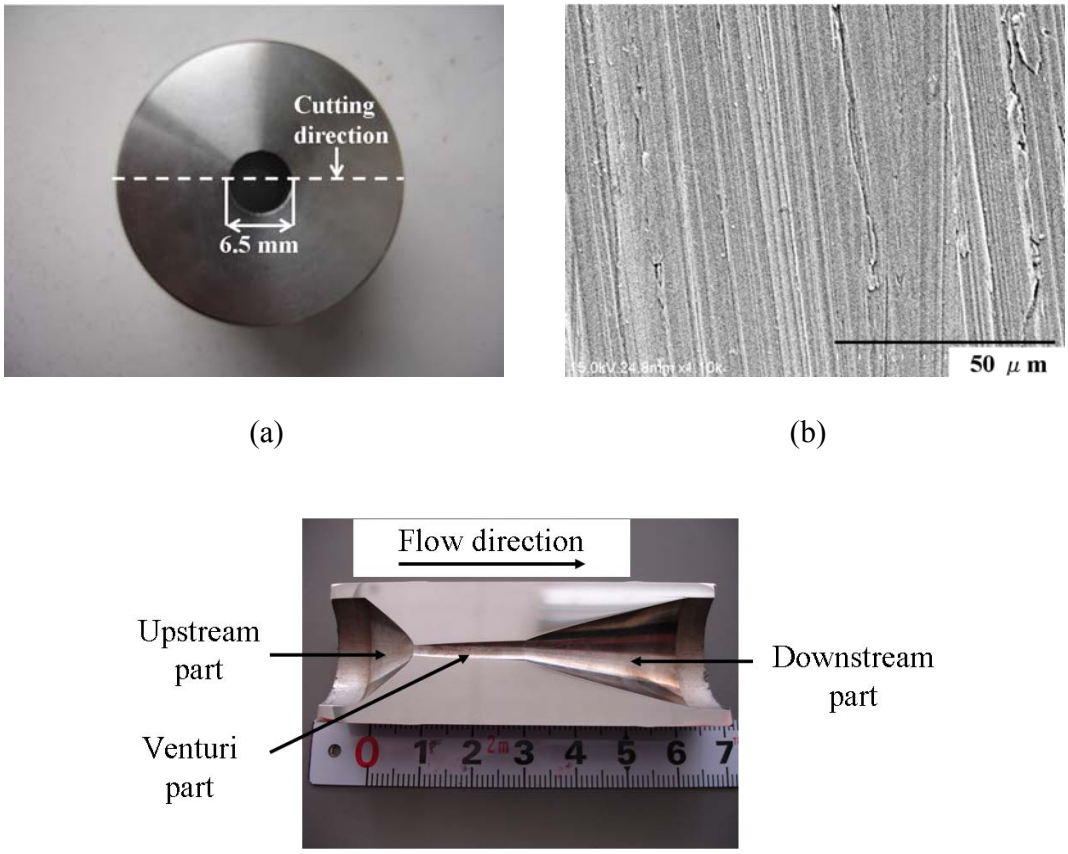

Fig. 5.1 (a) A 316 SS cylinder made with the same machining method as the venturi channel used for cavitation damage experiment; **(b)** SEM of the inner surface of **Fig. 5.1 (a)**; and **(c)** Venturi channel cut into half after cavitation experiment for 600 hours.

In order to observe the inner surface of the test section more clearly, an optical microscope was used and the result is shown in **Fig. 5.2**. The upper picture of **Fig. 5.2** shows the upstream part of the venturi where cavitation bubbles are formed due to the decrease in static pressure below the vapor pressure of sodium at 200°C because of the acceleration of sodium flow. This acceleration occurs when sodium travels from the

upstream part to the inside of the venturi region. The figure shows that the inner surface at the upstream part of the venturi reveals relatively smooth surface. No clear micro pits are observed in this region. The lower picture of **Fig. 5.2** shows the downstream part of the venturi. The surface shows some pitting damages at around 100 μm from the throat outlet. These damages are caused by the collapse of cavitation bubbles when travelling out from the venturi outlet. The collapse produces shock waves and micro jets which impinge on the surface of the test section, hence creating some observable micro pits.

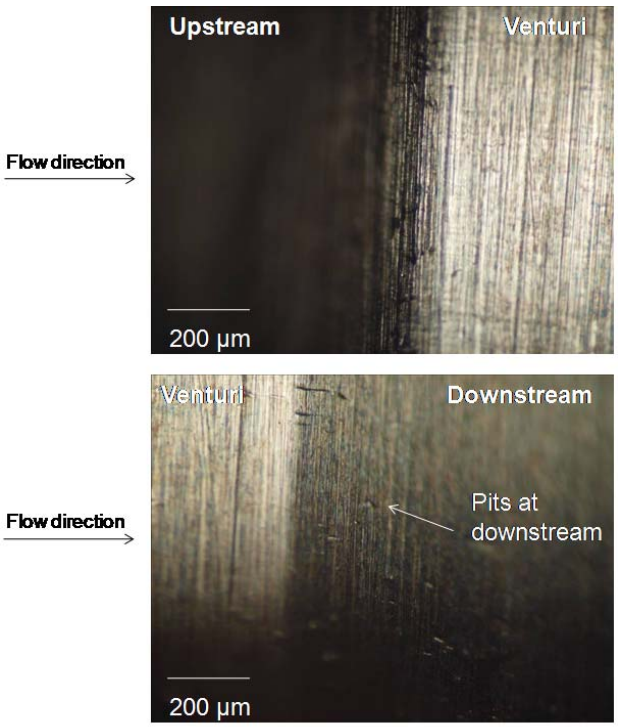

Fig. 5.2 Photograph of the test section surface at upstream (upper picture) and downstream (lower picture) parts of the venturi channel.

SEM was utilized to observe the damage part more clearly such as the size, distribution and shape of each pit. However, since the sample holder of the SEM machine has limited size, the test section was cut into seven samples with 5 and 10 mm in length (**Fig. 5.3**) so that the surface of each sample could be observed. The specimens were washed again by ethanol and water before observed by using SEM. Therefore the possibility that oil attach on the surface was impossible. Because of the curvature of the inner surface of the test section, observation on the surface of the test section cannot be done over the radial direction (from bottom to top). Therefore, only around the axis part of the inner surface of the test section on the axial direction was observed (from left to right). The surface from samples No. 4 until No. 7 was observed around the axis part and the SEM pictures were taken beginning from the left part and step-by-step moving to the right. Each picture was observed and the numbers and shapes of pits were counted to get the total number of pits. The total number of pits then divided by the number of pictures taken in each samples to get the average number of pits.

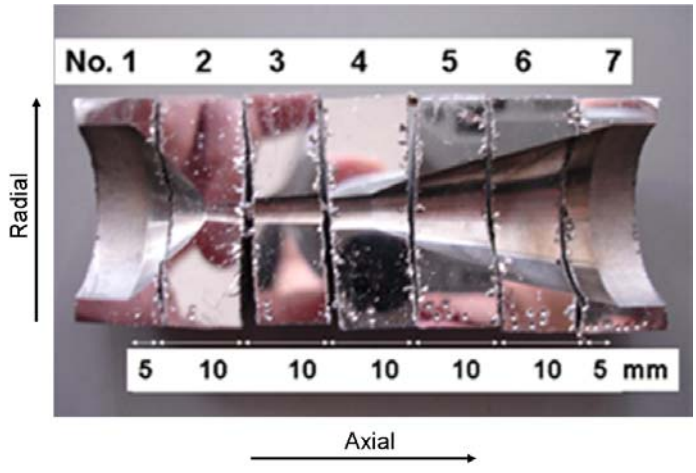

Fig. 5.3 Venturi channel cut into seven samples.

From the SEM observation on the surface, the number of pits on the surface of each sample was counted with emphasis on samples No. 4 to No. 7 (downstream part of the test section) where cavitation bubbles collapse due to high static pressure of the sodium on these regions and expected that at these parts the erosion will be higher. To ensure pits were formed, the observation of the surface using backscattered electron signal generated at low angles from the specimen was also performed. The backscattered electron signal at low angles is very sensitive to compositional information, therefore differences between the compositions can be observed. The backscattered electron signal is generated from the electron beams that are reflected from the sample/specimen by elastic scattering. The intensity of the signal depends on the atomic number of the specimen. Therefore information about different elements in the specimen can be obtained. The results show that there were no differences in color as shown in **Fig. 5.5** below. It means that the materials have the same compositions and indicate that pits were formed due to cavitation. If the compositions were different than different colors could be seen on the **Fig. 5.5**. Observation on the surface of the specimen was also conducted using laser microscope (Keyence VK-8500). The typical 2D and 3D surface analysis clearly shows a hole with depth of around 25 μm as shown in **Figs. 5.6** and **5.7**. This hole clearly indicates that pit is created due to cavitation. **Figure 5.8** shows the average number of pits on the surface of samples No. 4 to 7. It was found that the average numbers of pits were high on the surface of samples No. 6 and 7, which suggested that most of the bubbles collapsed in these regions. This was possible since the static pressure of the sodium in that region was higher than at regions of samples No. 4 and 5. Cavitation

bubbles would have more time to travel downstream because the pressure difference was not large enough to make the bubbles to collapse; hence the energy to produce a micro pit was not so large. Therefore, most of the bubbles might collapse at region of samples No. 6 and 7. The existence of pits on the surface of samples No. 4 and 5 suggests that some small number of bubbles also collapse there. Smaller bubbles might collapse easily on the surface of samples No. 4 and 5, while larger bubbles require larger pressure difference to collapse. Therefore, the collapse of larger bubbles can be achieved at region of samples No. 6 and 7. Figure 3.4 also shows that the formation and collapse sites of cavitation bubbles are not same, but rather downstream of the venturi outlet resulting from the flow.

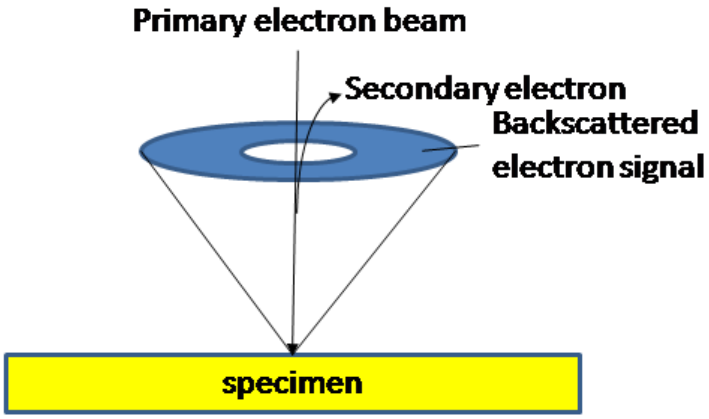

Fig. 5.4 Different electron signals generated by SEM.

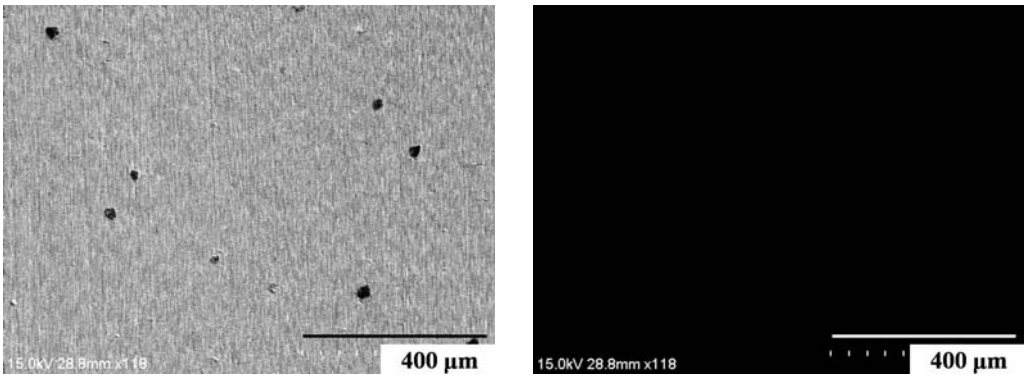

(a) (b)

Fig. 5.5 a) Pits distribution at sample No. 6 (~7700µm from left), and **b)** its corresponding backscattered electron signal.

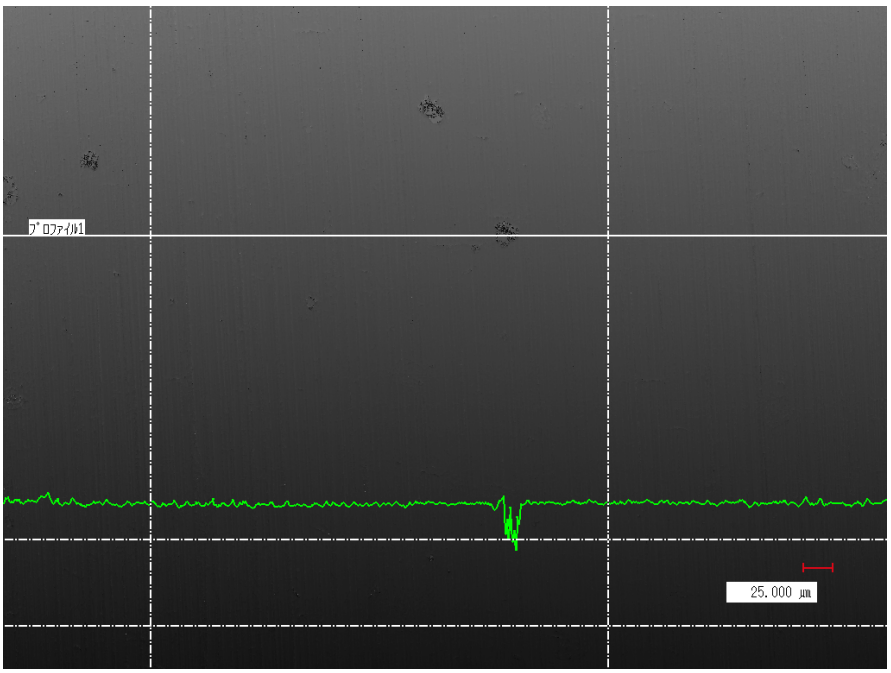

Fig. 5.6 2D surface analysis of sample no. 7 (~600 µm from left).

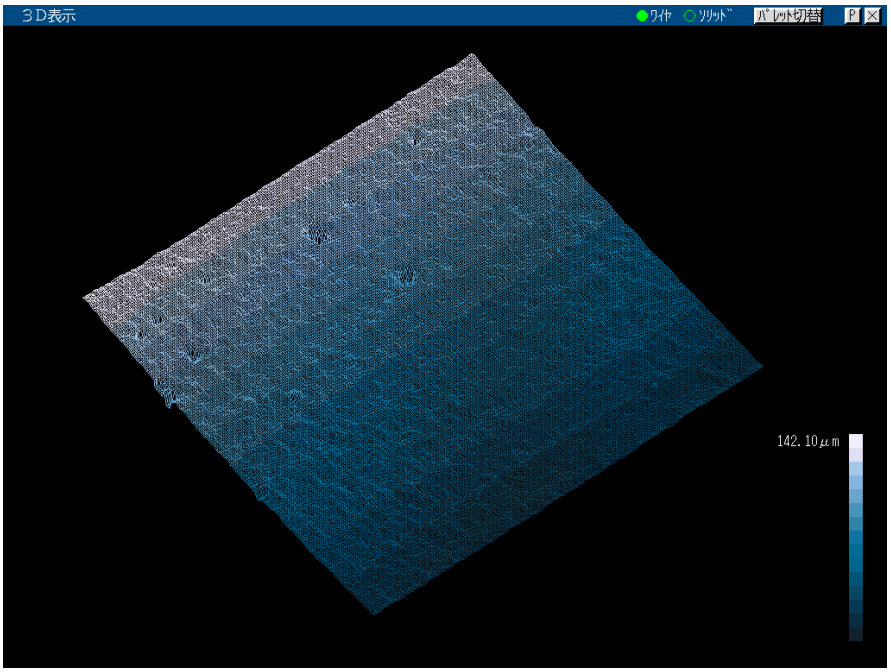

Fig. 5.7 3D surface analysis of sample no. 7 (~600 μm from left).

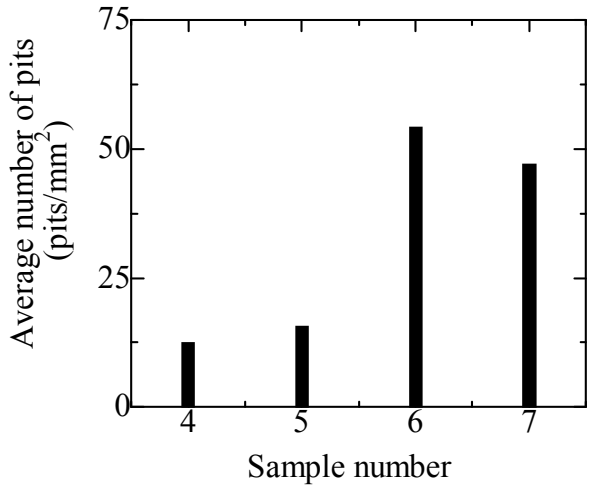

Fig. 5.8 Average number of pits for each sample number.

Figure 5.9 shows the distribution of the number of the pits with its diameter for samples No. 4 to 7. It was found that most of the pits formed on the surface of the test section had diameter of around 25 μm indicated by some clearly observable peaks for samples No. 4 to 7. Samples No. 6 and 7 had larger number of pits with diameter of around 25 μm compared to others. Pits with smaller diameter might be produced by the low energy from cavitation bubbles collapse, while those with larger diameter might be produced by larger energy since the collapse energy from a cavitation bubble has linear relationship with a pit being formed on the surface of the material **[5-13]**. For instance, in case of sample No. 6, some pits with diameter larger than 25 μm were also observed with the largest diameter of around 110 μm, which indicated intense collapse of cavitation bubbles at this region which formed a larger pit diameter.

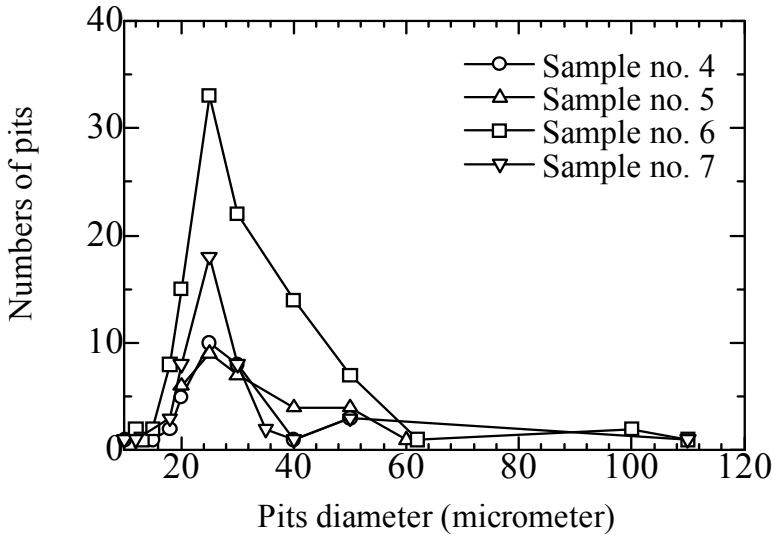

Fig.5.9 Average number of pits for each sample versus pits diameter.

Figures 5.10 to 5.13 show the distributions of the pits and the enlarge view of the pits from the surfaces of samples No. 4 to No. 7 that are located downstream of the venturi channel. Briefly observing the surfaces of samples No. 4 to No. 7 it can be seen that pits distributions on samples No. 4 and 5 are scarce and lower than distributions on samples No. 6 and 7 where a lot of erosions can be observed. **Figure 5.12** shows the SEM photographs of the inner surface on sample No. 6. As shown in **Fig. 5.12 (a)**, pits are not distributed uniformly on the surface. Some of the pits have large diameters but others have smaller diameters. The difference in the diameter of the pits might be caused by the difference of the energy absorbed by the material to form a pit resulting from the collapse of a cavitation bubble. Since the collapse of cavitation bubbles occurred randomly, therefore it was expected statistically that a pit was formed by a single collapse of cavitation bubble **[5-14]**. However, larger pits might be produced by the collapsing of some small cavitation bubbles at the same local place or by larger bubbles although the probability was very small. Therefore it can be seen in **Fig. 5.9** above that the number of pits with diameter larger than 25 μm is decreasing. The pits that were observed on the surface of sample No. 4 to No. 7 show irregular shapes rather than round ones. This might indicate the influence of the flow that changes the shapes of the collapse bubbles from spherical to non-spherical.

Meanwhile, **Fig. 5.10 (b)** to **5.13 (b)** show an enlarged view of a pit with a diameter of around 25-40 μm. It seems that the ductile surface is deformed to a pit by pressure pulse. Based on the differences of color from SEM, the surface plots of the pits can be predicted qualitatively and are shown from **Figs. 5.10 (c)** to **5.13 (c)**. The qualitative surface plot shows rough surfaces with holes that indicate the formation of

pits induced by sodium cavitation. From the surface photograph using SEM, the depth of the pit could not be determined due to the curvature of the test section. Also because the pits are formed randomly, therefore observation of the pits' depth at the sample cross-section is difficult because it is hard to match the cutting part with the pitting parts caused by cavitation in the sodium flow.

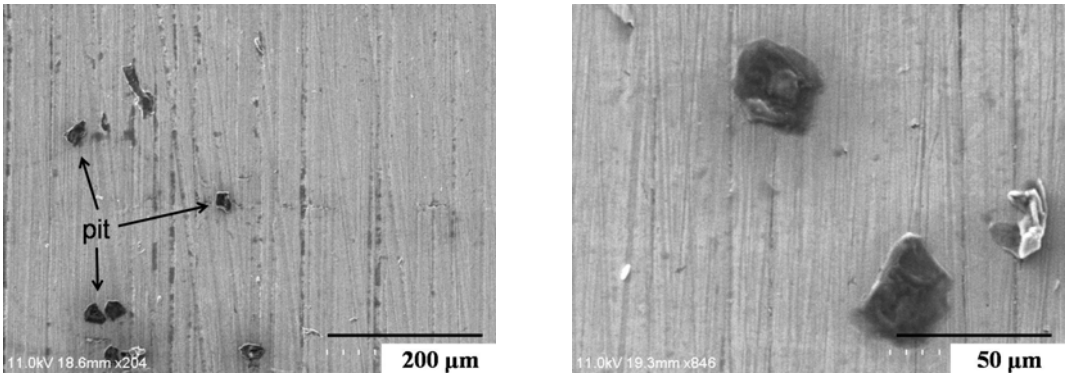

(a) Pits distribution (~ 2500 µm from left) (b) Enlarged view (~625 µm from left)

Fig. 5.10 SEM of inner surface on sample No. 4.

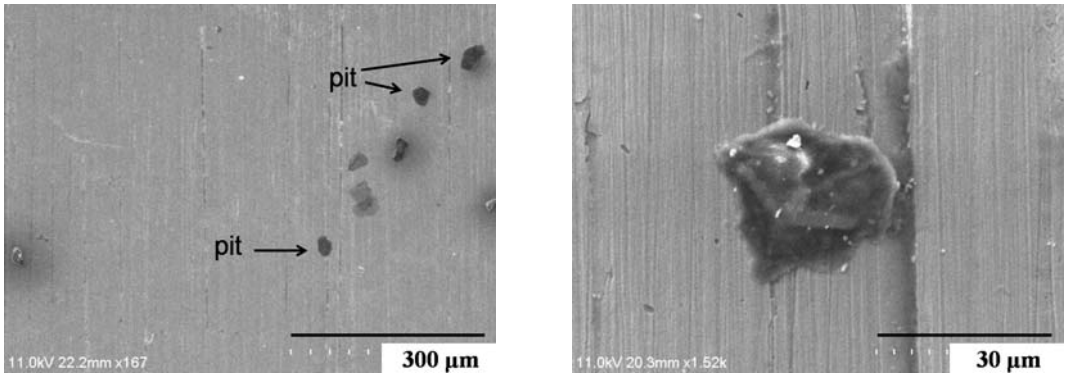

(a) Pits distribution (~ 4285 µm from left) (b) Enlarged view (~1428 µm from left)

Fig. 5.11 SEM of inner surface on sample No. 5.

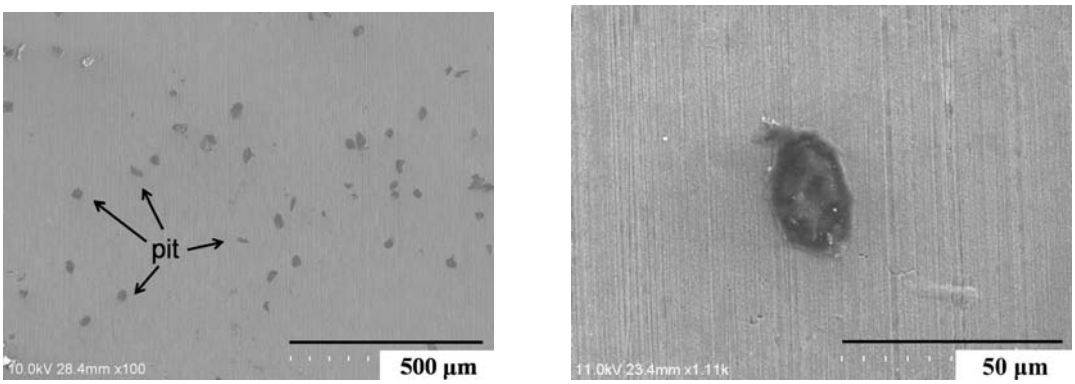

(a) Pits distribution (~ 3750 µm from left) (b) Enlarged view (~9300 µm from left)

Fig. 5.12 SEM of inner surface on sample No. 6.

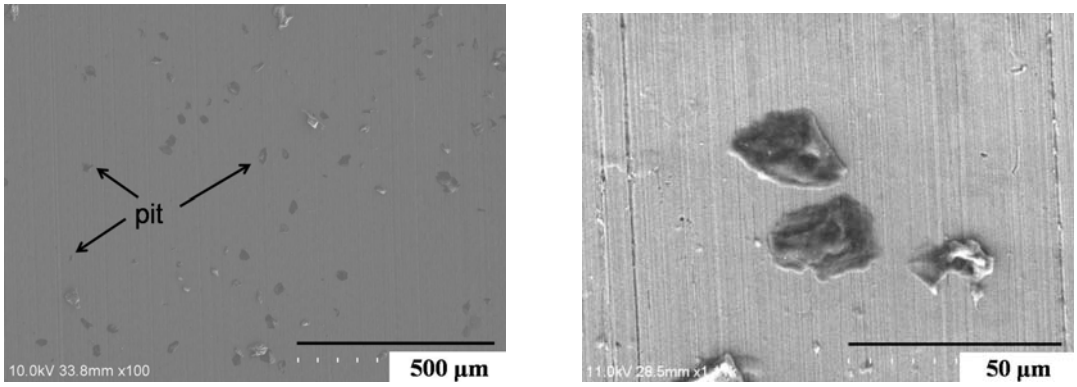

(a) Pits distribution (~ 2500 µm from left) (b) Enlarged view (~3823 µm from left)

Fig. 5.13 SEM of inner surface on sample No. 7.

Besides micro pits which were formed on the inner surface of the test section, some micro cracks were also observed on the inner surface of samples No. 2, 3 and 4 with the length of around 100 µm as shown in **Fig. 5.13**. These micro cracks might be caused by the cyclic process that occurred on the test section due to the formation and collapse of the bubbles at the test section. It was known that the formation and collapse of cavitation bubbles in venturi channel occurred with certain frequency **[5-15]**. When this

condition was maintained for longer time scale, material became fatigue and small cracks might grow slowly into larger ones. If these cracks cannot be prevented well, material can be damaged further which could cause an accident during the operation of a sodium-cooled fast reactor. And this could stop the operation of reactor for a longer time.

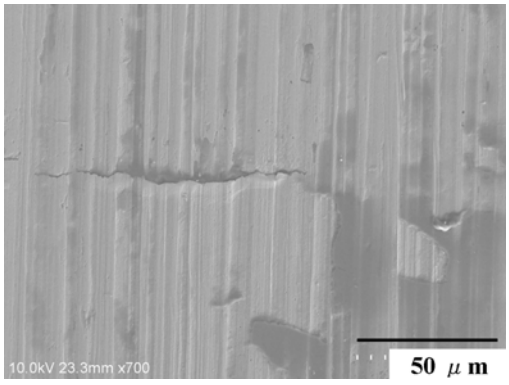

(a) Sample No. 2 (~8600 μm from left)

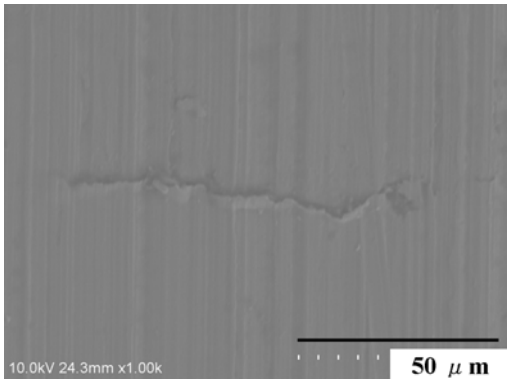

(b) Sample No. 3 (~6000 μm from left)

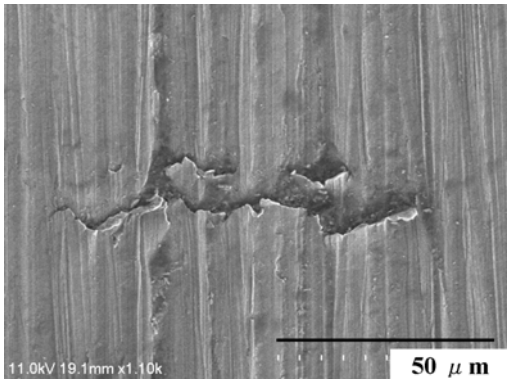

(c) Sample No. 4 (~7500 μm from left)

Fig. 5.14 SEM observation of micro cracks on inner surface of the test section.

There are a lot of important factors that can influence erosion in sodium such as hardness of the material, liquid density, sound velocity, liquid pressure and bubble wall distance. The hardness the material, the more resistant it is from cavitation erosion.

Liquid density, sound velocity, liquid pressure and bubble distance from the wall significantly influence the generation of impact pressure when bubble collapse theoretically **[5-16]**. Higher liquid density, sound velocity and liquid pressure will create higher impact pressure and more erosion.

To observe the mechanism of cavitation bubbles collapse, a high-speed camera was used. Since it is difficult to observe the collapse process in sodium, experiment in water to simulate bubble collapse in sodium was conducted at room temperature. The experiment was conducted at water temperature of 34.5°C, *K*: 0.78 (developed cavitation). The high-speed camera (Ultranac FS-501) during the experiment was operated at frame rate of 50000 fps and flashing lamp (Nissin Electronic LH-SA2H) was operated at 50 Joules/flash, exposure time 180 μs. From **Fig. 5.15** it is shown that although the high-speed camera frame was very rapid, however the collapse of the bubble cannot be observed clearly. It indicates that the collapse speed at developed cavitation was very fast. The rapid collapse of cavitation bubbles might be caused by the influence of pressure waves from the neighboring bubbles. The pressure waves could add more external pressure during the collapse process that increases the bubble wall velocity as shown in **Figure 5.16**. Therefore the processes of cavitation bubbles collapse in sodium are assumed based on references of bubbles collapse near wall in water. **Figure 5.17** shows the schematic process of the pits and micro cracks formation. At first the cavitation bubbles generated at the throat of the venturi channel were transported to downstream because of the sodium flow. Static pressure at downstream of the venturi channel was recovered again at downstream since the dynamic pressure was reduced. Because there was an increase of the static pressure at downstream, bubbles could collapse very

intensely. Based on the reference from Tomita and Shima **[5-17]**, the collapse of the cavitation bubbles was not spherical because of the wall effect. This un-spherical collapse of bubble will produce micro jet with higher velocity normal to the wall. Analytical estimation of the micro jet velocity by **[5-18]** is 100 m/s based on the measurement from dynamic pressure **[5-19]**. The micro jet velocity lies in the range of 100-200 m/s as measured by **[5-20 to 5-24]**. The impact pressure of the micro jet on the wall can be estimated by using the water hammer formula of Joukowski and Allievi **[5-16]**:

$$\Delta P = \rho c V_j \quad \text{.....(5-1)}$$

Where ΔP is the normal pressure to the wall, ρ is the fluid density, c is the sound velocity in fluid and V_j is the jet velocity. For sodium at 200°C, jet velocity of 100-200 m/s and sound velocity of 2462.25 m/s the pressure is estimated to be 222-444 MPa. This value is higher than the yield strength of 316 SS that has the value of 205 MPa. Therefore, the formation of micro pits on the surface the venturi channel is possible because of the plastic deformation. This created micro jet from cavitation bubbles collapse could hit the surface of the material and creating some observable micro pits during the experiment for 600 hours. In sodium, the micro jet velocity might be very large because there is no damping by the gas when the bubbles collapse due to vaporous cavitation process. The collapse of the bubbles will create vibrations also on the material because of the shock wave. These vibrations can create micro cracks due to material fatigue, and the micro cracks can go first from the pits as the weakest point in material surface. Analytical calculation of micro jet velocity **[5-25]** shows that the effects of surface tension and initial bubble radius on micro jet velocity are small than liquid pressure and stand-off

parameter observation (bubble distance from the wall divided by the initial bubble radius) **[5-26]**.

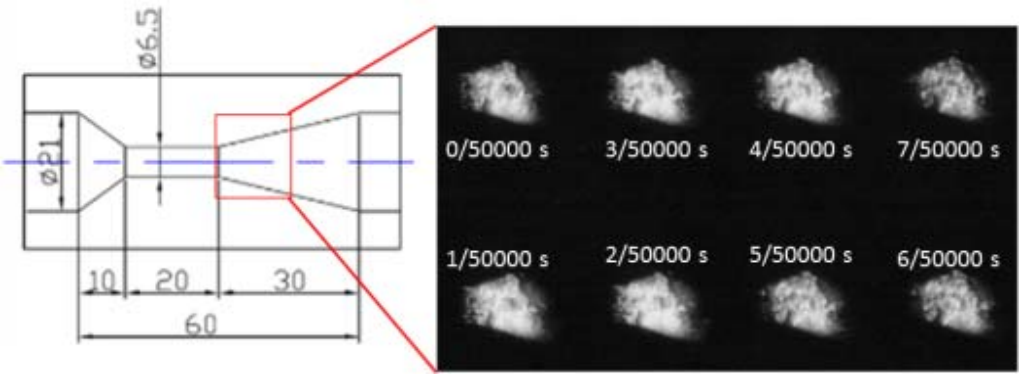

Fig. 5.15 Collapse process in water cavitation (*K*: 0.78 (developed cavitation); T: 34.5°C). Frame speed of high-speed camera: 50000 fps, flashing lamp energy: 50 J, exposure time: 180 μs.

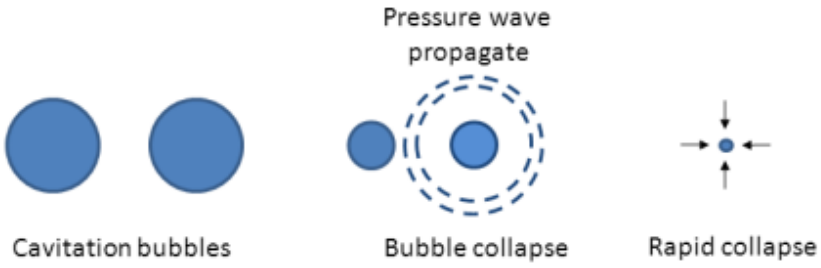

Fig. 5.16 Schematic of rapid bubble collapse at downstream of venturi channel.

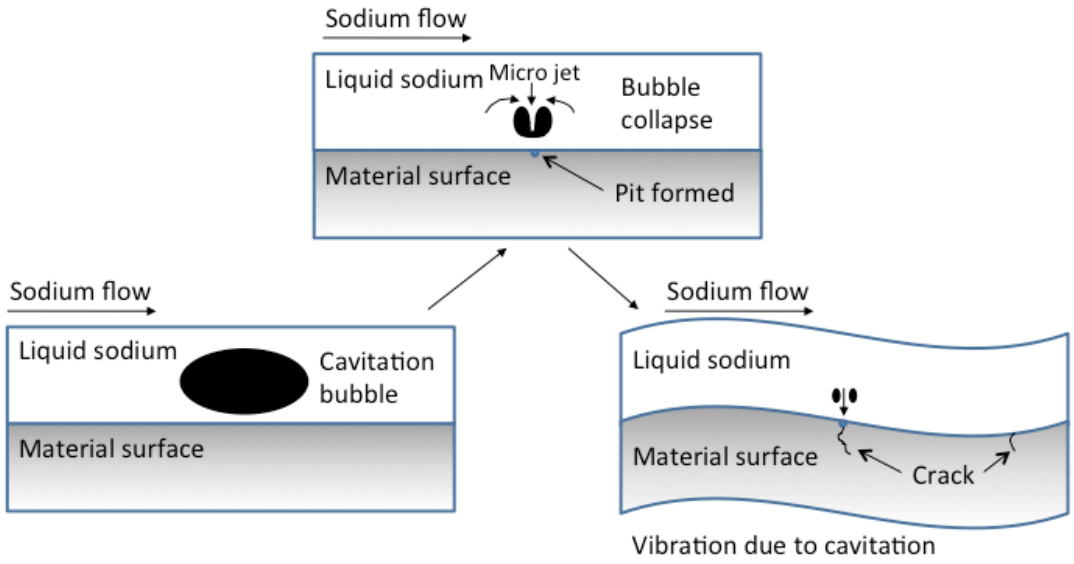

Fig. 5.17 Schematic of pits and cracks formation due to cavitation.

5.4 Conclusion

Cavitation erosion experiment has been conducted for flowing sodium in venturi channel made from 316 SS. The following conclusions are obtained:

1) Cavitation created damage on the surface of the test section in the form of irregular pits due to eroded surface and micro cracks.

2) Most of the pits formed on the surface of the test section occurred on sample No. 6 that was further downstream of the venturi outlet. This indicated that the formation and collapse sites of cavitation bubbles were not the same and influenced by the sodium flow. These pits had diameter of around 25 μm. Some pits with diameter larger than 25 μm were also observed with the largest diameter of around 110 μm, which suggested intense collapse of cavitation bubbles in this region.

3) The collapse of cavitation bubbles at downstream produced micro pits with various

diameter. The distribution of the pits showed that pits with smaller diameters have higher number density on the surface of the material than with larger diameters. This suggested that the bubbles collapse pressure was more intense at lower pressure than at higher pressure.

4) Micro cracks were observed on the inner surface of the venturi channel which might be caused by the cyclic process of the formation and collapse of the cavitation bubbles at the venturi channel.

5.5 References

5-1 Konomura, M. and Ichimaya, M., (2007), Design Challenges for Sodium Cooled Fast Reactors, Journal of Nuclear Materials, Vol. 371, pp. 250-569.

5-2 Young, S. G. and Johnston, J. R., (1970), Effect of Temperature and Pressure on Cavitation Damage in Sodium, Characterization and Determination of Erosion Resistance, ASTM STP 474, American Society of Testing and Materials, pp. 67-108.

5-3 Preiser, H. S., Thiruvengadam, A. and Couchman III, C. E., (1964), Cavitation Damage in Liquid Sodium, NASA CR-54071.

5-4 Thiruvengadam, A., Preiser, H. S. and Rudy, S. L., (1965), Cavitation Damage in Liquid Metals, NASA CR-54391.

5-5 Thiruvengadam, A. and Preiser, H. S., (1965), Cavitation Damage in Liquid Metals, NASA CR-72035.

5-6 Young, S. G. and Johnston, J. R., (1967), Effect of Cover Gas Pressures Up To 4 Atmospheres on Accelerated Cavitation Damage in Sodium, NASA TMX-61065.

5-7 Young, S. G. and Johnston, J. R., (1968), Effect of Cover Gas Pressures on Accelerated Cavitation Damage, NASA TMX-52414.

5-8 Smith, P. G., DeVan, J. H. and Grindell, A. G., (1963), Cavitation Damage to Centrifugal Pump Impellers during Operation with Liquid Metals and Molten Salt at 1050-1400 F. Transaction of the ASME Series D, Journal of Basic Engineering, Vol. 85, pp. 329-337.

5-9 Young, S. G. and Johnston, J. R., (1967), Accelerated Cavitation Damage of Steels and Superalloys in Sodium and Mercury, Erosion by Cavitation or Impingements, ASTM STP 408, American Society of Testing and Materials, pp. 186-219.

5-10 Robinson, M. J. and Hammitt, F. G., (1967), Detailed Damage Characteristics in a Cavitating Venturi, Transaction of the ASME Series D, Journal of Basic Engineering, Vol. 89, pp. 161-173.

5-11 Ardiansyah, T., Takahashi, M., Yoshizawa, Y., Nakagawa, M., Asaba, M. and Miura, K., (2010), The Onset of Cavitation and The Acoustic Noise Characteristics of Sodium Flow in a Venturi, submitted to Special Issue on 18th International Conference on Nuclear Engineering, Journal of Power and Energy Systems.

5-12 Fink, J. K. and Leibowitz, L., (1995), Thermodynamic and Transport Properties of Sodium Liquid and Vapor, ANL/RE-95/2.

5-13 Okada, T., Iwai, Y., Hattori, S. and Tanimura, N., (1995), Relation Between Impact Load and The Damage Produced by Cavitation Bubble Collapse, Wear, Vol. 184, pp. 231-239.

5-14 Hammitt, F. G., (1963), Observations of Cavitation Damage in a Flowing System, Transaction of the ASME Series D, Journal of Basic Engineering, Vol. 85, pp. 347-359.

5-15 Niiyama, K., Nozawa, M., Ohira, K. and Oike, M., (2008), Cavitation Instability in Subcooled Liquid Nitrogen Flows, Journal of Fluid Science and Technology, Vol. 3, No. 4, pp. 500-511.

5-16 Franck, J. P. and Michel, J.M., (2005), Fundamentals of Cavitation, Kluwer Academic Publishers.

5-17 Tomita, Y. and Shima, A., (1990), High Speed Photographic Observations of Laser-Induced Cavitation Bubbles in Water, Acustica, 71, No. 3, pp. 161-171.

5-18 Zhong, P. and Chuong, C. J., (1993), Propagation of Shock Waves in Elastic Solids Caused by the Impact of Cavitation Microjets: Part I. Theoretical Formulation, Journal of the Acoustical Society of America, Vol. 94(1), pp. 19-28.

5-19 Rochester, M. C. and Brunton, J. H., (1974), in Proceedings of the 4th International Conference on Rain Erosion and Related Phenomena, Vol. I, edited by A. A. Fyall and R. B. King, pp. 371.

5-20 Benjamin, T. B. and Ellis, A. T., (1966), The Collapse of Cavitation Bubbles and the Pressure Thereby Produced Against Solid Boundaries, Philosophical Transaction of the Royal Society of London A, Vol. 260, pp. 221-240.

5-21 Gibson, D. C., (1968), Cavitation Adjacent to Plane Boundaries, In Proceeding 3rd Australasian Conference on Hydraulics and Fluid Mechanics.

5-22 Lauterborn, W., (1974), Kavitation durch Laserlicht, Acustica, Vol. 31, pp. 51-58.

5-23 Shima, A., Takayama, K., Tomita, Y. and Miura, N., (1981), An Experimental Study

on Effects of a Solid Wall on the Motion of Bubbles and Shock Waves in Bubble Collapse, Acustica, Vol. 48, pp. 293-301.

5-24 Vogel, A., Lauterborn, W. and Timm, R., (1989), Optical and Acoustic Investigations of the Dynamics of Laser-Produced Cavitation Bubbles Near a Solid Boundary, Journal of Fluid Mechanics, Vol. 206, pp. 299-338.

5-25 Samiei, E., Shams, M., Mahdi, M., Ebrahimi, R. and Ahmadi, G., (2010), Numerical Study on Surface Tension Effects on Cavitation Bubble Collapse in Spherical Acoustic and Nonspherical Rayleigh Collapse, 7th ICMF, pp. 1-9.

5-26 Philipp, A. and Lauterborn, W., (1998), Cavitation Erosion by Single Laser-Produced Bubbles, Journal of Fluid Mechanics, Vol. 361, Issue 01, pp. 75-116.

CHAPTER 6

CONCLUSIONS

SFR is one of the proposed Generation-IV nuclear reactors. However in the development of SFR cavitation is regarded as one of the most important aspects to be solved because of the compact design. To simulate cavitation in sodium, most of the researches were conducted in water instead of sodium. This results in the very limited data in sodium cavitation as compared to water cavitation. Also, cavitation experiment in water lacks the information of the actual cavitation process in sodium because of the different properties between sodium and water. This lack of information can be a major obstacle in developing SFR in the future. Therefore cavitation experiment in sodium is very important in order to understand the differences between sodium and water cavitation. The objective of this study is to investigate cavitation characteristics using sodium to get the actual cavitation process. The results are compared with water cavitation case to make clear the differences. From the experiments conducted in this study and the results presented from **Chapter 3**, **Chapter 4** and **Chapter 5**, the overall conclusions are summarized below:

a) For the simulation of sodium cavitation using water, the concentration of gas is very important to control. Because in sodium the gas content is not so high and vaporous cavitation could occur. However in case of water the gas content is high enough, therefore gaseous cavitation could occur. In sodium case due to vaporous cavitation, the onset cavitation coefficient K is around 1, while in water due to gaseous cavitation the onset cavitation coefficient K is higher than 1.
b) For the detection of sodium cavitation acoustic noise, it is important to differentiate the noise spectrum especially at high frequency region. In case of sodium cavitation the noise increases at high frequency region (from around 2 kHz up to 20 kHz)

probably caused by the more dominant vaporous cavitation process. While in water the noise increases not only at high frequency but also at low frequency region (from low frequency up to 20 kHz) that probably caused by gaseous cavitation.

c) In sodium erosion experiment, it is found that erosion in the form of micro pits and micro cracks occurred even for 600 hours in developed cavitation under flowing condition. Most of the pits created have diameter of around 25 μm.

   From the results, to simulate sodium cavitation using water, controlling the gas concentration is very important to have the similar characteristics of cavitation (onset and acoustic noise). While in erosion, the collapse of vaporous cavitation might create more erosion than gaseous cavitation because the bubbles directly collapse without damping.

For the future development of SFR, these results show that it is important to choose material with higher strength that is more resistant to erosion at some parts where the possibility of cavitation occurrence is high. Also controlling the coolant velocity and pressure in SFR is important to prevent cavitation. Lower velocity and higher pressure than atmospheric condition could suppress cavitation.

APPENDIX

Characteristics of Measurement Equipment

Sensor characteristics for sodium cavitation.

Model	Ono Sokki NP-2710	Maximum shock resistance	98,000 m/s^2
Structure	Shear type	Operating range	−70 to+260°C
Sensitivity	0.31 pC/(m/s^2)±10%	Insulation resistance	At least 1000 MΩ
Capacitance	Approx. 340 pF	Weight	2 g
Resonance frequency	Approx. 50kHz	Ground/insulation	Case ground
Frequency response range*	fc to 10 kHz±5% fc to 20 kHz±3dB	Case material	Titanium
Transverse sensitivity	Within 5%	Outer dimension	7.9 Hex x 8.4 H
Maximum allowable acceleration	22,600 m/s^2	Connector	5-44 coaxial right angle

*The fc depends on the time constant with respect to the charge amplifier, $fc=1/2\ \pi RC$

Characteristics of pressure transducer and diaphragm flange.

Specification (pressure gauge)	
Model	Ashcroft GC51
Accuracy	±0.25% FS (Full scale)
Stability	±0.25% FS/year
Response time	30 msec
Output resolution	0.1% FS
Zero offset	≤±0.1% FS/year
Standard ranges (compound)	-15 to 50 psi
Standard ranges (gauge)	0-7500 psi
Temperature limit (operating)	-10 to 60°C
Temperature effects (-10 to 60°C)	±0.2% FS
Output signal	4-20 mA (2 wire)
Supply voltage	12-32 Vdc
Specification (diaphragm)	
Diameter	110 mm
Lower flange material	316L SS
Upper flange material	316 SS

Characteristics of charge amplifier.

Model	TEAC SA-630
Input	BNC Connector, Switched Charge Type or IEPE Type
Maximum Input	100000pC (charge); ±10V (voltage)
Current Sources	0.5mA, 3mA
Sensitivity Setting	Three Digits Digital Switch, Sensitivity setting (x 0.1, x 0.01/ x 0.001)
Input Ranges	10, 100, 1000, 10000 m/s^2 at 0.03 to 0.999 $pC/m/s^2$ 1, 10, 100, 1000 m/s^2 at 1.0 to 9.99 $pC/m/s^2$ 0.1, 1, 10, 100 m/s^2 at 10 to 99.9 $pC/m/s^2$
Sensitivity Range	from 0.03 to 999 pC/m/ s^2 or mV/m/ s^2
Rated Output	±1V; BNC Connector; Output Impedance 1 ohm or less
Maximum Output	±10V; ±10mA; Load Impedance 2k-ohm or more
Sensitivity Accuracy	±1.0% or less
Frequency Response	0.2Hz to 50kHz; +0.5dB/-3dB; LPF and HPF Pass; 'H' or 'M' Range
Output Filter	Low Pass Filter (-3dB ±1dB); 100, 300, 1k, 3k, 10kHz; -12dB/oct High Pass Filter (-3dB); 5Hz; -12dB/oct
Noise Level	0.02pC(mV) rms or less; at Input Input Capacitance 1000pF, Sensitivity 1pC(mV)/m/ s^2; Output 1m/s^2 ; LPF Pass
Calibration Voltage	Sin Wave 200Hz±20Hz, 2Vpp±5%
Power Supply	DC 10V to 15V 200mA AC 90V to 135V 8VA

Characteristics of data acquisition device.

Model	Roga Instruments Plug.n.DAQ
Analog Input	2 channels single ended BNC, IEPE
Impedance	100 kOhm
IEPE power	24 V/4 mA
Input ranges	0.1 V, 1 V, 10 V
Bandwidth	3.5 Hz to 24 kHz (-3 dB) 10 Hz to 22 kHz (-0.5 dB)
Sampling Frequency	32 kHz; 44.1 kHz; 48 kHz
Absolute accuracy	2% typical
Gain accuracy	0.2% or better
Distortion	<0.05%
S/N	>85 dB (90 dB typical)
Aliasing rejection	-70 dB (up to 0.4 xfs)
Pass band ripple	0.05 dB
Analog output	2 channels single ended BNC
Output	1 V, 100 Ohm
Bandwidth	1 Hz-22 kHz (+/- 0.5 dB, 48 kHz FS) 0.5 Hz-24 kHz (-3 dB, 48 kHz FS)
Absolute accuracy	2% typical
Distortion	<0.02%
S/N	>90 dB
Pass band ripple	0.2 dB

Sensor characteristics for water cavitation.

Model	TEAC-601	Peak operating	±100,000 m/s^2
Sensitivity	0.3±20% pC/(m/s^2)	Shock survivability (peak)	200,000 m/s^2
Transverse sensitivity (max)	5%	Grounding	Case ground
Capacitance	1,000±20% pF	Connector	Micro connector (M3 screw)
Operating temperature range	−20 to 80°C	Case	Titanium
Frequency response (±3 dB)*	fc to 30kHz	Weight (approx.)	2.7 g
Resonant frequency (approx.)	60kHz	Size	9 HEX x 10.5 H

*fc depends on the time constant of the connected amplifier, fc=1/2 πRC.

Characteristics of high-speed camera.

Model	Photron Fastcam-Net 1000
Lens mount	C mount type
Sensor	CCD
Memory	128 MByte
Frame rate	30-10,000 fps (frame per second)
Frame size	512 x 480 to 128 x 34 pixels
Shutter speed	1/500 to 1/120,000 sec.
Power supply	AC 100V 50/60 Hz
Operating temperature	0-35°C

Characteristics of stroboscope.

Model	Sugawara MS-300
Flashing range	30-30,000 r/min (0.5-500 Hz)
Flashing energy	5 W
Flash duration	2.4 μs
Function	Internal sync, external sync, frequency dividing, delay, shift.
Power supply	90-264 VAC

Specification of the dissolved oxygen (DO) meter.

Model	Horiba OM-51	
Measurement Method	Dissolved Oxygen	Diaphragm galvanic battery method
	Saturation Oxygen	Dissolved Oxygen conversion
	Oxygen	Dissolved Oxygen conversion
Measurement Range	Temperature	0.0 ~ 100.0; Resolution 0.1:
	Dissolved Oxygen	0.00 ~ 19.99 mg/L; Resolution 0.01mg/L
	Saturation Oxygen	0.0 ~ 199.9%; Resolution 0.1%
	Oxygen	0.0 ~ 50.0%; Resolution 0.1%
Repeatability	Temperature	±0.1±1 digit
	Dissolved Oxygen	±0.1mg/L±1 digit

LIST OF PUBLICATIONS

I. International journal papers

1) Teddy Ardiansyah and Minoru Takahashi, Comparison of Sodium and Water Cavitation in Venturi Channel, submitted to the Journal of Power and Energy Systems, Special Issue of ICONE19 (under review).
2) Teddy Ardiansyah, Minoru Takahashi, Yoshio Yoshizawa, Masamichi Nakagawa, Kuniaki Miura and Makoto Asaba, The Onset of Cavitation and The Acoustic Noise Characteristics of Sodium Flow in a Venturi, Journal of Power and Energy Systems, Vol. 5, No. 1, January 31, 2011, pp. 33-44.
3) Teddy Ardiansyah, Minoru Takahashi, Makoto Asaba and Kuniaki Miura, Cavitation Erosion in Flowing Liquid Sodium Using Venturi Test Section, Journal of Power and Energy Systems, Vol. 5, No. 1, January 31, 2011, pp. 77-85.

II. International conference papers

1) Teddy Ardiansyah, Minoru Takahashi and Xi Chen, Comparison of The Water and Sodium Cavitation Phenomena in Venturi, Proceedings of the 19th International Conference on Nuclear Engineering (ICONE-19), ICONE19-43535, October 24-25, 2011, Osaka, Japan.
2) Teddy Ardiansyah and Minoru Takahashi, Investigation of Cavitation Phenomena for Innovative Sodium- and Lead-Bismuth-Cooled-Fast Reactors, Proceedings of the Third International Symposium on Innovative Nuclear Energy Systems (INES-3), October 31-November 3, 2010, Tokyo, Japan.

3) Minoru Takahashi, Tooru Kobayashi, Masashi Nakatsuka, Teddy Ardiansyah, Martin Kulhanek, Ales Vojacek, Vaclav Dostal, Shoji Uchida and Mingguang Zhang, Study on Liquid Lithium Target System for Boron Neutron Capture Therapy (BNCT), Proceedings of the 18th International Conference on Nuclear Engineering (ICONE-18), ICONE18-29516, May 17-21, 2010, Xi'an, China.
4) Teddy Ardiansyah, Minoru Takahashi, Yoshio Yoshizawa, Masamichi Nakagawa, Makoto Asaba and Kuniaki Miura, Numerical Simulation of Cavitation for Comparison of Sodium and Water Flows, Proceedings of the 18th International Conference on Nuclear Engineering (ICONE-18), ICONE18-29659, May 17-21, 2010, Xi'an, China.
5) Teddy Ardiansyah, Makoto Asaba, Kuniaki Miura and Minoru Takahashi, Characteristics of Cavitation and Erosion Phenomena in Sodium Flow, Proceedings of the 18th International Conference on Nuclear Engineering (ICONE-18), ICONE18-29545, May 17-21, 2010, Xi'an, China.
6) Teddy Ardiansyah, Minoru Takahashi, Masamichi Nakagawa, Kuniaki Miura and Makoto Asaba, Effect of Argon Gas Injection of Acoustics Noise and Onset of Sodium Cavitation in Venturi, Proceedings of the 13th International Topical Meeting on Nuclear Reactor Thermal Hydraulics (NURETH-13), N13P1217, September 27-October 2, 2009, Kanazawa, Japan.

7) Teddy Ardiansyah, Minoru Takahashi, Yoshio Yoshizawa, Masamichi Nakagawa, Kuniaki Miura and Makoto Asaba, Accoustic Noise and Onset of Sodium Cavitation in Venturi, Proceedings of the 6th Japan-Korea Symposium on Nuclear Thermal Hydraulics and Safety (NTHAS6), N6P1134, November 24-27, 2008, Okinawa, Japan.

III. Meetings and workshops

1) Teddy Ardiansyah and Minoru Takahashi, Numerical Calculation of Cavitation Bubble for the Simulation of Noise Spectrum, 2012 Annual Meeting of Atomic Energy Society of Japan (AESJ), March 19-21, 2012, Fukui, Japan.
2) Teddy Ardiansyah, Makoto Asaba, Kuniaki Miura and Minoru Takahashi, Experimental Study on Cavitation Erosion and Onset Condition in Sodium Flow, Proceedings of 2nd Multidisciplinary International Student Workshop 2010 (MISW 2010), August 5-6, 2010, Tokyo, Japan.
3) Teddy Ardiansyah, Minoru Takahashi, Makoto Asaba and Kuniaki Miura, Study on Sodium Cavitation for Fast Reactors (III)-Analysis of Cavitation with FLUENT and Erosion Experiment, 2010 Annual Meeting of Atomic Energy Society of Japan (AESJ), March 26-28, 2010, Mito, Japan.
4) Masashi Nakatsuka, Teddy Ardiansyah, Minoru Takahashi, Tooru Kobayashi, Development of Liquid Lithium Target for Neutron Capture Therapy Using Accelerator (1)-Water Film Flow Simulation Test, 2009 Fall Meeting of Atomic Energy Society of Japan (AESJ), September 16-18, 2010, Sendai, Japan.

5) Teddy Ardiansyah, Minoru Takahashi, Masamichi Nakagawa, Yoshio Yoshizawa, Kuniaki Miura and Makoto Asaba, Study on Sodium Cavitation for Fast Reactors (II)-Experiment of Cavitation Inception Condition and Noise Characteristics, 2008 Fall Meeting of Atomic Energy Society of Japan (AESJ), September 4-6, 2008, Kochi, Japan.

6) Minoru Takahashi, Makoto Asaba, Kuniaki Miura, Yoshio Yoshizawa, Masamichi Nakagawa and Teddy Ardiansyah, Study on Sodium Cavitation for Fast Reactors (I)-Subjects in Design of Reactor and Experimental Technique of Cavitation, 2008 Fall Meeting of Atomic Energy Society of Japan (AESJ), September 4-6, 2008, Kochi, Japan.